Characterizing Isotropic Materials in Corrosive Environments: A Non-Destructive Testing Approach using an Advanced Line Focus Transducer

by

Saleh Awad A. AlGhamdi

Bachelor of Science Mechanical Engineering, King Abdul-Aziz University, 2006

Master of Mechanical & Material Science, Swanson Engineering School, 2015

Submitted to the Graduate Faculty of the

Swanson School of Engineering in partial fulfillment

of the requirements for the degree of

Doctor of Philosophy

University of Pittsburgh

2023

UNIVERSITY OF PITTSBURGH

SWANSON SCHOOL OF ENGINEERING

This dissertation was presented

by

Saleh Awad A. AlGhamdi

It was defended on

July 14, 2023

and approved by

Heng Ban, PhD, Professor, Department of Mechanical Engineering and Materials Science

Patrick Smolinski, PhD, Associate Professor, Department of Mechanical Engineering and Materials Science

Guangyong Li, PhD, Associate Professor, Department of Electrical and Computer Engineering

Dissertation Director: Qing-Ming Wang, PhD, Professor, Department of Mechanical Engineering and Materials Science

Characterizing Isotropic Materials In Corrosive Environments: A Non-Destructive Testing Approach Using An Advanced Line Focus Transducer

Saleh Awad A. AlGhamdi, PhD

University of Pittsburgh, 2023

Corrosion plays a considerable role in metal degradation. For example, approximately 40% of the defense system maintenance is directed toward corrosion-related maintenance with an annual cost of $23 billion [2]. This research used an efficient noninvasive approach to characterize new materials, such as 3D print and metallic materials, using an improved lens-less line focus ultrasound transducer (LFT) system to measure the targeted structure under a harsh corrosive environment.

The purpose of the study is to develop a variety of different lens-less line focus transducer designs and validate them, considering the optimum design to define elastic constants of material structure. For this aim, the designed line focus transducers considered various focal lengths and aperture angles to capture Rayleigh surface wave and longitudinal bulk wave that relates to stiffness constants. Next step in the study considering the lack of any studies using the system in a corrosive environment, which raises the limitation of using the current design in a real-time testing in acidic environment, and to resolve this limitation, a proposed novel modification, includes coating the PVDF element using a paryelen-C and using different corrosion resistance casing for testing in high acidity solution. Next, some experiments will be conducted after fabricating the coated and uncoated LFT to compare the results and validate the new modifications.

After that, the Line focus transducer will determine the elastic constants of isotropic materials. The elastic constants will be derived using the Time-Resolved method relating the

defocus distance Δz and the time difference Δt between the bulk longitudinal wave and Rayleigh surface wave. new materials like 3D print will be tested to validate the Transducers, Elastic stiffness constants such as Young's & shear modulus and Poisson Ratio will be defined.

This final segment explores the application of LFT on novel Bulk Metallic Glasses, aiming to categorize the material while also verifying the design's consistency and reliability in producing repeatable results. This section includes the latest modifications to the Transducer and real-time testing under corrosive conditions such as seawater and acidic solutions. This represents a first in literature, serving to validate the proposed modifications through material characterization.

Table Of Contents

List Of Tables

List Of Figures

Preface

I begin by extending my heartfelt gratitude to my esteemed advisor, Professor Qing Ming Wang, whose boundless patience, invaluable assistance, continuous support, and expert guidance have propelled me to attain this significant milestone in my academic journey.

I am also deeply indebted to my respected lab partner and fellow Ph.D. candidate, Zihao Zhong, whose unwavering aid, and steadfast encouragement have been a constant source of strength throughout this research endeavor. Furthermore, I sincerely thank Dr. Qiuyan,Dr. Hong Fei Zu, Dr. Pei-Yuan Hsiao, Dr. Mohammad Gudarzi, Yuxiang Wang and Chenglong Ji for their valuable mentorship and guidance and not forgetting about Ruixin Feng, who helped and inspired me to do better work.

In completing this program, I cannot overlook the immeasurable support bestowed upon me by my supportive parents, whose encouragement has sustained me every step of the way. I am equally grateful to my siblings, whose well-wishes have constantly motivated me.

A special tribute goes to my life partner, my wife, Dr. Tumader Khouja, whose unfailing patience and steadfast support have been my pillar of strength throughout the years. I also extend my heartfelt thanks to my children, Omar, Zaina, and Adam, for their understanding and encouragement throughout this challenging journey.

In conclusion, I express my sincere appreciation to the Almighty, Alhamdulillah, for guiding and blessing me throughout this rewarding journey.

1.0 Introduction

This chapter addresses a comprehensive exploration of Nondestructive Testing (NDT) and Non-destructive Evaluation (NDE) techniques, particularly emphasizing ultrasound testing. The chapter traces the historical development of mechanical scanning acoustic microscopy (AM) methods, from their inception by pioneers such as Lemons and Quate in 1973 to modern transducer design and methodology advancements. The chapter will investigate the evolution of various ultrasound transducers and methodologies, highlighting the significant contributions made by researchers like Parmo, Bertoni, Chubachi, Kushibiki, and Yamanaka. The focus will be on the lens-less line focus transducer developed by D. Xiang and Yamanaka, chosen for its versatility, efficiency, and affordability. It aims to provide a comprehensive understanding of these transducers' evolution, functionality, and potential in the characterization of isotropic materials. The chapter underlines the significance of these developments in material characterization and sets the stage for the subsequent chapters investigating the practical application of these techniques. After that, a research objective that emphasizes the significance of this dissertation outlines.

1.1 Background And Literature Review

1.1.1 Line Focus Transducer

One of the many definitions of Nondestructive Testing (NDT) is using testing methods for materials or samples to evaluate defects present in them and characterize the material properties

under test. When using the NDT techniques to characterize the physical or mechanical properties of materials, such as measuring young's modulus of elasticity using the ultrasound velocity in materials, Non-destructive Evaluation (NDE) techniques refer to it. That means NDE techniques include all the mechanical characterization and NDT techniques used for defect evaluation. One of the most common NDT and NDE techniques is Ultrasound testing.[3]

Ultrasonic nondestructive evaluation techniques proved that it is the crucial key factor in determining material properties, more precisely using a mechanical scanning acoustic microscope (AM) technique with its unique application in material characterization. The first developers of this technique were Lemons and Quate in 1973[4, 5].

After that, researchers developed investigations of different designs of ultrasound transducers and methodologies. These investigations led to the emergence of one of the most popular measurement methods based on defining the leaky surface wave speed. Which is extracted from the V(z) curve and time-resolved defocus method under surface-wave acoustic microscopy [6]. The basic principle is to use a lens for focusing the planar waves produced from the transducer onto the sample to acquire The V(z) curve, which represents the output voltage amplitude of a piezoelectric transducer, and that curve would vary significantly by exhibiting periodical maxima and minima with the change of the distance between the acoustic probe and sample surface[6-8]. 1979 Parmo and Bertoni established the relationship between interval z and Rayleigh wave velocity [9].

During 1976 and 1977, Chubachi published new designs, including ZnO piezoelectric film deposited on a concave substrate of a gold hemispherical shell to produce a concave transducer with a focal distance of 5.9mm and frequency of 100MHz in water. They were designing a composite resonator using PVF2 piezoelectric films with a 30μm in thickness and 10~65MHz in

frequency. By 1985, Chubachi and Kushibiki published a novel method in the Acoustic microscopy field in their paper by using a line focus beam sapphire lens with a cylindrical concave surface with a curvature of 1.0mm radius and an aperture half-angle of $\theta = 60°$ and placing a ZnO film transducer fabricated to radiate and detect longitudinal acoustic waves with an operating frequency of about 200MHz, in order to characterize the materials [10]. For another twenty years, Kushibiki and his group kept optimizing the transducer design and studying material characterization using it [11-13]. Furthermore, more improved designs and techniques were enhanced to improve the lenses, such as the V-groove lens, the butterfly transducer, the slit aperture lens, and other designs [14-18].

By 1983, Yamanaka introduced a new technique to measure the leaky surface wave velocity on a small solid surface [19]. He used the impulsive converging beam generated from an acoustic lens. Using a new method depends on the difference in the time arrival between those two (axial and leaky surface waves) waves, which helped decrease the dependency on the scanning system's mechanical precision since the time interval measurement does not require mechanical scanning. According to the two reflected waves from the sample, a separation will start showing up in the time domain more clearly while defocusing the transducer lens distance z toward the sample. Yamanaka focused mainly on the axial wave and the leaky surface wave- since Parmon and Bertoni revealed in their work the significant contribution done by the output signals that reach the piezoelectric transducer, and they are the axial wave and leaky surface wave; the later time-resolved defocusing method is the term used to describe it. [9].

Later, between 1990-1999, D. Xiang et al. developed a new line focus transducer with no focal lens (lens-less) that significantly cut the price compared to the traditional Line focus transducer design and improved the measurement of Rayleigh wave speed in the time domain. It

was 10MHz in center frequency and utilized the time-resolved defocusing method to define the velocity of axial and leaky surface waves. The transducer differs because the PVDF film is taped onto the cylindrical curve inner surface made of close-matched tungsten powder-loaded epoxy resin instead of the traditional build. [20-23].

In 1995, Y. C. Lee et al. proved the transducer's ability to characterize isotropic solids and anisotropic thin films [24]. By 2005 and 2006, they developed a double PVDF thin film transducer to identify and characterize isotropic and anisotropic materials [25, 26].

The chosen transducer in this study will be the lens-less line focus transducer since developed D.Xiang, and Yamanaka developed it to make it more versatile for use with both isotropic and anisotropic materials. The ability to lower acoustic energy dissipation with a low f-number (ratio of focal length to aperture) significantly generates leaky surface waves efficiently. The fabrication of this transducer can be achieved at a lower budget than the lens transducers. [19, 23].

1.2 Research Objectives

This study's primary goal is to propose a new variety of designs for the lens-less line focus transducer radius of curvature and validate these new designs. From this last part, the second goal is to validate the newly fabricated designs by testing the capability of LFT using more complicated materials, such as Additive manufacturing materials produced from metal 3D printers, and adding to that, exploring the ability of the newly fabricated designs to identify and classify metallic glasses such as Bulk metallic glasses materials, Literature has never documented the accomplishment of such fabrication for this type of transducers.

Finally, another goal is aiming at contribute a new novel method of fabricating and modifying the Line Focus Transducer since, with many studies on Lens-Less line focus transducers, there is a lack of study on using the system in a corrosive environment by coating the Piezoelectric PVDF film, in turn, will be enabling to characterize stiffness constants of isotropic materials samples on-site instead of limiting the use of the system in a lab environment only.

1.2.1 Design Improvement & Fabrication of Different Curvature Lens-Less Line Focus Transducers

This study's primary goal is to propose a new variety of designs for the lens-less line focus transducer from a large to small radius of curvature. We are, furthermore, fabricating them with validation of each transducer by comparing their results with industry-standard ones. Fabricating different radii of curvatures would enable us to generate both Rayleigh surface wave and longitudinal bulk wave from the same device without the need to use two different systems and methods by using only one method called a time-resolved defocusing method with the v(z) curves,

which in turn will allow us to characterize the sample material going under corrosion, by extracting the main parameters such as Rayleigh critical angle θR, the leaky Rayleigh surface wave velocity, the Bulk longitudinal wave velocity, and the bulk transverse wave velocity. From that previous information, we can determine the independent elastic constants for isotropic material, such as Poisson's Ratio ν, Young's modulus E, and the shear modulus G for the samples before and after the corrosion testing. Having those parameters and comparing them to standard results, we can validate the fabricated Line Focus Transducer in our lab and choose the optimum new design.

1.2.2 Validating The Design And Fabricated Line Focus Transducer Using 3D Printed Samples And Classifying New Bulk Metallic Glasses

The goal is to investigate the fabrication process of a large aperture angle, lens-less Line Focus Ultrasonic Transducer (LFT) and subsequently validate its performance using different Metal alloys and materials such as 3D printed stainless steel materials and Bulk metallic Glasses (BMG). The research seeks to affirm the accuracy and repeatability of the results while acknowledging and investigating any discrepancies attributed to factors related to the fabrication and sintering process controlled by the additive manufacturing process. Also, to conduct an extensive investigation into Bulk Metallic Glasses (BMG) characterization using the Lens-Less Line focus Transducers LFT2030 and LFT3560. The research further aims to characterize the BMG materials using the validated Line Focus Transducer system, collecting, and analyzing data to calculate the velocities of the Rayleigh surface waves and other vital parameters. To define the Elastic constants, thereby gaining valuable insights into the properties of the samples and helping classify BMG, which has never been done before in the BMG field, which will demonstrate the reliability of the Time Domain methodology.

This research aims to contribute to a broader understanding of the structure-properties relationship of Bulk Metallic Glasses (BMG) samples and other isotropic materials. This goal will be accomplished by utilizing the accurate and reliable Line Focus Transducers LFT2030 and LFT3560 for data collection. The research aims to underscore the potential of the LFT ultrasound system as a dependable method for characterizing and estimating the elastic constants of these materials. Furthermore, it seeks to explore the system's potential use in defining and classifying uncertain metal alloy materials, thereby demonstrating its broader applications in material science.

1.2.3 Proposing A Novel Method To Fabricate Lens Less Line Focus Transducers For The Corrosive Environment

The primary objective of this part of the research is to introduce and implement an innovative method for fabricating Large Lens Less Line Focus Transducers (LFTs), thereby contributing significantly to the field of material characterization. It involves substantially modifying these transducers' traditional design and size, aiming to achieve a more compact and efficient device, including reconstructing the transducer casing using Polylactic Acid (PLA), a biodegradable thermoplastic derived from renewable resources, to reduce the weight and increase the durability of the transducer. Furthermore, the research aims to improve the resistance of the Polyvinylidene Fluoride (PVDF) film to harsh environmental conditions by coating it with Parylene-C. The last goal involves using the new fabricated line focus transducer and utilizing it in a corrosive environment while it is working by submerging the whole system in an acidic environment and finding out its ability to generate the Rayleigh wave and work properly in such a harsh environment, which will demonstrate enhanced material characterization capabilities and increased accuracy in output results using Ultrasonic Transducers.

2.0 Fundamentals Of Acoustic Waves, Corrosion, And Bulk Metallic Glasses

Waves' motion in gas, liquid, and solid and their effects are considered Acoustics, which is part of sound science.[27] During the 19th century, acoustics were considered art. However, in this new age, it became more scientific by entering the precision engineering era at the beginning of the 20th century. Until the 19th century, Human Ears were considered the primary instrument to measure the acoustic field. Simultaneously, whistles, gongs, and gunshots were the only controlled sound sources generated by the engineers at that time, with frequencies of 50Hz to 15 kHz. Meanwhile, great names like Rayleigh, Stokes, Lamb, Thomson, Helmholtz, König, Kundt, and many others made tremendous contributions to the physics of sound and published papers at that time. Especially after Lord Rayleigh's two-volume treatise Theory of Sound 1877/1878.[28]

In the late 19th century, Cauchy, Poisson, and Stokes proved the propagation of two types of elastic deformation waves through isotropic solids using the general theory of elasticity. The faster one is called a Longitudinal or irrotational wave, in which the particle motion would move in the same direction as the wave propagation direction. The second type is much slower, called the transverse or rotational wave, in which the particle motion would move perpendicular to the wave propagation direction. [29]

Additionally, Lord Rayleigh found an existence wave-type called surface wave that propagates over the surfaces, which is now named Rayleigh wave. The particle motion has an elliptical path with the major axis of the ellipse perpendicular to the surface of the solid. Moreover, noticing that the elliptical path of the particle motion (width) decreases exponentially with the increase in solid depth.[29]

Few differences between the body waves (Longitudinal & shear wave) and the surface wave are noticeable as the body waves spread out in three dimensions while conserving the energy propagated by the wave field, it must diminish in their displacement amplitude as r-1, where r is the distance from the source. In comparison, the surface waves only spread out in two dimensions and must diminish as r-1/2. Furthermore, that explains why the crustal earthquake is stronger and more damaging at moderate to large distances.[29].

2.1 Wave Definition

In general, waves are considered an elastic deformation leading to a change in the pressure (or displacement), electrical intensity or potential, or temperature that propagates the energy from point to point in a medium. Noticing that the particles in the medium witness local oscillations without traveling while the wave passes. [30] the same concept is valid for the Sound wave, where the waves are compressional oscillatory disturbance that propagates in an elastic medium, with no net flow for medium particles.[27]

According to the medium's particle displacement, movement, and direction, different sound waveforms with unique characteristics will generate from that movement. These sound waves can propagate in a medium depending on the material properties and their boundaries. There are mainly two types of sound waves in solids: plane or bulk waves, including Longitudinal and transverse waves. They travel through the body's interior, and they are faster than the surface waves. The other type is the surface waves, including the Rayleigh, Lamb, Love, and other guided waves. Since this study focuses on studying the Rayleigh surface wave and finding its velocities

on different material surfaces, we will emphasize the next section about these wave's features and derive the equations mathematically to find their velocities.

2.1.1 Longitudinal Wave

As mentioned, the Longitudinal wave is considered one of the Bulk or propagating wave components. Many terminologies name the longitudinal wave., like the compression wave and the P-waves (primary waves). The main feature distinct this wave is that particle displacement in the solid material would move in a parallel direction of the wave propagation. Simply the particles would only oscillate back and forth from their equilibrium position. It means the net movement of a particle is zero and that oscillation mainly transports the energy associated with the wave. As shown in Figure 2-1, the movement of the particles shapes a compression and rarefaction area or increases and decreases pressure area; with the alternate changing between these two areas simultaneously, the propagation of the wave will be formed and travel in a specific direction. Worth noting that the distance between two compression areas or rarefaction areas is called the wavelength λ.[30].

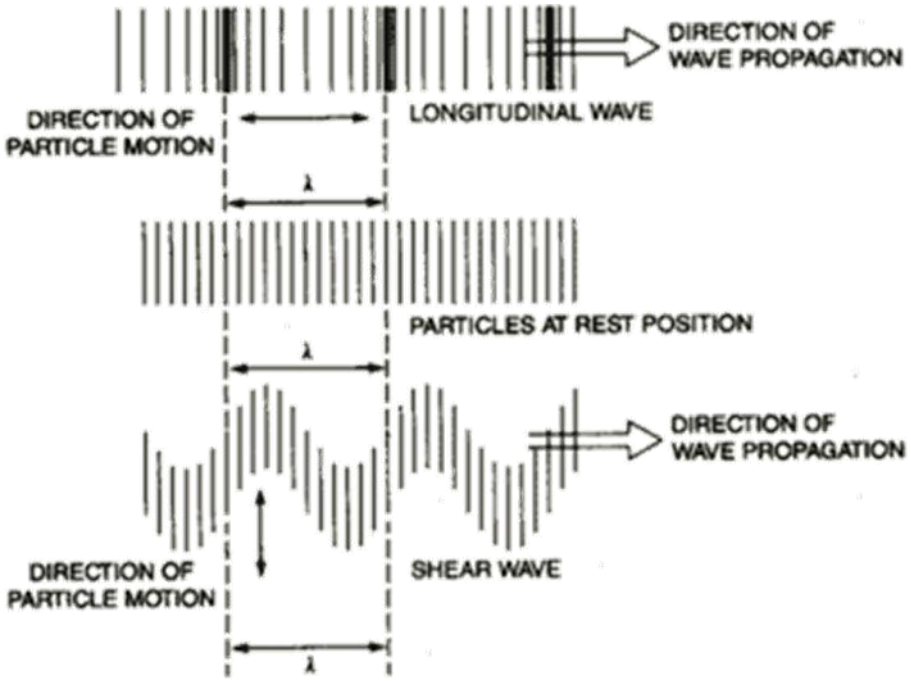

Figure 2-1 Longitudinal and Transverse wave representation [1]

2.1.2 Transverse Wave

The Transverse wave is another name for a shear wave or S wave (secondary wave). The shear wave has a different particle movement than the longitudinal wave. Although the particles oscillate and have no net movement, the particles move in a perpendicular direction to the wave propagation and are slower than the longitudinal wave. As shown in Figure 2-1, the particles move up and down from their equilibrium position while the wave moves horizontally. Since the particles move up and down about their equilibrium position, this type of wave creates a wave crest and trough, and the distance between two consecutive crests or troughs equals the wavelength λ.[30].

2.1.3 Surface Wave

2.1.3.1 Rayleigh Wave

Rayleigh wave is considered one of the surface waves (SAW) types. They are lower in frequency than body waves and slower as well. Moreover, it is assumed the solid is bounded (not infinite), which raises the importance of the wave propagation's boundary conditions—the Rayleigh surface wave named after the famous scientist John William Strutt, Lord Rayleigh. In 1885, Lord Rayleigh derived mathematically and proved the existence of this type of wave, and because it rolls, moving the ground up and down and side to side in the same direction, the wave is moving. [31]

Rayleigh wave occurred on the elastic medium's surface and combined the longitudinal and transverse waves' two motions. Since the particles in the elastic solid would have an elliptical path normal to the surface -the ellipse's major axis is vertical- and parallel to the direction of the propagation. On the surface, that particle will follow a counterclockwise path while moving away from the surface at greater depth, more than 1/5th of the wavelength, and the particles will trace a clockwise elliptical path. This type of motion names the designation of "retrograde.", where the particle has an opposite motion horizontally on the surface to the wave propagation direction while that motion becomes prograde at greater depth as shown in Figure 2-2. [30, 32]

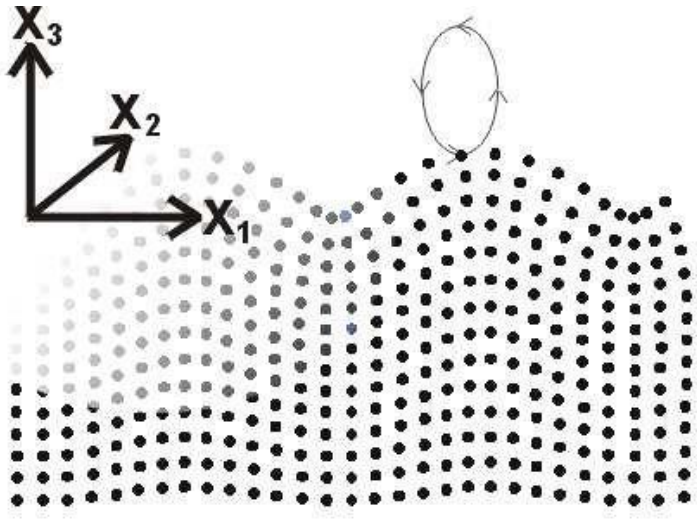

Figure 2-2 Coordinate system for Rayleigh waves on a surface [2]

2.2 Elastic Constants And Tensor Derivation Of Acoustic Waves In Solids

To describe the stress and strain using the tensor notation. Suffixed variables such as i, j, k, and l must be assigned to designate the Cartesian coordinates x, y, and z. One can describe the force acting per unit area on a surface using a traction vector with components τj, where j = x, y, z. considering an infinitesimal cube volume element with stress acting over its faces, tractions on the three faces can be described. Resulting in nine elements of stress σij, where the first suffix denotes the normal to the plane on which the given traction operates and the second suffix denotes a traction component's direction; furthermore, since a kinetic argument proves that σij = σji, there are only six independent components of the stress tensor [8].

Considering the deformation caused by the wave propagation within the elastic solid medium and the material's yield limit, the relationship between the stresses generated within the material and the deformations represented by the strains can be represented by Hook's law, which

will be linearized and matched between stress σij and strain εkl components using the elastic stiffness constants cijkl, which characterizes the elastic behavior in the small deformation solids. The cijkl called elastic stiffness constants serve as "microscopic spring constants" in describing what strain results from given stress [33].

First, the strain expressed in terms of the displacement derivative of a point in a solid considering rigid rotation will result in a strain. The strain components of the strain tensor are

$$\varepsilon_{kl} = \frac{1}{2}\left(\frac{\partial u_k}{\partial u_l} + \frac{\partial u_l}{\partial r_k}\right) \tag{2-1}$$

Where r_l and r_k are the position vector.

Second, the tensor notation Hook's law can be written as:

$$\sigma_{ij} = c_{ijkl}\varepsilon_{kl} \tag{2-2}$$

(The subscripts ijkl is known as the Einstein convention, which means summation over all k, l = x, y, z, i.e., nine terms). The elastic stiffness constant, c_{ijkl}, is a fourth-rank tensor, resulting in $3^4 = 81$ elements in the stiffness tensor coefficients. Secondly, considering the stress and strain tensors are symmetric, i.e., $\sigma_{ij} = \sigma_{ji}$ and $\varepsilon_{ij} = \varepsilon_{ij}$, that will result in a stiffness matrix requiring only 36 elements.[3] to enable it to be written as a matrix, a reduced notation for the independent elements of stress and strain is used,

$$\begin{pmatrix} \sigma_{xx} & \sigma_{xy} & \sigma_{xz} \\ \sigma_{yx} & \sigma_{yy} & \sigma_{yz} \\ \sigma_{zx} & \sigma_{zy} & \sigma_{zz} \end{pmatrix} = \begin{pmatrix} \sigma_1 & \sigma_6 & \sigma_5 \\ \sigma_6 & \sigma_2 & \sigma_4 \\ \sigma_5 & \sigma_4 & \sigma_3 \end{pmatrix} \tag{2-3}$$

Since only six independent components exist, the stress can be written in a one-column vector. The same applies to the strain abbreviated notation, with a simplification added by including the ½, simplifying Hook's law since it counts the two terms, such as $\varepsilon_{xy} + \varepsilon_{yx,}$ only once.

$$\begin{pmatrix} \varepsilon_{xx} & \varepsilon_{xy} & \varepsilon_{xz} \\ \varepsilon_{yx} & \varepsilon_{yy} & \varepsilon_{yz} \\ \varepsilon_{zx} & \varepsilon_{zy} & \varepsilon_{zz} \end{pmatrix} = \begin{pmatrix} \varepsilon_1 & \frac{1}{2}\varepsilon_6 & \frac{1}{2}\varepsilon_5 \\ \frac{1}{2}\varepsilon_6 & \varepsilon_2 & \frac{1}{2}\varepsilon_4 \\ \frac{1}{2}\varepsilon_5 & \frac{1}{2}\varepsilon_4 & \varepsilon_3 \end{pmatrix} \tag{2-4}$$

So, Hook's law (equation 2-2) can be written in abbreviated notation using the reduce notation, as:

$$\sigma_I = c_{IJ}\varepsilon_J \tag{2-5}$$

In the reduced notation, the double index ij will be replaced by a single index I and kl replaced by a single index J, where I and J range from 1 to 6. as shown in Table 2-1 Reduced Index Notation.

Table 2-1 Reduced Index Notation

Index ij , kl	Reduced index I,J	Matrix Representation
11	1	$\begin{pmatrix} \sigma_1 & \sigma_6 & \sigma_5 \\ \sigma_6 & \sigma_2 & \sigma_4 \\ \sigma_5 & \sigma_4 & \sigma_3 \end{pmatrix}$
22	2	
33	3	
23 or 32	4	
13 or 32	5	
12 or 21	6	

Moreover, since the stiffness matrix is symmetric $c_{IJ} = c_{JI}$ with respect to the reduced indices I and J, we can reduce the distinct or independent constants to 21 required to characterize the solid. The elastic properties reflect the material's symmetry, such as the crystal symmetry increasing the number of distinct elastic constants required to characterize the material decreases. Such as for cubic symmetry, there are only three independent constants, that is $c_{11} = c_{22} = c_{33,}$ $c_{44} = c_{55} = c_{66}$ and $c_{12} = (c_{IJ}$, $I \neq J$, I and $J \leq 3)$, where all other elements equal to zero. And that results in a stiffness matrix may be written using the abbreviated notation,

$$c_{IJ} = \begin{pmatrix} c_{11} & c_{12} & c_{12} & 0 & 0 & 0 \\ c_{12} & c_{11} & c_{12} & 0 & 0 & 0 \\ c_{12} & c_{12} & c_{11} & 0 & 0 & 0 \\ 0 & 0 & 0 & c_{44} & 0 & 0 \\ 0 & 0 & 0 & 0 & c_{44} & 0 \\ 0 & 0 & 0 & 0 & 0 & c_{44} \end{pmatrix} \tag{2-6}$$

There are only two independent constants for the isotropic material case, and they are c_{11} and c_{44}. One characterizes the elastic properties of the isotropic medium by Young's modulus and the other for Poisson's ratio, E and ν respectively, or by Lamé constants, λ and μ. And they are:

$$E \equiv \frac{c_{44}(3c_{11}-4c_{44})}{c_{11}-c_{44}} \equiv c_{11} - 2\frac{{c_{12}}^2}{c_{11}+c_{12}} \equiv \frac{\lambda}{2(\lambda+\mu)} \tag{2-7}$$

$$\nu \equiv \frac{c_{12}}{2(c_{11}-c_{44})} \equiv \frac{c_{12}}{c_{11}+c_{12}} \equiv \frac{\mu(3\lambda+2\mu)}{\lambda+\mu}$$

Moreover, the isotropic stiffness tensor can be obtained using $c_{12} = c_{11} - 2c_{44}$ in the cubic stiffness matrix.[4]

According to the stiffness matrix equation, 2-6 and Hook's law for isotropic medium equation 2-2 can be written as:

$$\sigma_{ij} = c_{11}\varepsilon_{ij} + \sum c_{12}\varepsilon_{kl}, \qquad \text{for } i = j \neq k = l; \tag{2-8}$$

$$= 2c_{44}\varepsilon_{ij,} \qquad \text{for } i \neq j,$$

The relation $c_{12} = c_{11} - 2c_{44}$, and equation 2-8, can rewrite it in the form.

$$\sigma_{ij} = (c_{11}-c_{12})\varepsilon_{ij} + c_{12}(\varepsilon_{11}+\varepsilon_{22}+\varepsilon_{33})\delta_{ij} \tag{2-9}$$

$$= 2c_{44}\varepsilon_{ij} + (c_{11}-2c_{44})\Theta\delta_{ij}$$

The dilation $\Theta \equiv \varepsilon_{11} + \varepsilon_{22} + \varepsilon_{33} \equiv \nabla \cdot u$, which is the divergence of the displacement. The vector operator del is $\nabla \equiv (\partial/\partial x, \partial/\partial y, \partial/\partial z)$; the displacement vector is $u \equiv (u_x, u_y, u_z)$; and δ_{ij} is the Kronecker delta function, where $\delta_{ij} = 1 \Leftrightarrow i = j$, $\delta_{ij} = 0 \Leftrightarrow i \neq j$, hence in (equation 2-9) when $i \neq j$ only the first term applies; and, when $i = j$, the $c_{44}\varepsilon_{ij}$ will cancel, leaving only $c_{11}\varepsilon_{ij}$ and the two other remaining uniaxial strain elements in Θ give the $c_{12}\varepsilon_{kl}$ terms in the first line of (equation 2-8).

Now, Newton's law can be written as

$$\rho \frac{\partial^2 u}{\partial t^2} = \frac{\partial \sigma_{ij}}{\partial r_j} + F_i \tag{2-10}$$

Where F_i are body forces (such as gravity), which will be neglected. Substituting Hook's law (equation 2-9) with Newton's law (equation 2-10) by swapping the order of terms of (equation 2-9), we get

$$\rho \frac{\partial^2 u}{\partial t^2} = (c_{11} - c_{44})\nabla(\nabla \cdot u) + c_{44}\nabla^2 u \tag{2-11}$$

And by using the standard vector identity

$$\nabla \times (\nabla \times u) \equiv \nabla (\nabla \cdot u) - \nabla^2 u \tag{2-12}$$

Equations 2-11 can be written as

$$\rho \frac{\partial^2 u}{\partial t^2} = c_{11}\nabla(\nabla \cdot u) - c_{44}\nabla \times (\nabla \times u) \tag{2-13}$$

Using Helmholtz's theorem, we can write the displacement vector u in terms of a scalar and a vector potential,

$$u = \nabla \emptyset + \nabla \times \psi \tag{2-14}$$

By applying Equation 2-14 to Equation 2-13, it gives

$$\rho \frac{\partial^2 \nabla \emptyset}{\partial t^2} + \rho \frac{\partial^2 \nabla \times \psi}{\partial t^2} = c_{11}\nabla(\nabla^2 \emptyset) - c_{44}\nabla \times (\nabla^2 \psi) \tag{2-15}$$

Note: the last term resulted from using the identity (equation 2-12), but this time using ψ as the vector knowing that term $\nabla \times [\nabla(\nabla \cdot \psi)]$ vanishes by standard vector identities $\nabla \times (\nabla \cdot \phi) \equiv 0$ and $\nabla \times (\nabla \cdot \psi) \equiv 0$. We can uncouple equations 2-15 into two separate equations, 2-16 & 2-17.

$$\nabla\left(\rho\frac{\partial^2\emptyset}{\partial t^2} - c_{11}\nabla^2\emptyset\right) = 0, \implies \rho\frac{\partial^2\emptyset}{\partial t^2} = c_{11}\nabla^2\emptyset; \tag{2-16}$$

and

$$\nabla \times \left(\rho\frac{\partial^2\psi}{\partial t^2} - c_{44}\nabla^2\psi\right) = 0, \implies \rho\frac{\partial^2\psi}{\partial t^2} = c_{44}\nabla^2\psi. \tag{2-17}$$

Equation 2-16 is scalar and has a wave solution with velocity $\mathbf{V_L} = \sqrt{(\mathbf{c_{11}/\rho})}$; this is the longitudinal wave equation called irrotational wave since $\nabla \times u = 0$ and no rotation in the medium. The second equation 2-17 is vector and has two degenerate orthogonal solutions with velocity $V_S = \sqrt{(c44/\rho)}$. These transverse or shear wave equations are called divergence-free waves since $\nabla \cdot u = 0$, and no dilation in this medium.

It is essential to notice that in isotropic solid material, c_{21} in (c_{11} - 2c44= c_{12}) should always be positive, and therefore c_{44} cannot be greater than $c_{11}/2$, which indicates $V_S < (1/\sqrt{2})\ V_L$ or $V_L > \sqrt{2}\ V_S$. that explains why the Longitudinal waves travel faster than the Shear waves

2.3 Wave Propagation In Liquid And Isotropic Solid Surface & Rayleigh Surface Wave

Rayleigh surface wave is considered a superposition of longitudinal and shear waves traveling over the solid surface with a common phase velocity, v_R, that velocity is slower than longitudinal and shear velocities [5]. Therefore, the wavenumber of Rayleigh surface wave $\beta \equiv \omega/V_R$ is greater than the longitudinal and shear wavenumbers $k_L \equiv \omega/V_L$ and $k_S \equiv \omega/V_S$.

Since the longitudinal and shear waves forming the surface wave decay exponentially away from the surface, their wavevector must have an imaginary component in the solid. They can be written α_l and α_s, and by using Pythagoras' theorem, we get,

$$\beta^2 + \alpha_l^2 = k_l^2 \tag{2-18}$$

$$\beta^2 + \alpha_s^2 = k_s^2 \tag{2-19}$$

As shown in 2-18 and 2-19, this case assumes the x-coordinate will be parallel to the surface while the z-coordinate will be normal to the surface with a negative value in the solid. It is noted that any component for $\partial/\partial y$ and u_y will vanish. Except for the vector potential ψ_y. The solution for longitudinal and shear components that decayed exponentially away from the surface and described by scalar and vector potentials, respectively, are:

$$\phi = \phi_0 e^{(i\beta x - i\alpha_l z)} \tag{2-20}$$

$$\psi_y = \psi_0 e^{(i\beta x - i\alpha_s z)} \tag{2-21}$$

By using Helmholtz's theorem equation 2-14, the displacement is

$$u = (u_x, u_z) = (i\beta, -i\alpha_l)\phi + (i\alpha_s, i\beta)\psi_y \tag{2-22}$$

$$= \left(i\beta\phi + i\alpha_s\psi_y,\ -i\alpha_l\phi + i\beta\psi_y\right)$$

And

$$\Theta = \nabla \cdot \mathrm{u} = -(\alpha_l^2 + \beta^2)\phi \tag{2-23}$$

Also, one of the crucial factors is the Boundary conditions with an assumption that the traction components (x &z) will vanish at the free surface. As mentioned earlier, the traction can be derived from Hook's law equation 2-9,

$$\sigma_{ij} = 2c_{44}\varepsilon_{ij} + (c_{11} - 2c_{44})\Theta\delta_{ij}$$

The strain components can be derived by applying Equation 2-22 to Equation 2-1 and the dilation from Equation 2-23. Then the normal component of the traction is

$$\sigma_{zz} = 2c_{44}\left(\frac{\partial u_z}{\partial z}\right) + (c_{11} - 2c_{44})\Theta \tag{2-24}$$

$$= 2c_{44}(-\alpha_l^2\phi + \beta\alpha_s\psi_y) + (c_{11} - 2c_{44})(-\alpha_l^2 - \beta^2)\phi = 0$$

Moreover, since the relationship between the stiffness constants (c_{11}, $c_{44,}$ and c_{12}), the wave velocities (V_L and V_S), and wavenumbers (k_l & k_S), we can derive $c_{11}/c_{44} = k_s^2/ k_l^2 = (\beta^2+\alpha_s^2)/(\beta^2+\alpha_l^2)$, according to this relationship we can rewrite equation 2-24 as:

$$\sigma_{zz} = c_{44}\{(-\alpha_s{}^2 + \beta^2)\phi + 2\beta\alpha_s\psi_y\} = 0 \tag{2-25}$$

Furthermore, that is true at z = 0.

The Tangential component of the traction is.

$$\sigma_{xz} = 2c_{44}\varepsilon_{xz} = \sigma_{ij} = c_{44}\left(\frac{\partial u_x}{\partial z} + \frac{\partial u_z}{\partial x}\right) \tag{2-26}$$

$$\sigma_{xz} = c_{44}\{2\beta\alpha_l\phi - (-\alpha_s{}^2 + \beta^2)\psi_y\} = 0$$

In addition, that is true at z = 0.

Considering that the x-dependence of ϕ & ψ_y is the same, and that is one of the boundary conditions, equivalent to Snell's law. At the same time, the z-dependence is unity at the surface by eliminating the explicit dependence on the stiffness elastic constants.

From equation 2-25,

$$\phi_0 = \frac{-2\beta\alpha_s\psi_0}{-\alpha_s{}^2 + \beta^2} \tag{2-27}$$

And from equation 2-26,

$$\psi_0 = \frac{2\beta\alpha_l\phi_0}{-{\alpha_s}^2 + \beta^2} \tag{2-28}$$

Hence,

$$4\beta^2\alpha_l\alpha_s + (\beta^2 - {\alpha_s}^2)^2 = 0 \tag{2-29}$$

Equation 2-29 is one form of the Rayleigh velocity equation. By squaring the two terms and multiplying them out, and using the relation ($\beta \equiv \omega/v_R$, $k_L \equiv \omega/V_L$, and $k_S \equiv \omega/V_S$) with equations 2-18 & 2-19, then equations 2-29 become an equation of the sixth order,

$$\left(\frac{V_R}{V_S}\right)^6 - 8\left(\frac{V_R}{V_S}\right)^4 + 8\left\{3 - 2\left(\frac{V_S}{V_L}\right)^2\right\}\left(\frac{V_R}{V_S}\right)^2 - 16\left\{1 - \left(\frac{V_S}{V_L}\right)^2\right\} = 0 \tag{2-30}$$

By assuming $X = (V_R/V_S)^2$, $Y = (V_S/V_L)^2$, equations 2-30 become more simplified,

$$X^3 - 8X^2 + 8(3 - 2Y)\,X - 16(1 - Y) = 0 \tag{2-31}$$

Since we ended up with a sextic equation, we should have six roots, but there is only one (real and positive) allowable solution in the case of Rayleigh velocity.[5] the ratio of the Rayleigh velocity to the shear velocity can be treated as a function of the Poisson ratio ν. As shown in Table 2-2, the Poisson ratio can be expressed as

$$\nu = \frac{1 - 2\left({V_S}/{V_L}\right)^2}{2\left\{1 - \left({V_S}/{V_L}\right)^2\right\}} \tag{2-32}$$

.

Table 2-2: Relationships between isotropic elastic constants

Lame Constants
$\lambda \equiv c_{12}$; $\mu \equiv c_{44}$.
For an isotropic material, c11 – c12 = 2c44, hence λ = c11 – 2c44; μ is also called the shear modulus, sometimes designated G.
Poisson ratio
$\boldsymbol{\sigma \equiv \frac{s_{12}}{s_{11}} \equiv \frac{c_{12}}{2(c_{11}-c_{44})} \equiv \frac{1-(2c_{44})/c_{11}}{2(1-c_{44}/c_{11})} \equiv \frac{\lambda}{2(\lambda+\mu)} \equiv \frac{E}{2\mu} - 1}$
Young Modulus
$\boldsymbol{E \equiv \frac{1}{s_{11}} \equiv \frac{c_{44}(3c_{11}-4c_{44})}{(c_{11}-c_{44})} \equiv \frac{\mu(3\lambda+2\mu)}{(\lambda+\mu)} \equiv 2\mu(1+\sigma)}$
Bulk modulus
$\boldsymbol{B \equiv c_{11} - \frac{4}{3}c_{44} \equiv \lambda + \frac{2}{3}\mu \equiv \frac{E\mu}{3(3\mu-E)} \equiv \frac{E}{3(1-2\sigma)}}$
Longitudinal wave modulus
$\boldsymbol{c_{11} \equiv \lambda + 2\mu \equiv \frac{\mu(4\mu-E)}{(3\mu-E)} \equiv \frac{(1-\sigma)E}{(1+\sigma)(1-2\sigma)} \equiv \frac{2(1-\sigma)}{1-2\sigma}\mu \equiv B + \frac{4}{3}\mu}$

So, equation 2-31 in terms of the Poisson ratio can be rewritten as:

$$\frac{X^3}{8(1-X)} + X = \frac{1}{(1-\nu)} \tag{2-33}$$

Besides, since most materials' acceptable range for ν ranges between 0 and 0.5, we will have V_s/V_L ranges between $1/\sqrt{2}$ to 0. According to that ratio, the Rayleigh velocity will vary between 87% to 95% of the shear velocity. This range will be an essential criterion for calculating the roots of shear wave velocity in later calculations. An approximate solution to equation 2-33 is [6]

$$V_R \approx V_S(1.14418 - 0.25771\,\upsilon + 0.12661\,\upsilon^2)^{-1} \tag{2-34}$$

2.4 Snell's Law - Reflection And Refraction At The Liquid-Solid Interface

At the interface of two different materials, the acoustic waves -i.e., ultrasonic beams- undergo reflection, refraction, scattering, and sometimes a combination. This phenomenon would occur from the mismatch of acoustic impedance between the materials. The water is medium one, and the metal we use in this study is medium two. It is also known that ultrasonic beams' reflection,

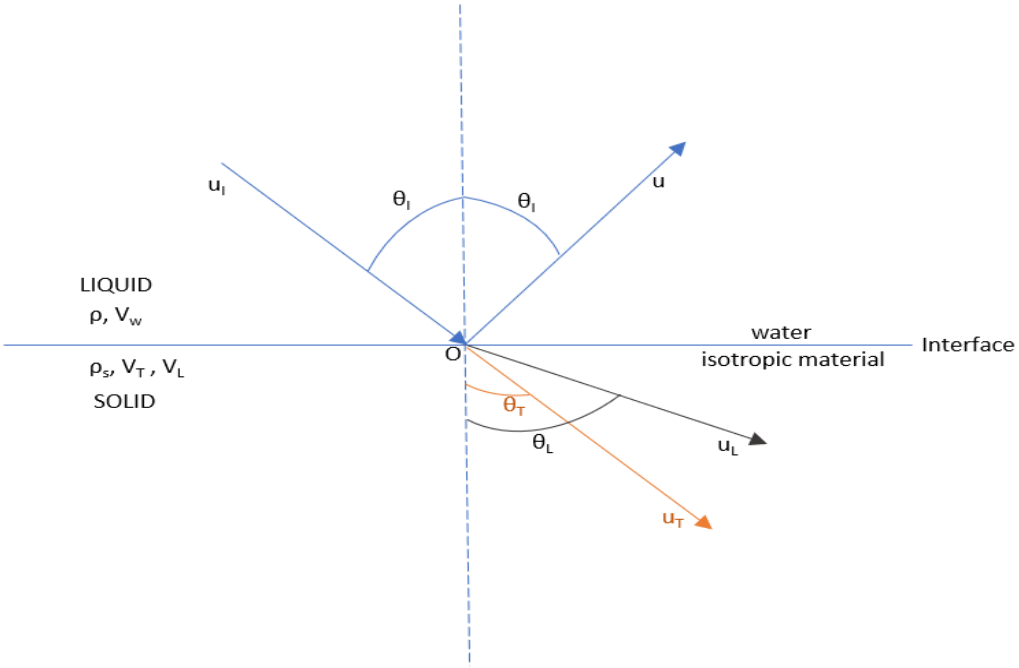

Figure 2-3:Interface between an isotropic solid and liquid

refraction, and scattering follow the same rules as optical beams. As per the optics rule, it can be seen from Figure 2-3, that the angle of the incident is equal to the angle of reflection (θ_I)[7].

The incident wave must be a longitudinal wave with a sample immersed in water and irradiated by an ultrasonic beam that generates refracted longitudinal and transverse waves in the isotropic metal since solid material supports the transverse movement of particles. Then the general law that describes wave behavior at the interface is Snell's law. "According to Snell's law, the ratio of the sine of the incidence to the sine of the angle of reflection or refraction equals the ratio of the corresponding wave velocity." [8, 9]

$$\frac{\sin\theta_I}{V_W} = \frac{\sin\theta_T}{V_T} = \frac{\sin\theta_L}{V_L}, \qquad \theta_I = \theta_L \tag{2-35}$$

Where Θ_I is the angle of incidence for incident longitudinal wave, and V_w is the sound propagation velocity in water. Simultaneously, θ_L and θ_T represent the angles of the propagated refracted Longitudinal and transverse waves, respectively. Both angles are measured from a line normal to the interface.

2.4.1 Critical Angles

When the incidence angle θ_I is small, the ultrasound wave undergoes a mode conversion at the boundary, resulting in the propagation of longitudinal and transverse waves simultaneously in the other medium. By increasing the incidence wave's angle, the direction of the refracted longitudinal wave will start to approach the boundary surface $\theta_L \longrightarrow 90°$. At some point, the incidence angle θ_I will reach a specific value where the θ_L will be precisely 90° (see Figure 2-4) such that $\sin\theta_I = V_w/V_L$ with $\theta_L = 90°$, above that value, no longitudinal refracted wave will

propagate in the material. That specific angle is known as the first critical angle, θ_1. By increasing the incidence angle's value beyond the first critical angle, the direction of the refracted shear wave will start to approach the boundary surface $\theta_T \longrightarrow 90°$. Of course, at some point of increasing, the refracted shear wave θ_T will be accurately 90° such that $\sin\theta_I = V_w/V_T$ with $\theta_T = 90°$.and again above that value, the shear wave will not propagate in the material. This second value of θ_I called the second critical angle θ_2. [9]

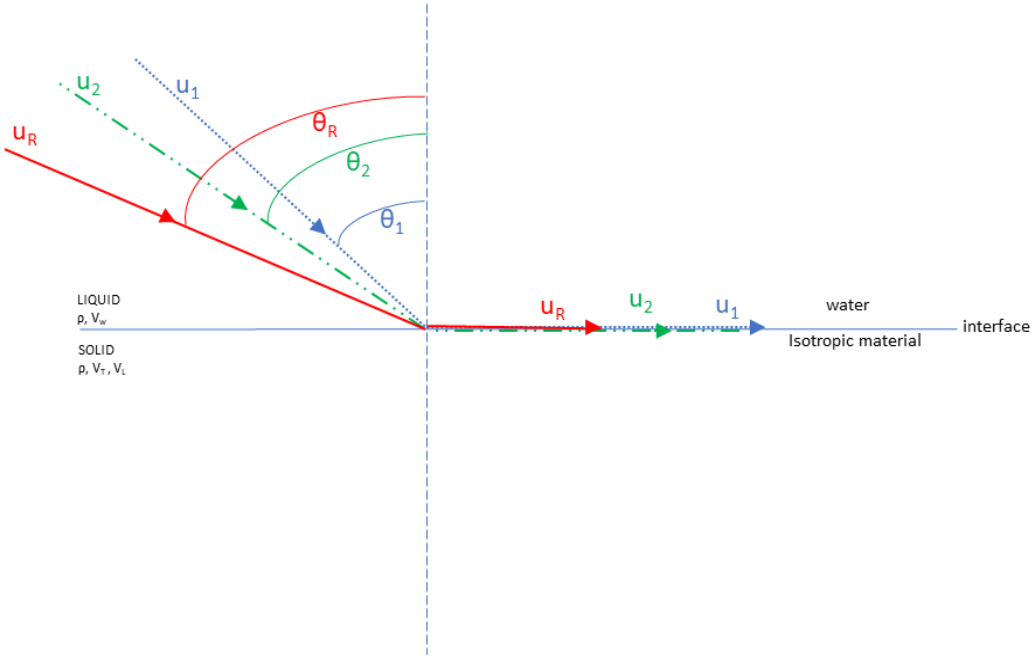

Figure 2-4:Critical angels including Rayleigh wave angle

Increasing the incidence angle slightly θ_I beyond the second critical angle to a specific angle called θ_R will result in exciting and generating the Rayleigh surface angle equal to $\sin\theta_R = V_w/V_R$, where V_R represents the Rayleigh surface wave velocity in the material.[9-11]

2.5 Piezoelectric Effect

The piezoelectric effect mainly means producing an electric charge that redistributes and spreads over the material surface due to applying stress on a unique crystalline material called dielectric material that belongs to a noncentrosymmetric class crystal classified as a piezoelectric material. This effect exists naturally in crystal materials, such as quartz (SiO_2), and poled (artificially polarized), such as PVDF.

When subjecting these piezoelectric materials to an external electric field, the anions and cations in the material will form asymmetric displacements that result in the deformation of the crystal. That strain form in the crystals becomes directly proportional to the applied electric field. This effect is called the indirect piezoelectric effect. In contrast, the direct effect happens when the material becomes subject to an external strain by applying stress that forces the dipoles in the crystal to rearrange and orient such that the crystal's opposite face develops positive and negative charges on each side.

The piezoelectric direct and indirect effects are represented in equations that relate the mechanical input to electrical output and vice versa, as shown in equations (2.36 - 2-39)

$$D = d\sigma \tag{2-36}$$

$$\begin{pmatrix} D_1 \\ D_2 \\ D_3 \end{pmatrix} = \begin{pmatrix} d_{11}\ d_{12}\ d_{13}\ d_{14}\ d_{15}\ d_{16} \\ d_{21}\ d_{22}\ d_{23}\ d_{24}\ d_{25}\ d_{26} \\ d_{31}\ d_{32}\ d_{33}\ d_{34}\ d_{35}\ d_{36} \end{pmatrix} \begin{pmatrix} \\ \sigma_1 \\ \sigma_2 \\ \sigma_3 \\ \sigma_4 \\ \sigma_5 \\ \sigma_6 \end{pmatrix} \tag{2-37}$$

$$\epsilon = dE \tag{2-38}$$

$$\begin{pmatrix} \epsilon_1 \\ \epsilon_2 \\ \epsilon_3 \\ \epsilon_4 \\ \epsilon_5 \\ \epsilon_6 \end{pmatrix} = \begin{pmatrix} d_{11}\, d_{12}\, d_{13}\, d_{14}\, d_{15}\, d_{16} \\ d_{21}\, d_{22}\, d_{23}\, d_{24}\, d_{25}\, d_{26} \\ d_{31}\, d_{32}\, d_{33}\, d_{34}\, d_{35}\, d_{36} \end{pmatrix} \begin{pmatrix} E_1 \\ E_2 \\ E_3 \end{pmatrix} \tag{2-39}$$

Where (D or P) represents the surface charge density developed from applying electric field E to the dielectric material. Unit of D is C/m^2 ($coulomb/meter^2$). It is the same as P, representing the electric polarization or surface charge density defined by the total dipole moment per unit volume. On the other hand, E represents the electric field, the unit is V/m^{-1}, σ represents the stress, with unit $N.m^{-2,}$ and ϵ represents the strain and its unitless.

d represents the piezoelectric coefficient that describes the piezoelectric effect, which relates the polarization D and the stress σ equation 2.36. it is represented by a 3x6 matrix, as shown in equation 2.37, and its unit is C/N (coulomb/newton). The components of the abovementioned tensor can be reduced depending on the piezoelectric system's symmetry. Furthermore, since most of the piezoelectric materials used in sensors and transducers are polycrystalline or nanocrystalline; thus, they are isotropic due to the poling of the system in the z-direction (direction 3). The system is said to be orthotropic. Due to that fact, the number of independent components of the piezoelectric coefficients gets reduced to only three independent components, and they are d_{31}, $d_{33,}$ and d_{15}. So, the piezoelectric coefficient matrix becomes:

$$[d] = \begin{bmatrix} 0 & 0 & 0 & 0 & d_{15} & 0 \\ 0 & 0 & 0 & d_{15} & 0 & 0 \\ d_{31} & d_{31} & d_{33} & 0 & 0 & 0 \end{bmatrix} \quad (2\text{-}40)$$

Where $d_{31} = d_{13}$ and $d_{15} = d_{51}$.

The piezoelectric coefficient involves more parameters such as g, e, and h; each of these coefficients relates electrical or mechanical input to mechanical or electrical output. The definitions of these parameters and their units are described in Table 2-3.

Table 2-3: Piezoelectric Coefficients - Definition and Units

Piezoelectric coefficient	Definition	Unit
d	Polarization/stress	C/N
g	Electric field/stress	V.m/N
e	Polarization/strain	C/m^2
h	Electric field/strain	V/m
Where identity V ≡ N.m/C		

2.6 PVDF Material

The Piezoelectric effect was first recognized by the Curie's brothers in 1880 when they observed a new effect in a quartz crystal called piezoelectricity; "piezo" means pressure [12]. That effect is called the direct piezoelectric effect, which means the mechanical input applied on the material, such as stress or strain, converts to electrical output, such as an Electric field or voltage signal. Little practical use of the material was done until 1917 when Professor P. Langevin from France did an x-cut to plates of quartz samples generating sound waves in water, and that work led to the sonar development [13]. Later in 1969, H. Kawai discovered that PVDF (polyvinylidene fluoride) had a strong piezoelectricity effect. A few years later, in 1975, the Japanese company Pioneer, Ltd. developed the first commercial piezoelectric loudspeakers and earphones made of PVDF.

The PVDF (polyvinylidene fluoride) is a semicrystalline polymer with a 50% crystallinity and has a glass transition temperature (T_g) of about -35 ˚C. Moreover, since it is a semicrystalline polymer, it consists of a lamellar structure mixed with amorphous regions, with a repeat unit of molecular structure [C2H2F2]n, as shown in equation 2-41.

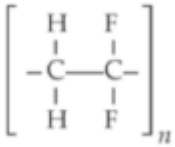

(2-41)

The main advantages of the polymer piezoelectric, including the PVDF, are flexibility, mechanically more stable, and shaping since it can be formed in a large area of thin films. The piezoelectric coefficients of poled thin films are reported to be as large as 6-7 $pC.N^{-1}$, which is ten times larger than any other polymer [14].

Although PVDF as a piezoelectric material has a lower piezoelectric coefficient than ceramic piezoelectric like PZT, they are more desirable in some applications due to the unique quality of opposing depolarizing while subjected to a high alternating electric field. That means that although the coefficient d_{31} in PVDF is only 10% of the PZT, the maximum strain in PVDF will be ten times greater than in PZT since the maximum permissible field is a hundred times greater for PVDF. Unlike other piezoelectric materials, the PVDF has a negative d_{33} value, which means that it will compress physically instead of expanding when exposed to an electric field, and that will be very useful in our transducer fabrication since it depends on the thickness mode observed in the PVDF films.

As a piezo film, the PVDF has a lower acoustic impedance than the piezoceramic materials, which are closer to water, human tissue, and other organic materials. E.g., the piezo film has an acoustic impedance 2.6 times that of the water, while the piezoceramic is about 11 times greater, which means a closer acoustic impedance would permit better and more efficient acoustic signals propagation in water.

Below is Table 2-4, some piezoelectric material compared to the PVDF material.

Table 2-4: Different Piezoelectric materials, including PVDF

Material property			PZT-4 Hard ceramic	PZT-5H soft ceramic	PVDF Polymer
Thickness mode coupling coefficient	k_t		0.47	0.52	0.19
Length extensional coupling coefficient	K_{33}		0.69	0.75	0.13
Piezoelectric strain constant	d_{33}	$pm.V^{-1}$	290	590	25
Piezoelectric voltage constant	g_{33}	$mV.m.N^{-1}$	26	20	230
Density	ρ	$(\times 10^3\ kg.m^{-3})$	7.70	7.50	1.78
Longitudinal speed	ν	ms^{-1}	4600	4600	2200
Acoustic impedance	$Z= \rho \nu$	MRayl	35	34	3.9

3.0 Fabricating And Validating Different Designs Of Lens-Less Line Focus Transducers For Isotropic Material Characterization

3.1 Background And Literature Review

One of the many definitions of Nondestructive Testing (NDT) is using testing methods for materials or samples to evaluate defects present in them and characterize the material properties under test. When using the NDT techniques to characterize the physical or mechanical properties of materials, such as measuring Young's modulus of elasticity using the ultrasound velocity in materials, it is referred to as Non-destructive Evaluation (NDE) techniques. That means NDE techniques include all the mechanical characterization and NDT techniques used for defect evaluation. One of the most common NDT and NDE techniques is Ultrasound testing.[7]

Ultrasonic nondestructive evaluation techniques proved crucial in determining material properties, more precisely, using the mechanical scanning acoustic microscope (AM) technique that uniquely applies to material characterization. The first developers of this technique were Lemons and Quate in 1973[15, 16].

After that, investigations of different designs of ultrasound transducers and methodologies emerged to result in one of the most popular measurement methods that are based on defining the leaky surface wave speed, which is extracted from the V(z) curve and time-resolved to defocus method under surface-wave acoustic microscopy [17]. The basic principle is to use a lens for focusing the planar waves produced from the transducer onto the sample to acquire The V(z) curve, which represents the output voltage amplitude of a piezoelectric transducer, and that curve would vary significantly by exhibiting periodical maxima and minima with the change of the distance

between the acoustic probe and sample surface[17-19]. 1979 Parmo and Bertoni established the relationship between interval z and Rayleigh wave velocity [20].

During 1976 and 1977, Chubachi published new designs, including ZnO piezoelectric film deposited on a concave substrate of a gold hemispherical shell to produce a concave transducer with a focal distance of 5.9mm and frequency of 100MHz in water. Plus, he was designing a composite resonator using PVF_2 piezoelectric films with a 30μm in thickness and 10~65MHz in frequency. By 1985, Chubachi and Kushibiki published a novel method in the Acoustic microscopy field in their paper by using a line focus beam with a sapphire lens and cylindrical concave surface with a curvature of 1.0mm radius and an aperture half-angle of $\theta = 60^{\circ}$ and placing a ZnO film transducer fabricated to radiate and detect longitudinal acoustic waves with an operating frequency of about 200MHz, in order to characterize the materials [21]. For another twenty years, Kushibiki and his group kept optimizing the transducer design and studying material characterization using it [22-24], and following that, more improved designs and techniques were developed to improve the lenses, such as the V-groove lens, the butterfly transducer, the slit aperture lens, and other designs [25-29].

By 1983, Yamanaka introduced a new technique to measure the leaky surface wave velocity on a small solid surface [30]. He utilized the impulsive converging beam that was generated from an acoustic lens. Using a new method depends on utilizing the difference in the time arrival between those two (axial and leaky surface waves) waves, which helped decrease the dependency on the scanning system's mechanical precision since the time interval measurement does not require mechanical scanning. According to the two reflected waves from the sample, a separation will start showing up in the time domain more clearly while defocusing the transducer lens distance z toward the sample. Yamanaka focused mainly on the axial wave and the leaky

surface wave- since Parmon and Bertoni revealed in their work the significant contribution done by the output signals that reach the piezoelectric transducer, and they are the axial wave and leaky surface wave, which are called later time-resolved defocusing method [20].

Later, and between 1990-1999, D.Xiang et al. developed a new line focus transducer with no focal lens (lens-less) with a 10MHz center frequency and utilizing the time-resolved defocusing method in defining the velocity of axial and leaky surface waves. The transducer is different since the PVDF film is taped onto the cylindrical curve inner surface made of closely matched tungsten powder-loaded epoxy resin instead of the traditional build [31-34].

In 1995, Y. C. Lee et al. proved the transducer's ability to characterize isotropic solids and anisotropic thin films [35]. By 2005 and 2006, they developed a double PVDF thin film transducer to identify and characterize isotropic and anisotropic materials [36, 37].

The chosen transducer in this study will be the lens-less line focus transducer developed by D. Xiang and Yamanaka. Since it is more versatile to be used with isotropic and anisotropic materials, it can lower acoustic energy dissipation with a low f-number (ratio of focal length to aperture) plays a significant role in generating leaky surface waves efficiently. It can be fabricated under a lower budget than the lens transducers [30, 34].

3.2 Lens-Less Line Focus Transducer Design, Fabrication, And System Configuration

3.2.1 Line Focus Transducer Design and Fabrication:

According to work done by D. Xiang [32] and Yamanaka [30], this type of Line focus transducer should have few requirements to reach a high measurement resolution in the time domain. Accordingly, the design should take into consideration the short-pulse broadband operation, so to achieve that goal, the following parameters should be met first:

3. Mechanical matching between the piezoelectrical element and the backing material,
4. Mechanical matching between the piezoelectrical element and the coupling liquid,
5. Electrical matching between the piezoelectrical element and the pulser/receiver network.

According to these design conditions, the commercial PVDF (Polyvinylidene fluoride) piezoelectric thin film has been chosen as an active element Since it is flexible to be conformed to the arc design and due to its low acoustic impedance, that matches both the backing material and the coupling liquid (deionized water).

A rectangular aluminum tube will be machined to the required curvature on one end and flat on the other (top), forming the transducer case as depicted in Figure 3-1. Another cylindrical tube will be used as the mandrel to form the required focal length by choosing the matching radius. After that, we bend the PVDF film onto the mandrel's cylindrical convex surface by taping it to the surface while placing the aluminum casing on top of the PVDF film and centering it. A blend of tungsten powder and epoxy resin will be cast inside the aluminum casing forming the backing material for the transducer. The assembled part will be left to cure for 24-48 hours, and then the mandrel and the tape covering the PVDF film will be removed carefully, and the wires from the PVDF film will be soldered to the connector.

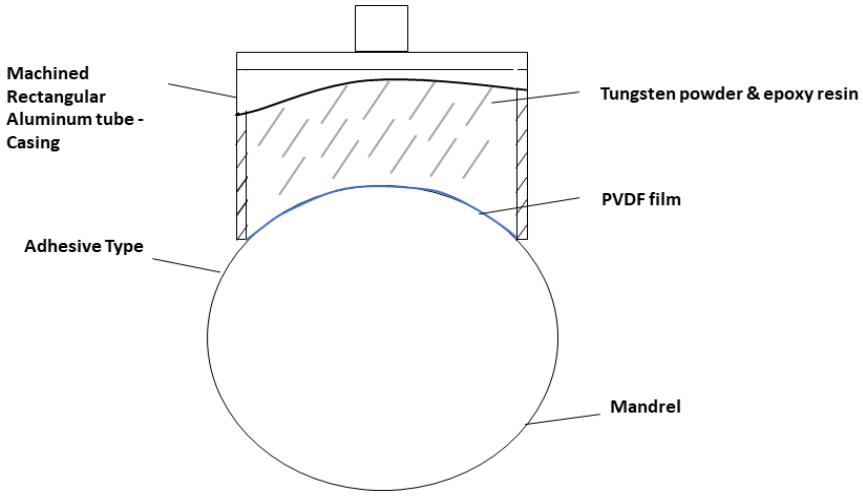

Figure 3-1:Schematic of Transducer Fabrication

In our research, the specifications used in building the transducers under investigation are four different Line Focus Transducers with different design dimensions to find the optimum curvature and aperture angle radius. LFT1530, LFT2030, LFT2530, and LFT3560 followed the naming criteria. Note that the LFT refers to the Line focus transducer, the first two digits refer to the radius of curvature in mm, and the second two digits refer to the arc length (in this case, the PVDF film length) in mm.

Table 3-1 Specification of constructed Line-focus PVDF Transducer LFT1530, LFT2030, LFT2530 & LFT3560

LFT Name	The radius of Curvature R ~ Focal Length F	PVDF film length = Arc Length	Aperture Angle θ
LFT1530	15	30	57.5
LFT2030	20	30	42.9
LFT2530	25	30	33.8
LFT3560	35	60	49.11

These Line Focus Transducers have the following design specification, as shown in Table 3-1 The focal length F ≈ (Radius of curvature) of 15mm, 20mm, 25mm, and 35mm, full aperture angle θ_{max} about 115, 85.9, 67.7 & 98.22 degrees & half-angle θ would be 57.5, 42.9, 33.8 and 49.11 respectively. The specification of the PVDF film is (30mm & 60mm) x 12.5mm with a thickness of 30 μm and a center frequency of 8-10 MHz (DT-028, NEG, Measurement specialties (MESA), TE Connectivity Ltd.) for all the transducers as shown in Figure 3-2.

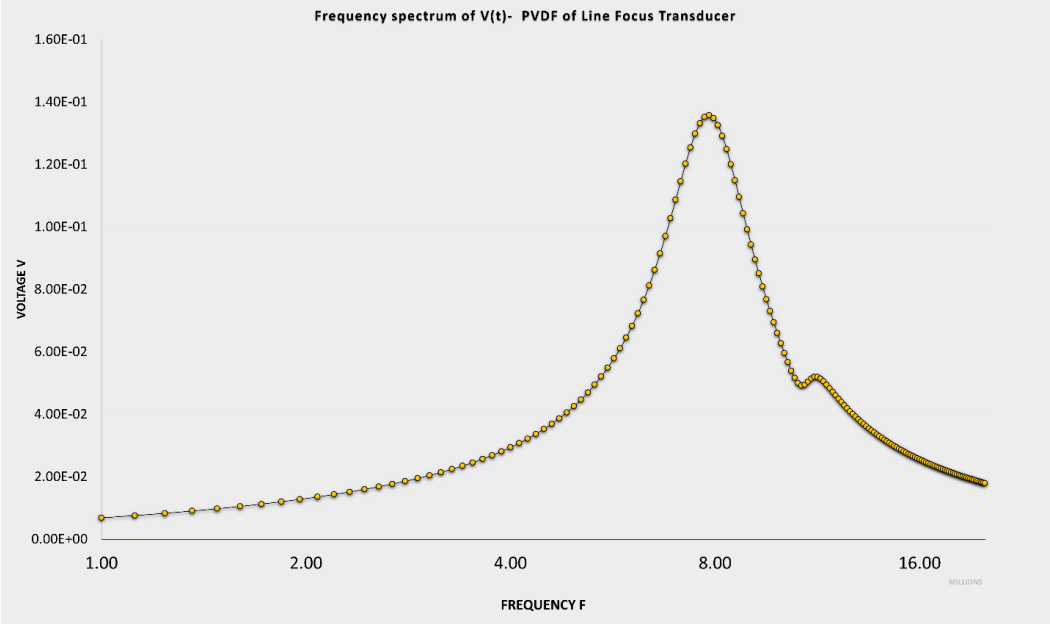

Figure 3-2: Frequency Spectrum of PVDF

The tungsten powder and the low viscosity epoxy (Devcon 2 Ton Epoxy ITW polymer Adhesive) blended with a weight ratio of 2:1. The goal of building different Transducers sizes is to validate and find the best covering maximum angle allowing the Leaky Rayleigh surface wave to propagate on the sample surface.

3.2.2 System Configuration or Equipment Setup:

As per the system assembly, configuration and as depicted in Figure 3-3, The Line Focus Ultrasonic,

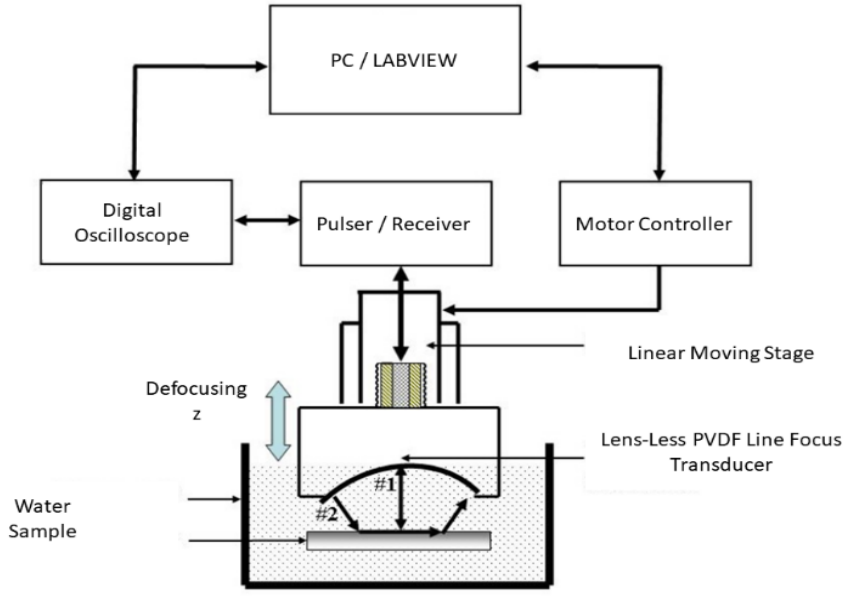

Figure 3-3:schematic diagram of the ultrasonic measurement

The testing system is built of a z-axis stage, as shown in Figure 3-4, which is used and controlled by a stepping motor controller DS102, made by SURUGA SEIKI CO., LTD, Figure 3-5 that is given a signal controlled by a LABVIEW Program to change the defocusing steps between the transducer and the sample surface vertically.

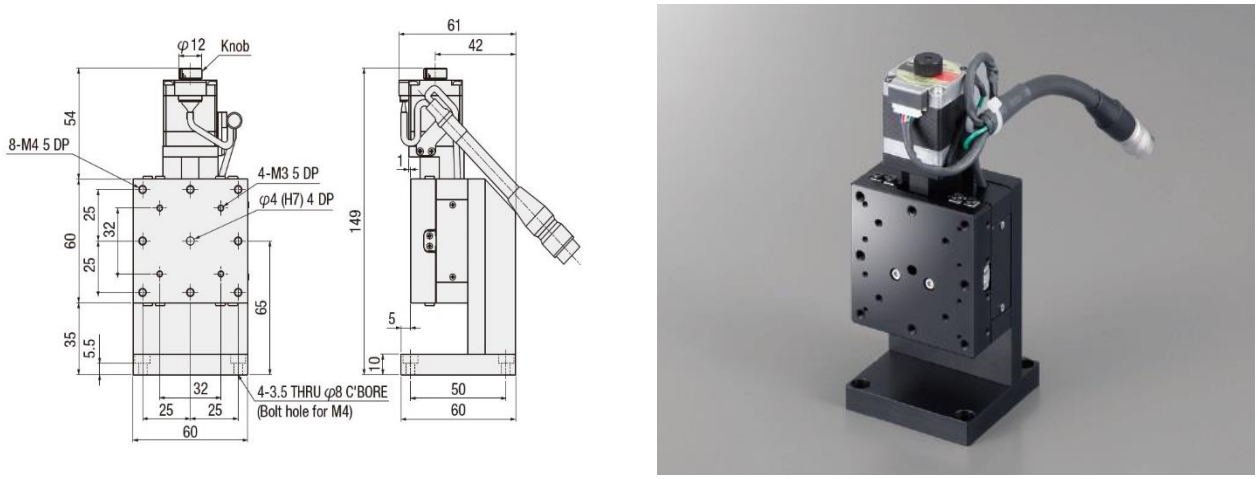

Figure 3-4: (a) Front and side view of Motorized stage, (b) Motorized stage in the z-axis

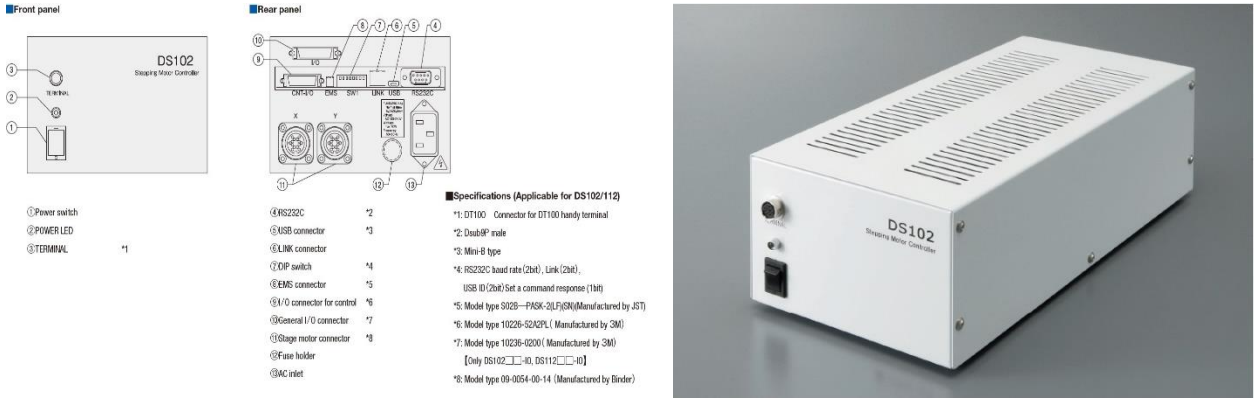

Figure 3-5: (a) Front and rear Panel of the Stepping motor Controller (b) DS102 Stepping Motor controller.

The travel range is between +/- 10mm, with a max—accuracy of 0.1μm. The Transducer will be used in a pulse-echo mode with the pulser/receiver, generating and receiving the signal. That signal will be generated by connecting the Piezoelectrical transducer to the Pulser/Receiver 5072PR system, made by OLYMPUS. The electric signal will be initiated from the pulser/receiver in the form of an electric pulse signal that excites the piezoelectric PVDF film attached to the transducer case to generate an acoustic wave that travels in the coupling medium (deionized water) and reflects from the sample as an echo which the same transducer will collect. The received wave

signal will be converted again to an electric signal (voltage form) and represented by a connected digital Oscilloscope 4034A, with a 350 MHz frequency span and a maximum Sampling rate of 4GSa/s. The total data collected is 2000 points in length, which would translate in the time domain as 2.5ns for each point, which means the sampling interval or the period for the waveform is 4.99 μsec, made by AGILENT TECHNOLOGIES. The received signal will be recorded and used later to analyze the waveform variation in the MATLAB program.

3.3 Measurement Methodology

In his research, Yamanaka introduced a more straightforward method to measure Rayleigh surface wave velocity without using the traditional V(z) curves technique that requires more strict mechanical precision.

The method depends on calculating the difference between the traveling time of each axial and leaky surface wave, called the time-resolved defocusing method [30].

The principle of measuring the leaky Rayleigh wave can be described using a ray representation shown in Figure 3-6 (a). when the sample surface is placed precisely on the transducer's focal plane, which means the waves from the transducer will be focused on the sample surface at point O, then there will be one echo pulse known as the direct reflected wave D received by the transducer on the path EOE. Another later echo pulse will be detected by the transducer, representing the wave that penetrates the sample and is reflected by the sample's back surface.

If the transducer moved toward the sample (defocusing) at distance z, the waveform would separate into two main pulses in the time domain. The first will be the direct reflected wave (path EOE), while the second wave with an incident angle value of the same critical angle θ_R will be the

Rayleigh surface wave emanating from the sample surface as it propagates. Not all the Rayleigh surface waves reach the transducer. Instead, some of it will be dissipated into the coupling medium (water) due to refraction at the lens reference, while the most efficient ray path was path ABO'CD [21].

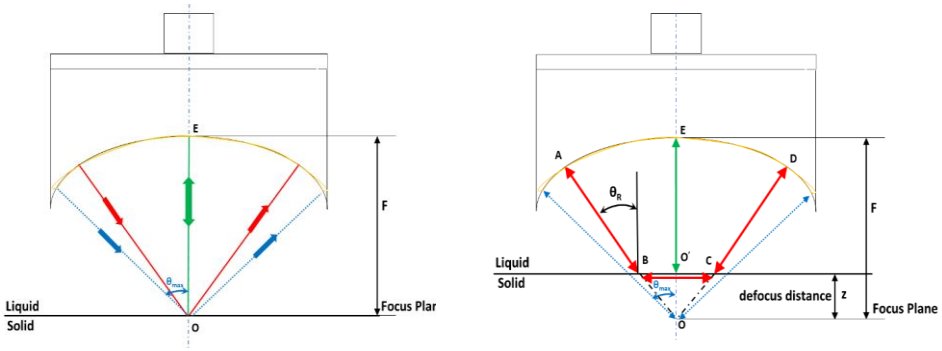

Figure 3-6:Ray Representation of the lens-less line focus transducer (a) sample surface at focus plane (b) sample defocused distance z from focus plane toward the transducer[1]

According to this information, the directly reflected wave (axial wave) can be used as a reference, then the arrival time of the leaky surface wave can be derived as the following:

The traveling time t of the axial wave, which is directly reflected from the surface of the sample taking path EO'E from Figure 3-6 (b), can be calculated as

$$T_A = \frac{2\,|EO'|}{V_w} = \frac{2\,(F-z)}{V_w} \qquad (3\text{-}1)$$

Where F is the distance of the focus plane of the transducer, z is the defocus distance, and V_w is the velocity of the acoustic wave propagating in the water (V_w = 1480 m/s at 23°C).

The traveling time of the leaky surface wave taking path ABO'CD from Figure 3-3 (b) can be calculated as

$$T_R = \frac{|AB| + |CD|}{V_w} + \frac{|BC|}{V_R} = \frac{2\,(F - \frac{z}{\cos\theta_R})}{V_w} + \frac{2(\tan\theta_R).z}{V_R} \quad (3\text{-}2)$$

V_R is the velocity of the leaky Rayleigh surface wave propagating on the sample surface.

By solving equations 3-1 and 3-2 simultaneously, we can result in the time delay of the Rayleigh surface wave t, and it can be described as

$$t = T_R - T_A = \frac{2z\,(1 - \cos\theta_R)}{V_w} \quad (3\text{-}3)$$

The term V_R has been eliminated from equation 3-3 by using the relationship of the Snell equation, which state that:

$$\frac{V_W}{V_R} = \frac{\sin\theta_R}{\sin\theta_w}\,, where\ \theta_w = 90° \quad (3\text{-}4)$$

The term z (defocusing distance) can be calculated by rearranging the equation 3-3 and represented as the following:

$$z = \frac{V_w}{2\,(1 - \cos\theta_R)}\,t \quad (3\text{-}11)$$

Knowing that θ_R is the Rayleigh critical angle given by

$$\sin^{-1}\left(\frac{V_W}{V_R}\right) = \theta_R \quad (3\text{-}5)$$

Moreover, according to relation 3-11, it is clear the linear relationship between the arrival time t of leaky Rayleigh surface wave and the defocusing distance z. So the slope of the distance

z as a function of the arrival time t will provide a relationship in terms of the Rayleigh critical angle θ_R, and it can be represented as:

$$\frac{dz}{dt} = \frac{V_w}{2\,(1-\cos\theta_R)} \tag{3-6}$$

The Rayleigh critical angle and slope relationship, respectively, can represent the leaky Rayleigh surface wave velocity from Snell's law as:

$$V_R = \frac{V_w}{\sin\theta_R} = \frac{V_w}{\sqrt{1-\cos^2\theta_R}} \tag{3-7}$$

The term cos θ_R has been eliminated from equation 3-7, and it is now the leaky Rayleigh wave velocity can be represented in terms of the slope and the wave velocity in the coupling medium (water) as the following:

$$V_R = \left[\frac{1}{V_w\left(\frac{dz}{dt}\right)} - \frac{1}{4\left(\frac{dz}{dt}\right)^2}\right]^{-1/2} \tag{3-8}$$

The values of z and t will be measured easily by moving the transducer with a known distance Δz while measuring the time differences Δt between the two pulses (the directly reflected wave and leaky Rayleigh surface wave).

The longitudinal wave velocity can be measured by using the pulse-echo technique. Knowing that the direct wave with path EOE and going through that sample to be reflected from the back wall, the transient time Δt (time difference between the front echo and back echo surface of the sample) we can represent it as:

$$V_L = \frac{2d}{\Delta t} \tag{3-9}$$

Where d is the sample thickness, doubling d is the wave propagating through the sample's upper surface and reflecting from the back surface.

3.4 Materials

The material samples will be studied to calibrate and validate the new design. They are commercial metal alloys mild steel, 420 stainless steel, 200 Nickle, Copper, and 6063 Aluminum alloy. The metal alloys are manufactured using conventional methods such as casting and machining; the bar's size is 20mm in width by 6mm in thickness and 60mm in length. After validating the results of the Longitudinal Shear wave velocity, the calculations for elastic properties of each sample will be listed, such as Young's modulus, Shear modulus, Poisson ratio, and Bulk modulus. Calculating all these elastic constants will help verify if the system can verify the standard manufactured material to be used in the future on fabricated metal alloys but does not have specific listed standards.

3.5 Experimental Results Discussion & Summary:

3.5.1 System Validation

3.5.1.1 Time-Resolved Defocusing Method Analysis:

The results shown in this chapter were generated by using the transducer LFT3560. The transducer specification was 25mm as a focal length and ~35 degrees as an aperture half-angle, while the sample used was standard 420SS stainless steel, Aluminum 6063, Nickle, Copper provided by Mcmaster Co.

The following methodology will be applied to all the standard samples, starting with sample 420SS stainless steel by placing it on a horizontal surface and submerged in distilled water under the transducer LFT3560; the lower stage that carries the water beaker and the sample was moved upward manually until reaching the highest waveform peak in the oscilloscope for the focal position was z = 0. In other words, the PVDF transducer's voltage response is V(t) in the time domain.

Once the focal position is found for the upper surface of the sample, an immediate representation of two waveforms appears as a response to the reflected wave echo from the sample's upper and lower surface, and they are the direct reflected wave D_U from path EOE and direct reflected wave D_B as it was depicted and explained previously in Figure 3-6. That same wave would be represented in a V(t) plot as in Figure 3-6, and the upper surface Du wave can be immediately distinguished and characterized by being the highest peak wave in the plot compared to the lower surface D_B Amplitude. The reasoning for that mainly refers to the higher percentage of reflection between the water as a fluid and the upper surface of the sample as a solid, expected to have 88% of the energy of the incident waveform will be reflected. At the same time, the rest

transmits to the sample, and some of the transmitted waveforms will be reflected again because of the back wall of the sample. Therefore, we can observe that D_U amplitude is always greater than D_B amplitude. Another essential factor that should be considered is the time delay or time difference between these two waves D_U and D_B as shown in Figure 3-7, which will be independent of the defocusing distance. The time difference will help us define the value of the Longitudinal wave velocity according to equation 3-9.

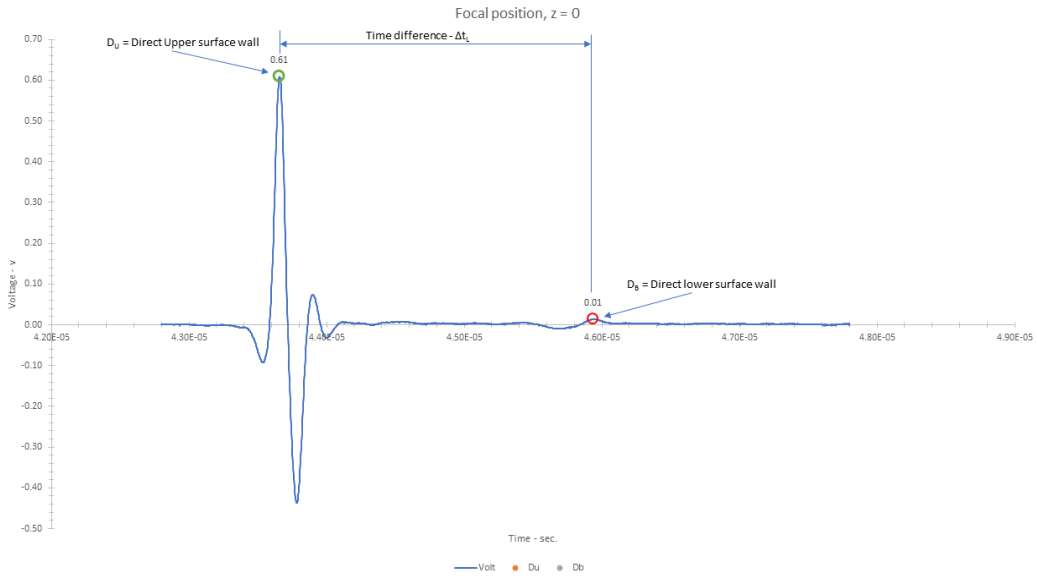

Figure 3-7:Waveform at focal distance for stainless steel SS316L, the defocus

Afterward, a defocus of the sample by moving the transducer toward the sample in about ten steps. Each step was fixed in value and equal to 0.25mm, adding up to 2.5mm. The first steps were taken to ensure the separation of the waveform's peak between the directly reflected wave and the Rayleigh surface wave. Afterward, each defocus amounting to the step value of 0.20 - 0.25mm; a waveform is recorded and named (step#). The defocus of 5mm is shown in Figure 3-7, which implies that the sample now is out of focus, which means the sample is much closer to the transducer now by 5mm, which results in receiving the Direct reflected wave from the upper

surface in a shorter time although the amplitude now is much smaller than it was in the focal position.

In Figure 3-8Figure 4-1, the Rayleigh surface wave became more recognizable than in the first defocusing steps. The wave can be generated if the aperture angle of the line focus transducer θ LFT is larger than θR. In LFT3560, the aperture angle is 49.11°. In this case, we know the velocity of the Longitudinal wave in stainless steel is 5790 m/s. While the Shear wave velocity is almost half the longitudinal, it is approximately 3100m/s. Moreover, knowing the velocity of sound in water is 1480m/s, we can find the second critical angle θ2 = 28.52°. According to the standard Rayleigh surface wave velocity in stainless steel (calculated from equation 3-10 [38]

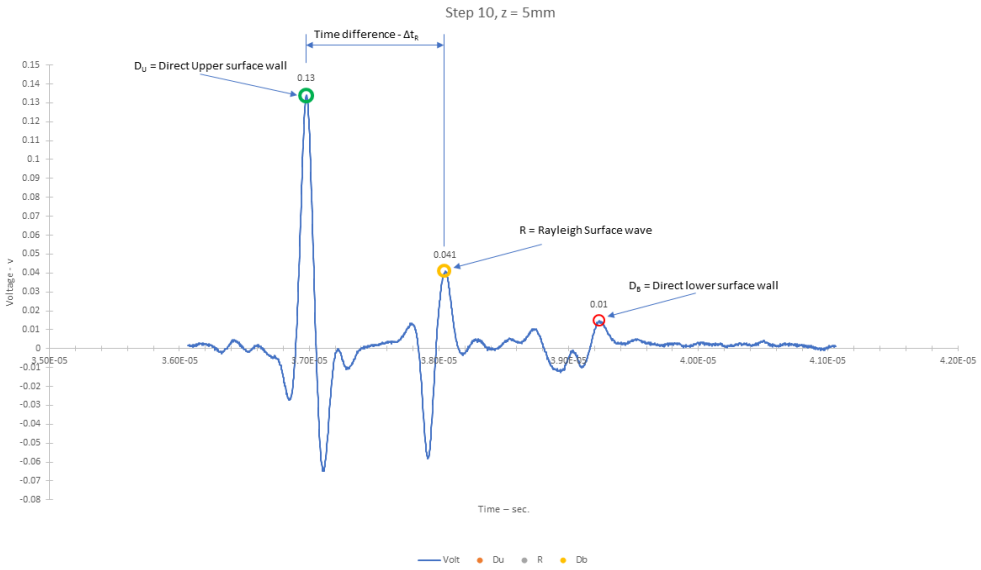

Figure 3-8:Waveform at focal distance for stainless steel SS316L, the defocus distance

with Poisson's ratio of 0.265) VR ≈2853 m/s, then Rayleigh angle $\theta_R \approx 31.25°$ and that proof that our Line Focus Transducer design LFT3560 is covering the Rayleigh angle.

$$V_R = V_S \frac{0.862 + 1.14\,\upsilon}{1 + \upsilon} \tag{3-10}$$

Where V_S is the shear wave velocity, and υ is the Poisson's ratio for stainless steel.

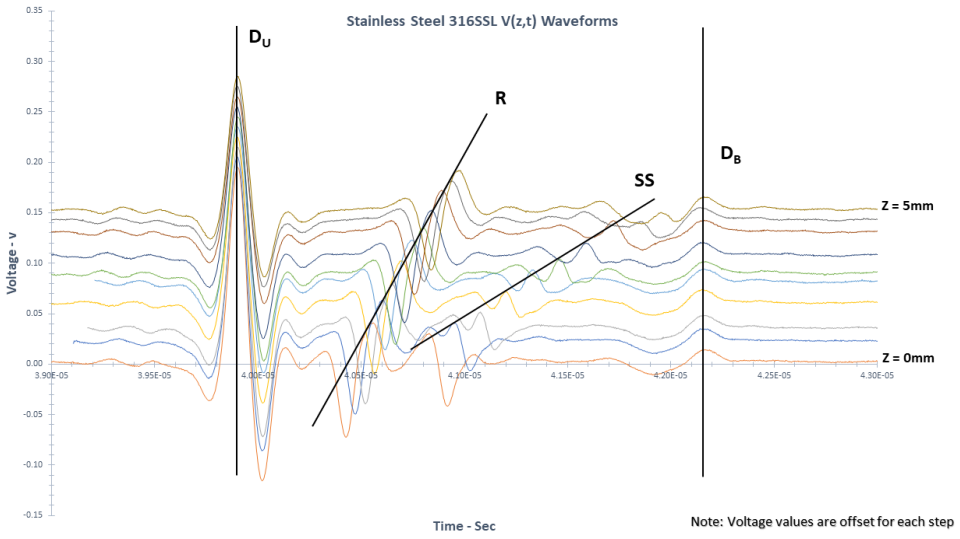

Figure 3-9:316SSL V(z,t) Waveforms overlapped

Another parameter can be extracted from Figure 3-8, which is the time interval between the direct wave peak U_D and Rayleigh wave peak R, and it is referred to in the graph as ΔtR that will facilitate the calculations for the Rayleigh wave velocity according to equation 3-8.

Plotting the v(z,t) graph for the stainless steel 420SSL with a changing defocus distance ranging from 0 to 5mm with an increment of 0.25mm will result in Figure 3-10. The values of ΔtR between the Direct wave DU and Rayleigh surface wave R in Figure 3-8 show a linear trend of increasing with the increase of the defocus value z, and the results confirm what is mentioned in

equations 3-8. Also, it is noticeable that the D_U is unchanging and confirmed by equations 3-9, which only considers the sample's thickness, which is constant, and the time difference between the D_U and D_B, which is constant. The wave SS, which is called the surface skimming wave, shows in our study, which means the line focus transducer can pick that kind of wave, and it shows to some extent a linear slope but with slower velocity and smaller value than the Rayleigh surface wave, but they are out of the scope of this research.

The peak of the Rayleigh surface wave in Figure 3-9 in different defocusing positions was linear, so according to that, a plot of defocusing distance z and time delays was proposed, as shown in Figure 3-10. A linear relationship between defocus z and time delay t agrees with the equation 3-6 relationship. From that graph, we can calculate the slope representing the dz/dt that amounted to 0.0053, which will be used in equations 3-8 to obtain the Rayleigh surface wave velocity.

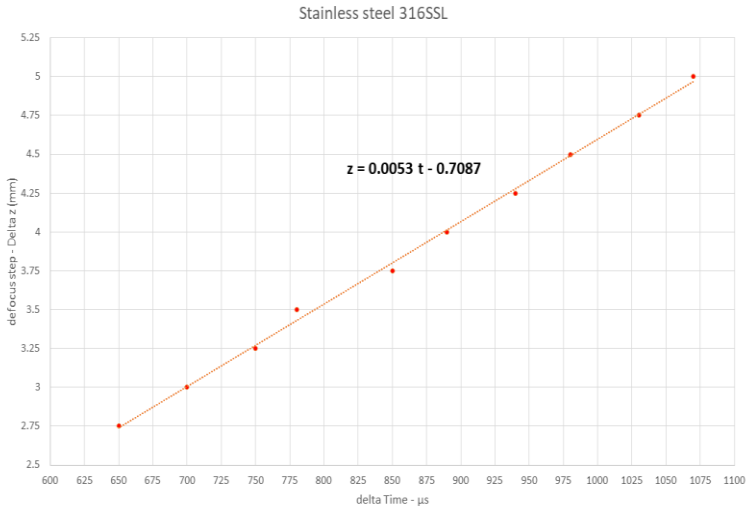

Figure 3-10:SS420 dz/dt plot

Applying the value of dz/dt in equation 3-8 will result in the Rayleigh wave velocity V_R in the stainless steel 420SSL, equal to 2905.2m/s. The longitudinal wave V_L values can be calculated using equations 3-9, which amounted to 5719.3m/s for a sample thickness of 6.5mm.

A calculation of the value of the shear wave velocity V_S can be possible according to equations 2-30 and 2-31, which can be represented much simpler as:

$$\left(\frac{V_S}{V_R}\right)^3 - \left(\frac{V_S}{V_R}\right)^2 - 0.718\left(\frac{V_L}{V_R}\right)^2\left(\frac{V_S}{V_R}\right) + \frac{3}{4}\left(\frac{V_L}{V_R}\right)^2 = 0 \tag{3-11}$$

Since this is a third-degree polynomial, we should end up with three roots of V_S. The only acceptable value will be $V_S / V_L < 1/\sqrt{2}$ for isotropic material solid. And according to that, the value of the shear wave velocity V_S = 3127.1m/s.

3.5.2 System Calibration and Material Characterization

After acquiring the shear wave velocity, it is possible now to describe the mechanical properties of isotropic solid materials using the elastic constants like Young's modulus (E), Shear modulus(G), Bulk Modulus (K), and Poison ratio (υ). Based on what was mentioned earlier in Chapter 2, the bulk wave propagation theory in solid. Using equations in Table 2-2, they are as follows:

$$E = \rho V_S^2 \frac{3V_L^2 - 4V_S^2}{V_L^2 - V_S^2} \tag{3-12}$$

$$G = \rho V_S^2 \tag{3-13}$$

$$\nu = \frac{2V_S^2 - V_L^2}{2(V_S^2 - V_L^2)} \tag{3-14}$$

$$\boldsymbol{K = \rho\ (V_L^2 - \frac{4}{3}V_S^2)} \tag{3-15}$$

Where E is Young's modulus of the material, G is the shear modulus, ν Poisson's ratio and K is Bulk Modulus.

The measured and calculated values are summarized in Table 3-2 and compared to the standard reference material.

Table 3-2: Measured Velocities and Elastic Properties' Calculation of Standard 316SSL Sample

Material		Density ρ (kg/m^3)	Measured Velocities (m/s)			Elastic Constants			
			Longitu-dinal Wave, V_L	Rayleigh Surface Wave, V_R	Shear-Transv-erse Wave, V_S	Young's Modulus, E (GPa)	Shear Modulus, G (GPa)	Poisson Ratio, ν	Bulk modulus, K(GPa)
Stainless Steel 420	measured	7820	5719.3	2905	3127	197	76.5	0.286	151
	Standard	7800	5720	-	3272	198	78	0.27	152
Copper	Measured	8820	4664	2102	2240	119	44.2	0.35	132
	Standard	8930	4648	-	2260	121	44.7	0.34	130
Nickle	Measured	7841	5777.8	2908	3127	198	76.7	0.29	160
	Standard	8830	5630	-	2815	205	77	0.31	162
Aluminum 6063	Measured	2689	6066	2950	3161	71	27	0.31	63
	Standard	2700	6320	-	3160	69	26	0.33	70

- Standard material collected from reference [39, 40]
- Rayleigh Wave velocity standards were calculated using equations 3-10 with the standard values.

As shown, Table 3-2 provides a comparison of the elastic properties of Stainless Steel 420, Copper, Nickel, and Aluminum. Each material showed varying degrees of deviation from the standard values for properties such as Young's Modulus, Shear Modulus, Poisson Ratio, and Bulk Modulus. The discrepancies ranged from slight underestimations to overestimations, depending on the specific property and material. On average, the variations fell within a range of approximately -3.41% to 5.93% (uncertainty levels) in the 12-13% range. That result will be used in the following chapters to validate the overall measured values compared to standard elastic constant values provided by manufacturers.

In summary, the measured elastic properties of these materials showed a range of deviations from the standard values. These variations highlight the importance of precision in measurements and the potential impact of different factors on the properties of materials. Despite these discrepancies, the measurements provide valuable insights into the elastic properties of these materials.

This study's findings affirm that the transducer's successful design and satisfactory results set the stage for further investigation. The subsequent phase of this research will involve the examination of fabricated Line Focus Transducers. These will be employed to authenticate the system with various materials, including 3D printed Stainless Steel 420, a product of additive manufacturing techniques, as elaborated in Chapter 4.

Furthermore, the fabricated transducers will be utilized to verify and identify new samples of Bulk Metallic Glasses, a topic that will be delved into in Chapter 5. A significant aspect of this research, to be discussed in Chapter 6, will involve using newly modified line focus transducers. These transducers, more compact and coated for durability, are designed to endure harsh environments such as seawater and acidic mediums, a milestone not previously accomplished. This

innovative approach aims to confirm the system's ability to accurately collect and interpret data from metal samples, such as those discussed in Chapters 3, 4, and 5. This novel methodology, largely unexplored according to existing literature, represents a significant contribution to the Ultrasonic nondestructive evaluation techniques field.

4.0 Fabrication Of A Large Aperture Angle, Lens Less Line Focus Ultrasonic Transducer & Validation With 3D Printed Stainless Steel Materials

This chapter investigates the intricate process of fabricating a large aperture angle, lens-less line focus ultrasonic transducer, and its subsequent validation using 3D printed stainless steel materials.

The chapter begins by tracing the historical development of 3D printing, highlighting its transformative impact on manufacturing processes. It underlines the ability of 3D printing to fabricate complex shapes using a diverse range of materials, thereby revolutionizing traditional manufacturing methods. It then transitions into a detailed examination of the SLM process, emphasizing its capacity to produce intricate geometric shapes using metal powders.

After that, the experimental procedure is accurately detailed, providing a step-by-step account of the alignment of the Line Focus Transducer (LFT) to the vertical orientation of the 3D printed samples, the adjustment of the focus position, the implementation of a systematic defocusing process, and the collection of data using two different LFT designs.

The chapter concludes with a comprehensive analysis of the samples' wave velocities and mechanical characteristics. The results section validates using the Line Focus Transducer system as a reliable methodology for characterizing isotropic material elastic properties. The chapter concludes by affirming the accuracy and repeatability of the results while acknowledging the presence of some discrepancies attributed to factors related to the fabrication and sintering process controlled by the additive manufacturing process.

This chapter thoroughly explores the fabrication of a large aperture angle, lens-less line Focus Ultrasonic Transducer, and its validation with 3D printed stainless steel materials. It offers

valuable insights into the potential of the Line Focus Transducer ultrasound system as a reliable method for characterizing and estimating the elastic constants of isotropic materials such as those produced by additive manufacturing. It also suggests its potential use in defining and classifying uncertain metal alloy materials.

4.1 Additive Manufacturing Method

4.1.1 3D-Printing Methods

The increasing need to fulfill extensive high precision, good quality, high production rates, and low production costs have led to a surge in demand for innovative manufacturing and assembly technologies. These technological advancements aim to enhance operational efficiency and attain a significant degree of self-governance in the manufacturing procedure, decreasing the product's time to market. Additive manufacturing (AM), commonly called 3D printing, has emerged as a promising technology that facilitates object production by adding material layers [41]. This stands in contrast to conventional manufacturing processes, which involve removing materials through milling, turning, drilling, and welding. The technology in question can fabricate intricate shapes that are difficult when produced through conventional means. It is achieved by employing diverse materials, including metals, thermoplastics, carbon fiber, and ceramics while minimizing material waste [42].

The evolution of 3D printing techniques has substantially expanded since it originated in 1976, coinciding with the advent of the inkjet printer. Charles Deckard Hull introduced stereolithography in 1984, a printing process that converts digital data into physical 3D objects. He was granted a patent for this technique in 1986. This innovative approach facilitated a transition from the conventional method of printing using ink to the utilization of diverse materials. During the 1990s, different corporations contributed to advancing 3D printing technology. Subsequently, in 2005, Z Corporation introduced the inaugural high-resolution color 3D printer. Subsequently, additive manufacturing has progressed as a state-of-the-art manufacturing methodology, recognized by various designations, including rapid prototyping, rapid manufacturing, laminated

object manufacturing, and additive manufacturing (AM) [43]. The term "additive manufacturing" implies the creation of three-dimensional solid objects from computer-generated or digital files.

The 3D printing procedure is considered one aspect of the comprehensive process, similar to the functionality of inkjet printers. Rather than ink, 3D printers inject the necessary material in multiple layers to create a physical object from a digital file. Start by making a three-dimensional object with commercial Computer-Aided Design (CAD) software like SolidWorks and saving it in a file that a 3D printer can read, like STL or ".thing." Subsequently, the 3D design model is exported to a slicing software, which analyses the model and converts the design files into instructions. The software produces a sequence of stratified slices and establishes the tool pattern (G-codes) for the 3D printing device. The printer receives the instructions through various means, such as a USB drive, USB cable, or local network. Following the completion of each layer, the build plate undergoes a downward displacement, thereby initiating the commencement of the subsequent layer's construction. Ultimately, upon completion of all layers, any surplus material, such as the raft and support structures, is eliminated to unveil the final product [44].

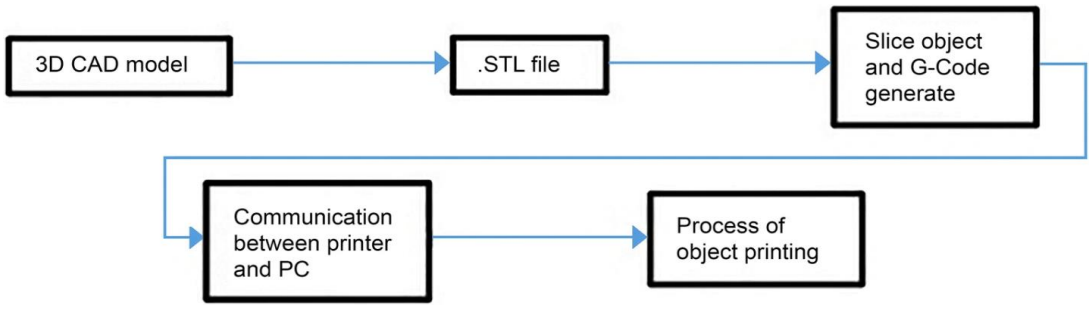

Figure 4-1 3D Printing Workflow [45]

Currently, plastic products are the primary materials utilized in 3D printing. In recent years, there has been a notable inclination towards using alternative materials such as metals, ceramics, and biomaterials.

Meanwhile, our study in this chapter will focus on 3D print metal alloy, in our case, stainless steel 316L; we are going to elaborate on metal material and Metal additive manufacturing (AM) utilizing the Powder bed fusion (PBF) methods and more specifically the Selective Laser Melting (SLM). Metal additive manufacturing (AM) is rapidly gaining popularity in engineering industries, with significant research efforts focused on developing new methods and usable materials [46].

4.1.2 Laser Powder-Bed Fusion Process

Selective laser melting (SLM) is a rapidly growing metal additive manufacturing (AM) technology in various engineering industries. It belongs to the powder bed fusion (PBF) method and allows producing complex geometric shapes using metal powders within the 30-50 μm range. The SLM process allows for achieving mechanical properties that are on par with those of bulk materials [47].

The SLM process begins with creating a 3D CAD model, which is then translated into machine instructions through slicer software. The software generates a code that controls the laser beam of the SLM printer. The laser selectively melts the metal powder layer by layer, and as each layer is completed, the build plate is lowered, and a subsequent layer of powder is deposited and melted to continue building the desired part geometry [46].

SLM offers several advantages in AM. It enables the production of parts with complex geometries, including thin walls and high-strength structural elements that would be challenging to manufacture using traditional methods due to geometric complexity. Technology can be employed at various stages of product development, from design concepts to low-volume

production. The dimensional quality of SLM-produced parts is generally high, often eliminating the need for extensive post-processing [48].

Nevertheless, SLM has a few limitations that should be considered. Porosity levels can be a concern in applications where gas tightness is crucial, such as high-pressure valves that require no leakage through the walls [49]. It is essential to point out that the mechanical characteristics of specimens fabricated through Selective Laser Melting (SLM) using 3D printing technology show anisotropy behavior, implying that they are subject to variation based on the build orientations and printing strategies employed, as indicated by [50] and [51] in their findings.

The SLM technology has garnered significant interest due to its potential for creating next-generation products and advancing AM. While extensive research has been conducted on the achievable mechanical properties of SLM-produced parts, there is still a lack of comprehensive material characterization tests utilizing the ultrasound methodology to define elastic mechanical properties such as Young's modulus, shear modulus, and Poisson ratio for the SLM produced parts and whether SLM-printed steel alloys can be a dependable method to fabricate products with high confidence of reproducibility and repeatability for the same part's shapes, dimensions and properties.

To address this gap in the literature, this study aims to measure wave velocities, characterize, and define the elastic constant of 316L stainless steel alloys produced using the SLM method by conducting a comprehensive analysis of Material Elastic properties for different samples produced using SLM methodology and comparing them by utilizing the ultrasound NDT methodology. This investigation aims to contribute to further developing and validating ultrasonic Line Focus Transducers technology and provide insights into its potential applications.

4.2 Materials

The samples utilized in the testing and validation process were primarily generated and printed using the EOS M290 (DMLS) printer, made available by the Additive Manufacturing Research Laboratory (AMRL) at the University of Pittsburgh, an institution established in 2016.

Three different samples in this test, as shown in Figure 3. These samples are 3D printed by the EOS M290 (DMLS) machine and made of stainless steel 316L powders with a material composition mentioned in Table 4-1.

Table 4-1: Material Composition of Stainless Steel 316L produced by EOS M290 (reference this to material datasheet eos stainless-steel 316L en web)

Element	Min	Max
Fe	Balance	
Cr	17.00	19.00
Ni	13.00	15.00
Mo	2.25	3.00
C		0.030
Mn		2.00
Cu		0.50
P		0.025
S		0.010
Si		0.75
N		0.10

The specific density of each sample was calculated using the mass, measured by a digital scale, and the volume from the dimensions measured by a caliper. For Sample 1, the approximate density is 8.00g/cm^3, while for Sample 2, it is 7.92g/cm^3; for Sample 3, it was 8.11g/cm^3, and

those results are very similar to standard data. Due to components built by additive manufacturing which consist of producing the samples layer by layer, the 3D printed metals can't guarantee the reproducibility of the samples, resulting in slight differences in elastic properties although the samples are isotropic. Accordingly, different specimen orientations are a factor that must be considered in the testing process. Young's modulus of printed Stainless-steel parts with standard parameters is approximately 171 GPa in the horizontal & vertical direction, according to the EOS datasheet, as shown in Table 4-2.

Table 4-2: EOS DataSheet for 3D Print 316 Stainless Steel

Parameters	EOS M 290 316L (HT)
ρ, Density g / cm^3	≥ 7.97
Tensile Strength, MPa	533.2 ± 1.1
Elongation at break, %	38.2 ± 0.1
Young's Modulus, E, GPa	≈ 171

Given this information, the specimen alignment with the Transducer PVDF film was crucially important to ensure the consistency of the result. Thus, the surface wave would propagate along the vertical direction (Z), as shown in Figure 4-2. Also, one surface specimen was chosen to prevent any inconsistency; in this case, we chose the surface with no marker.

Figure 4-2 3D Prints Samples 1,2 and 3 with Z- coordinate direction

4.3 Experimental Procedure

The procedure used in this test will follow the same steps described in Chapter 3. Which (began with a careful alignment of the Line Focus Transducer (LFT) to the vertical orientation of the 3D-printed samples. This step was crucial to ensure the accuracy of subsequent measurements, as precise alignment is pivotal for maintaining consistency in wave propagation characteristics.

Following alignment, the focus position was finely adjusted. The optimal focal position was determined by identifying the setting that yielded the highest amplitude of the directly reflected wave. This facilitated the most effective interaction between the ultrasound waves and the sample, yielding more precise measurements.

A systematic defocusing process was implemented once the optimal focus position was identified. This process involved incrementally moving the LFT closer to the specimen. The increments were carefully maintained at a constant step size of 0.2mm. This controlled approach was critical in ensuring uniformity in data collection and minimizing experimental error.

Each sample was tested three times to allow for a comprehensive data set and to account for potential variations between individual tests. The data collection process involved two different

LFT designs, LFT3560 and LFT2030, to allow for cross-verification of findings and ensure the reliability of the data.

After data collection, the results were averaged to accurately represent the Elastic constants - Young's Modulus, Shear Modulus, Bulk Modulus, and Poisson's Ratio.

4.4 Results And Discussion:

4.4.1 Wave Analysis Results & Discussion:

The standard material, such as the metal alloys we studied in the last chapter 3, is considered an isotropic material due to the fabrication casting conventional methods. Accordingly, the orientation of the samples will not influence the material property studied by the Line focus transducer. However, in additive manufacturing, we can witness some anisotropy since the laser sintering technology in the 3D printing machines have some directional movement in XY plane and Z plane, where XY represents the laser printing head movement as the sample lays on the try (face of the sample) while the Z movement is upward and downward the try (thickness of the sample) due to that factors a directional pattern exist favoring one direction (x- direction) over another (y-direction) but due to previous studies done on the effect of directional patterns on the Rayleigh surface wave velocity measured by Line focus transducers it has found out the differences of velocity will not exceed 1% and an error factor less than 3% [11], which can confirm that assuming the isotropy character of the additive manufacturing sample is acceptable which qualify the use of the wave propagation theory of isotropic materials.

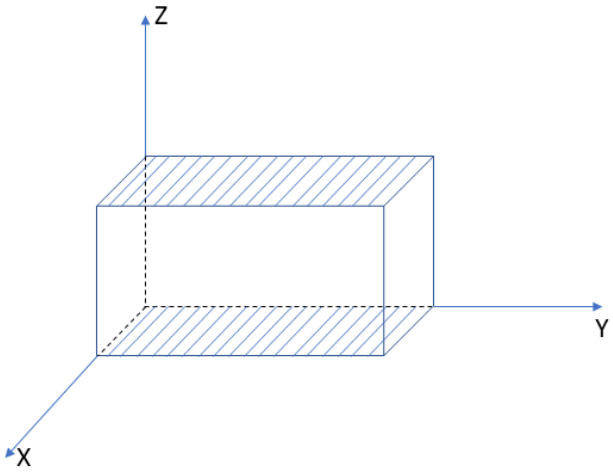

Figure 4-3 3D print Fabrication direction.

According to the previously described testing methodology, three test groups were collected for samples 1,2 &3 from the 3D print stainless steel for data analysis. Following the time-resolved defocusing methodology in section 3.5.1, the test will give us two graphs to analyze. The first one will provide us with the gradual Rayleigh waves separation from the directly reflected wave, which is called the v(z,t) graph, and the second one will provide the slope plot of dz/dt, which indicates the linear relationship of z defocusing steps and t time delay hence which lead to extract the slope data (dz/dt) that can be used to calculate the Rayleigh Surface wave velocity. The graphs' samples are indicated in Figure 4-4, Figure 4-5, and Figure 4-6 below.

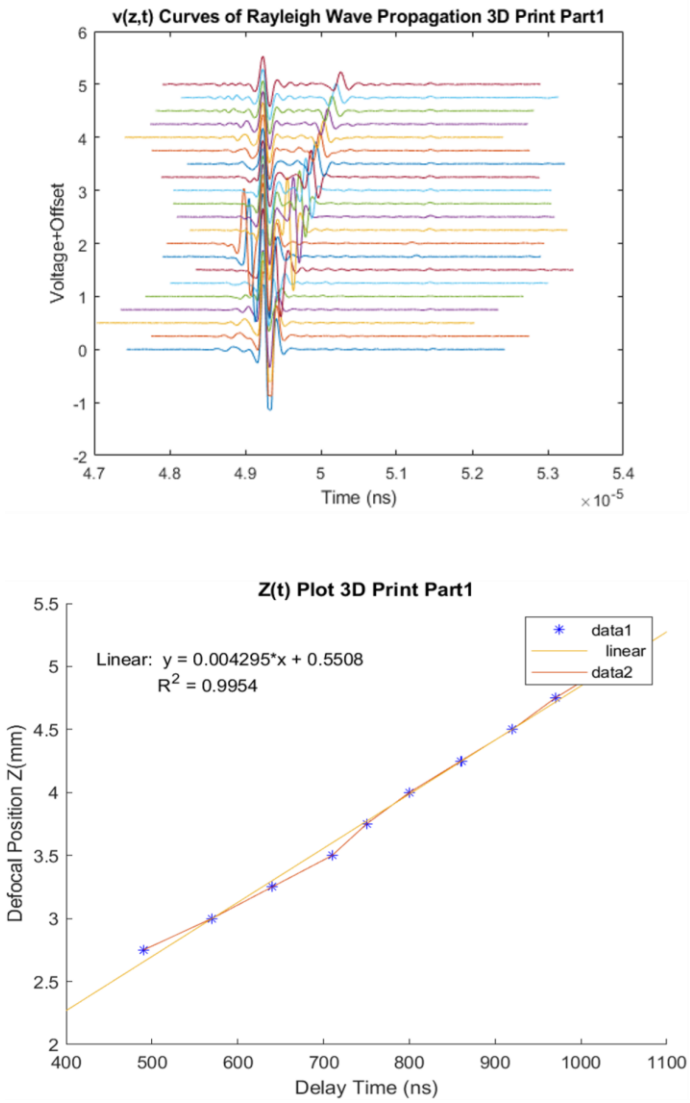

Figure 4-4 3D Print Sample 1 V(z,t) curves and Z(t) curve

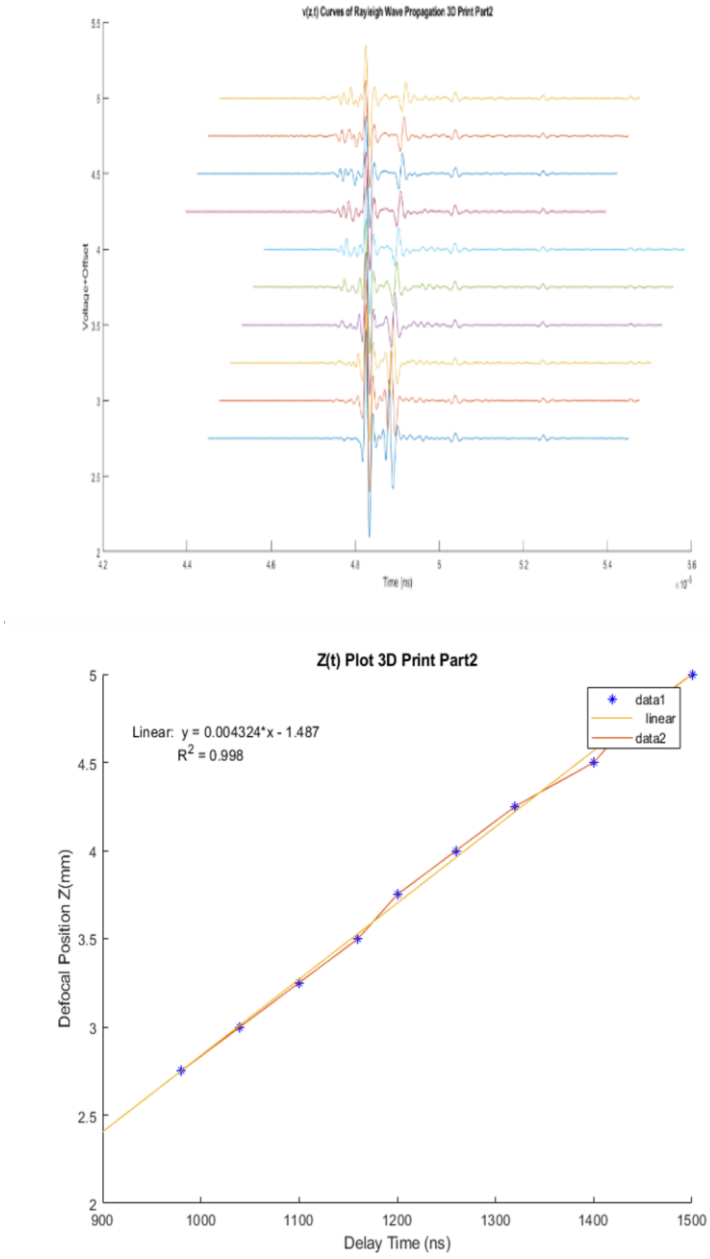

Figure 4-5 3D Print Sample 2 V(z,t) curves and Z(t) curve

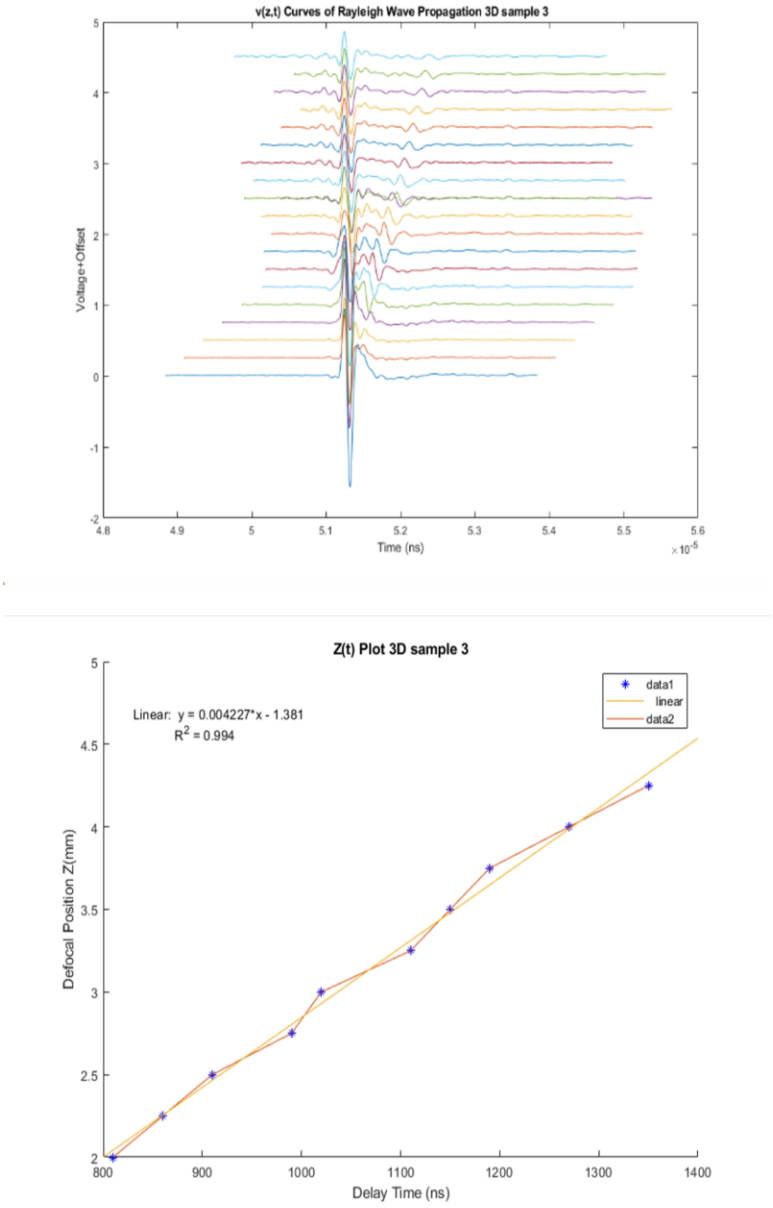

Figure 4-6 3D Print Sample 3 V(z,t) curves and Z(t) curve

Table 4-3: Measured Velocities and Elastic Properties' Calculation of 3D Print Samples

Sample#		Slope dz/dt	Density ρ (g/cm^3)	Measured Velocities (m/s)			Elastic Constants		
				Longitudinal Wave, V_L	Rayleigh Surface Wave, V_R	Shear-Transverse Wave, V_S	Young's Modulus, E (GPa)	Shear Modulus, G (GPa)	Poisson Ratio, ν
1	LFT3560	4.2949	8.00	5303.7	2637.3	2832.3	166.9	64.2	0.301
1	LFT2030	4.0615	8.00	5387.6	2571.7	2751.7	160.4	60.6	0.324
1	LFT3560	4.2046	8.00	5251.1	2612.1	2805.4	163.8	62.9	0.300
2	LFT3560	4.3241	7.92	5742.4	2645.5	2823.2	169.2	63.1	0.341
2	LFT3560	4.3266	7.92	5643.3	2646.2	2827.5	168.7	63.3	0.332
2	LFT3560	4.3295	7.92	5339.7	2647.0	2841.8	166.5	63.9	0.302
3	LFT2030	4.2271	8.11	5327.4	2618.4	2808.9	167.4	64.0	0.308
3	LFT3560	4.2227	8.11	5297.9	2617.2	2808.9	166.9	64.0	0.305
3	LFT3560	4.2222	8.11	5375.3	2617.0	2804.9	167.6	63.8	0.313

VL, VS, and VR measurements were calculated using the equation 4-13 and summarized in Table 4-3 and shown in Figure 4-7 with the measured densities for each sample. Based on the previous measurement of the wave velocities, the elastic constants were obtained and summarized in the same table.

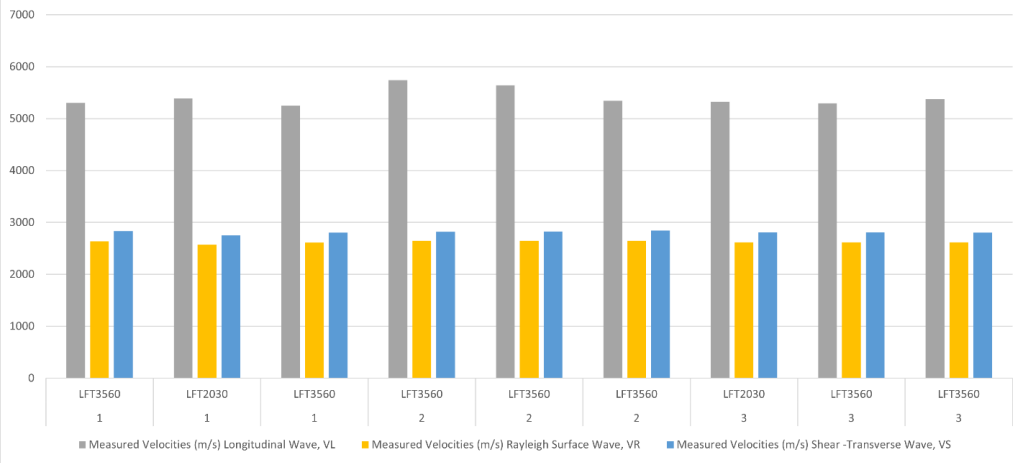

Figure 4-7: Wave Velocities VL, VR, and VS for 3D Print samples 1,2 &3

According to the results in Table 4-3, the average values of Young's Modulus, Shear Modulus, and Poisson's ratio of sample 1 were calculated represented in Table 4-4 are 163.70 GPa, 62.57 GPa, and 0.31.

Table 4-4 Average Wave Velocities and Elastic Constants for 3D Print Samples 1,2 &3

Sample#	Density ρ (g/cm^3)	Measured Velocities (m/s)			Elastic Constants		
		Ave. Longitudinal Wave, V_L	Ave. Rayleigh Surface Wave, V_R	Ave. Shear -Transverse Wave, V_S	Ave. Young's Modulus, E (GPa)	Ave. Shear Modulus, G (GPa)	Ave. Poisson Ratio, ν
1	8.00	5314	2607	2796	163.70	62.57	0.31
2	7.92	5575	2646	2831	168.13	63.43	0.33
3	8.11	5334	2618	2808	167.30	63.93	0.31
overall average					166.38	63.31	0.314

Additionally, to ensure the consistency of the results, the relative standard deviation was calculated, resulting in 1.99%, 2.91%, and 4.40%, respectively, which approves the consistency and precision of the method used to calculate the wave velocities and mechanical characteristics. The rest of the averages for each sample and the relative standard deviation is depicted in Table 4-5 below. The relative standard deviation does not exceed 10%, which is an acceptable margin, and therefore, the next step will be analyzing all the data in Table 4-3 by taking the overall averages of the elastic properties. They are 166.38 GPa for Young's Modulus with a relative standard deviation of 1.42%, while 63.31 GPa for Shear Modulus with a relative standard deviation of 1.09% and 0.31 for Poisson's Ratio with a relative standard deviation of 3.03% as it is shown in Figure 4-8.

Table 4-5: relative Standard Deviation for 3D print Stainless Steel 316L

relative standard deviation	Young's Modulus, E (GPa)	Shear Modulus, G (GPa)	Poisson Ratio, ν
sample1	1.99%	2.91%	4.40%
sample2	0.85%	0.66%	6.28%
sample3	0.22%	0.18%	1.31%

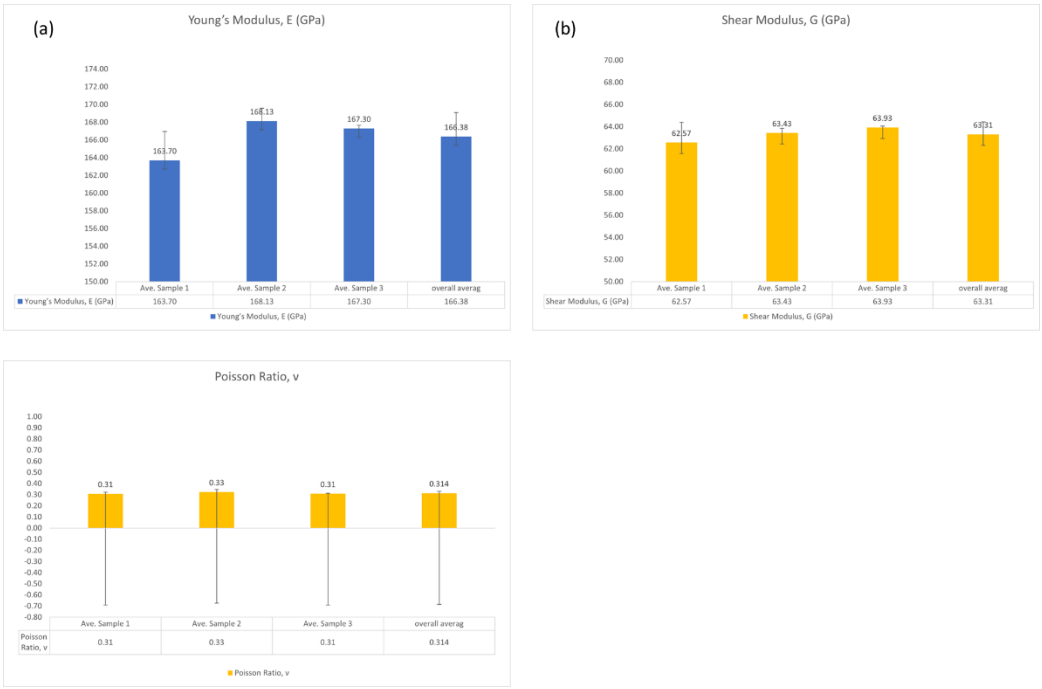

Figure 4-8: (a) Average Young's modulus E (GPa), (b) Average Shear Modulus G (GPa) and Poisson's Ratio v for 3D Print Samples number 1,2 and 3 and the overall average for each Elastic Constants represented in fourth bar Using Line Focus Transducer

moreover its known from the standard material properties of Stainless steel 316L the young modulus is 190 GPa ±18 while fabricated by Additive manufacturing the range for Young's modulus is between 160-182 GPa with an average of 171GPa, while for the Shear modulus its ranging between 62-80 GPa with an average of 70 GPa and for the Poisson ratio its ranging between 0.260-0.303 with an average of 0.29 [52]. Although Young's modulus measured is within the range of standard data provided, comparing it to the maximum value, acceptable reasoning can be related to many factors affecting the wave velocity. One of them is that the porosity of the 316L stainless steel samples is higher than standard samples, which causes the wave propagation to have more energy dissipation and hence the wave velocity drops significantly, and that can be shown in

this study since the standard Longitudinal wave velocity in the standard sample should be around 5800m/s. At the same time, the VL measured recorded around 5380 m/s, an error of 7.81%.

The error of the methodology used by the Line focus transducer and from utilizing the time-resolved defocusing method analysis for Young modulus is about 2.7%, while for the shear modulus, the error was 9.56%, and for the Poisson ratio, the error from actual value is about 6.9%. Since the overall uncertainty for Additive Manufacturing Stainless Steel 316L calculated previously in Chapter 3 is between 12-13%, that is considered within the acceptable range of error, which proves that overall, the Line Focus Transducer ultrasound system with this accuracy is a capable methodology to characterize isotropic material elastic properties.

4.5 Conclusion

In Summary, there is no significant fluctuation of results that appears within these nine tracks of testing. Also, the system shows a good repeatability of the final average results within the range of error percentage calculated from the uncertainty of commercial materials. The most important values, Young's modulus, Shear modulus, and Poisson's ratio, "Elastic Constants," shows a significant accuracy to the standard values provided by the manufacturer. Except for the outlier figures shown in Table 4-3 from sample 2, where the longitudinal velocity measured were higher than the other samples in first and second reading out of three total readings, this could be the result of internal crack or vacuum in the sample caused the wave to reflect faster than usual. This discrepancy cannot be controlled by the time resolved defocusing method since it is more related to the fabrication and sintering process controlled by the additive manufacturing process. To avoid such a discrepancy in the future, more data collection and tests can be done instead of three testing for each sample, which will guarantee to reduce of the fluctuation in the total average of the wave velocity, which will impact the elastic constants results to be more consistent with the other samples. In general, the elastic constants of the AM SS360L bars were measured using the nondestructive testing via using the line focus ultrasonic system that proved to generate surface waves such as Rayleigh surface wave and direct waves from line focus transducer and then measuring the velocity of those waves using the time-resolved defocusing method utilizing the v(z,t) waveform is a reliable method to characterize and estimate the elastic constants of an isotropic material such as AM materials, not only that but also uncertain metal alloys materials can be defined and classified according to this methods as it will be shown in the next chapter for Bulk metallic Glasses metal alloys.

5.0 Validating The Fabricated Lens-Less Line Focus Transducer By Identifying New Bulk Metallic Glasses Material

This chapter presents the results of an extensive investigation into the characterization of Bulk Metallic Glasses (BMG) using the Lens-Less Line focus Transducers LFT2030 and LFT3560. As outlined in Chapter 3, the methodology was applied to two different BMG samples, resulting in eight data sets that comprehensively understand these materials.

The chapter's first part focuses on identifying and measuring Rayleigh waves in the BMG samples. The data obtained from this process revealed a clear separation of Rayleigh surface waves from Direct Waves, a critical aspect in understanding the properties of these materials.

The second part of the chapter delves into the characterization of the BMG materials using the validated Line Focus Transducer system. Each transducer was used to collect two sets of data from each sample, resulting in a total of eight data sets. These data sets were then analyzed to calculate the velocities of the Rayleigh surface waves and other essential parameters.

The third part of the chapter presents the results of time domain waveform analysis conducted on the first sample, $Ni_{63.09}Nb_{16.71}P_{10.05}Cr_{7.48}Si_{2.31}Al_{0.36}$. This analysis led to the calculation of wave velocities and Elastic constants, providing valuable insights into the properties of the sample.

The fourth part of the chapter discusses the analysis of the second sample, $Zr_{67}Cu_{12}Ti_{11}Ni_{9}$. Despite the presence of a crack in the sample, consistent results were obtained, further validating the effectiveness of the transducers.

The final part of the chapter compares the calculated elastic constants with standard BMG alloys, further validating the measurements. Despite the inherent challenges in characterizing

BMGs due to their complex nature, the measurements were in good agreement with the standard values, demonstrating the reliability of the methodology.

This chapter, therefore, provides a comprehensive analysis of the BMG samples, contributing to the broader understanding of their structure-properties relationship. The findings highlight the accuracy and reliability of the Line Focus Transducers LFT2030 and LFT3560 in collecting data for new materials, demonstrating their potential for broader applications in material science.

5.1 Bulk Metallic Glasses

5.1.1 Background & History

Amorphous metallic alloy is considered a new noncrystalline material compared to the amorphous material group [53]. Reaching the amorphous structure can be achieved by combining different sizes of atoms of different complex alloying elements under rapid cooling while transitioning from melt or liquid phase to solid phase, which will result in the formation of the glassy structure, as shown in Figure 5-1: Schematic time-temperature-transformation (TTT) diagram showing direct casting and thermoplastic forming processes of BMGs. The rapid cooling's importance reflects the requirement to limit the metallic atoms from combining into the lattice structure found in conventional metals [53]. The requirements of critical cooling rate limitations rise, such as the size of the final product and its forms, typically thin ribbons, foils, and wires. What characterizes that kind of metal is its unique features, amorphous microstructure, and distinctive mechanical properties. The absence of dislocations and no plasticity is exhibited in the Bulk metallic glasses, which results in very high yield strength and elastic strain limits due to the absence of material flow.

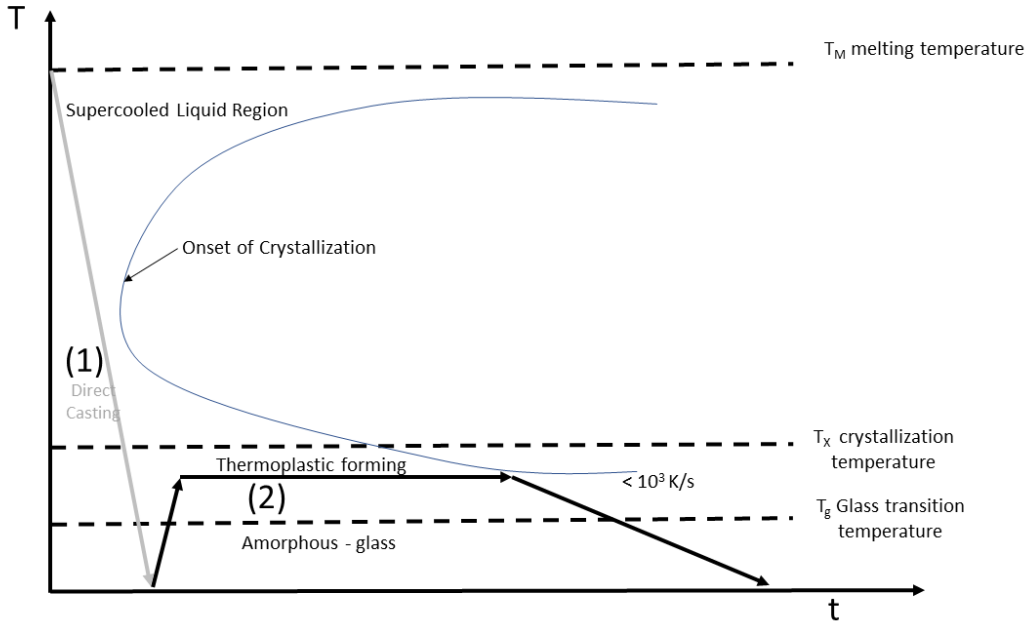

Figure 5-1: Schematic time-temperature-transformation (TTT) diagram showing direct casting and thermoplastic forming processes of BMGs.

The first reported metallic glasses were in 1960 at Caltech, the USA, by Duwez; the alloy was Au75Si25 [54], and by developing rapid quenching techniques for cooling the metallic liquid at very high rates, reached 105 – 106 K/s. in the late 1980s a massive leap of development in the field of amorphous materials enabled the casting of the amorphous metals with more excellent dimensions greater than 1mm. It is formally defined in the community of metallic glasses that the dimension of these materials above 1mm would be considered as “bulk”: these are known as bulk metallic glasses (BMGs). While the first bulk metallic glasses were ternary Pd-Cu-Si alloy produced in 1974 by Chen [55], it was rods with few millimeters produced at a cooling rate of 103 K/s. Recently, Die casting, a standard methodology for the net shape process of BMG and superplastic forming (SPF), has been used to produce small features with thin sections and high aspect ratios that lead to being used in microelectromechanical systems, medical and optical

applications, and data storage [56]. As of Today, the largest BMG made is 80mm in diameter and 85mm in length, as reported by Nishiyama in 2012 [57]

BMG alloys tend to comprise an excellent glass-forming ability (GFA) combined with distinctive chemical, mechanical, and physical properties, and They were developed in several systems like Ti-, Al-, Mg-, Zr-, Fe-, Ni- and Ln based alloys with a critical cooling rate less than 10^3 K/s and thickness above 1mm by conventional casting methods ([58, 59]). Following significant breakthroughs in Bulk Metallic Glasses (BMG), a new class of bulk metallic alloys with an amorphous structure has been integrated into commercial materials since the mid-1990s until our time now.

5.1.2 Characteristics Of Bulk Metallic Glasses & Classification System

5.1.2.1 BMG Characteristics

The Bulk Metallic Glasses (BMGs) exhibit an exceptional property of high strength (The BMGs have the unusual combination of high yield stress σ_y and low young modulus E.) with high yield strain and extraordinary resilience (measure of material ability to store elastic energy) were the BMG capable of storing extra elastic energy at minimum volume compared to 1500 metals and traditional crystalline alloys were the elastic limit σ_y and Young's modulus E represented. as it can be seen Figure 5-2 the BMG is laying on top of the other conventional engineering materials, With a high correlation to Young's modulus [60].

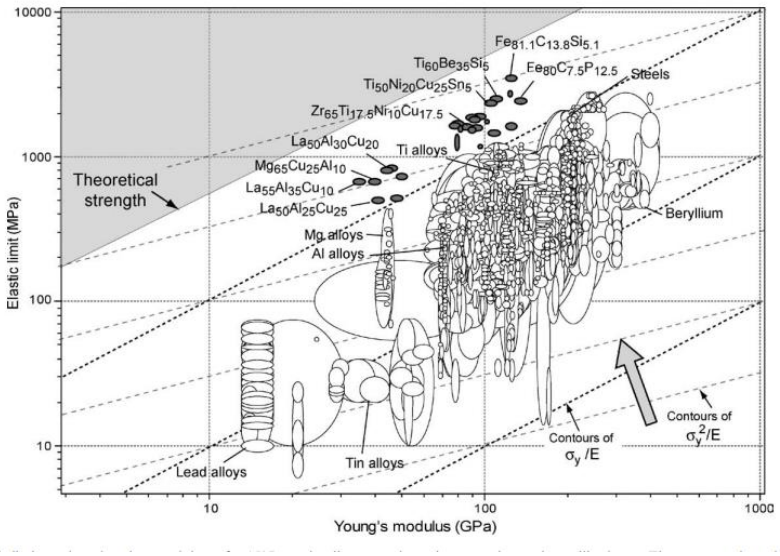

Figure 5-2: Elastic Limit (strength, sigma y) plotted against Young's modulus E for Bulk metallic glasses [61].

The findings suggest a negative correlation between resilience and the loss coefficient, indicating that localized plastic deformation plays a crucial role in energy dissipation. In the present context, metallic glasses are exceptional since they exhibit a high resilience and reduced damping, making them a highly desirable option for systems that utilize vibrating reeds, such as gyroscopes. Additionally, they are well-suited for applications that require the transmission of elastic waves [61]. So, in general, Bulk metallic glasses are well known for their superior high strength and hardness, higher elastic elongation, desirable high viscous flow workability, better smooth surfaces, good light reflectivity, high resistance to oxidation, wear, and corrosion, large ductility in bending with low coefficient of friction [62] &[63, 64]. However, the downside of BMG is plastic deformation that concentrates within the shear bands that varies between 10-20 nm thickness, with a plastic flow along that shear bands [65, 66] due to the absence of crystallographic slip dislocation, which prevents BMG from having homogenous deformation instead they have shear banding deformation causing BMG to be more brittle and might cause a catastrophic result [67] and [68].

5.1.2.2 BMG classification system

As for the BMG classification, there have been many ways to classify it, and the best classification system was done by Prof. Inoue, where he proposed that BMG can be classified into three main types, Figure 5-3,

1. Metal-Metal Type
2. Pd-Metal-Metalloid Type
3. Metal-Metalloid Type

That classification was based on which metal group would react with the other group to transform into a glassy structure chosen using several rules, such as chemical affinity, atomic size, and electronic configuration. In Inoue et al. they proposed an atomic arrangement, size, and crystal structure [69].

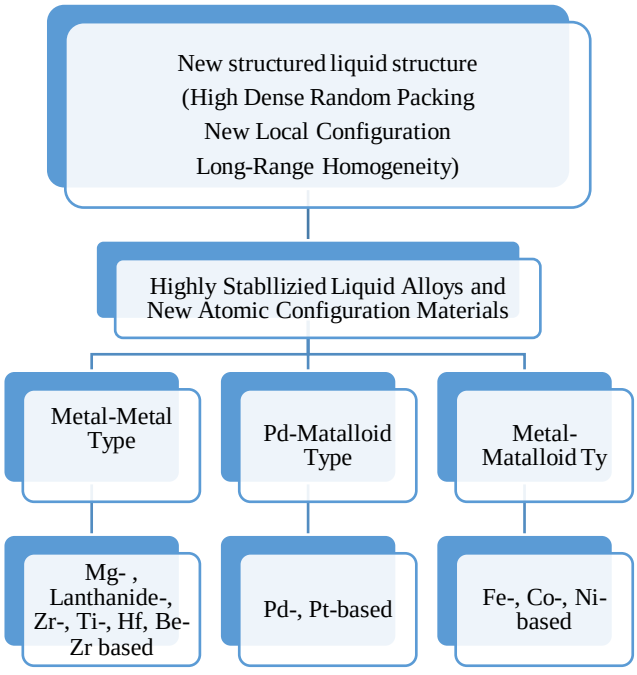

Figure 5-3: classification of BMGs by Inoue and Takeuch[73]

5.1.3 BMG Applications

Due to all the material properties, we mentioned about the Bulk metallic glasses, they have the potential to be utilized in many fields starting, including biomedicine [70], machinery structural materials (high-performance springs), aerospace [71], nuclear reactors [72] and sports goods such as (golf clubs, skis, and skates). Tooling, especially knife edges, due to BMG's higher hardness property. Also, applications such as diaphragms in pressure sensors [73] and springs, as we mentioned earlier since the BMG can endure and store high elastic energy per unit volume with low damping, which is a good attribute for springs features since it has been proven to offer an excellent material for microelectromechanical systems (MEMS) devices due to high yield strength, extreme hardness, greater resilience, and strong corrosion resistance, not only that but the capability to mold these materials in a fine scale that is desirable in this field, with a proof of concept were the metallic glasses used instead of silicon as hinges for rotating micro mirrors in digital light processor DLP devices without fatigue failure at 10^{12} cycles [74] and used as a spring actuator that was proposed by [75] as shown in Figure 5-4.

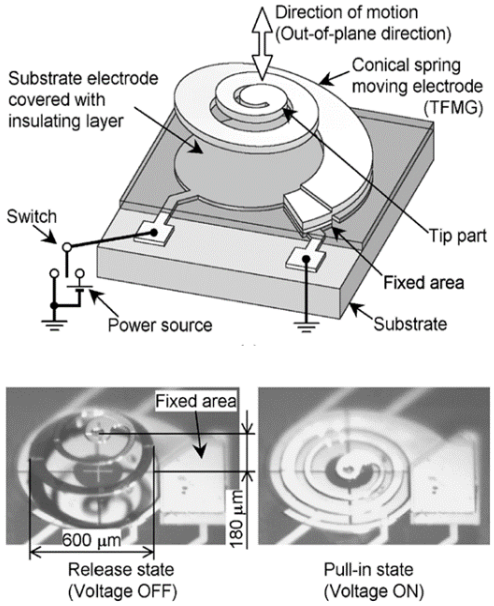

Figure 5-4: Conical Spring Micro actuator, spring is 7.6Microm thick film of Pd76Cu7Si17 metallic glass [75].

The material we choose in our research falls under the metal-metal type, which is Zr- and Ni-Based alloys, due to the unique mechanical properties that Zr- & Ni-based alloys comprise, such as the high yield strength and high elastic strain limit. It has shown a high promising application potential in some of the applications shown in Table 5-1.

Table 5-1 Application Fields presented with BMG in Japan [76]

Application Fields that have been presented for BMG
1. Structural materials
2. Sensor materials
3. Precision machinery materials
4. Optical materials
5. Spring materials
6. Sporting goods materials
7. Wear-resistant coating materials
8. Precision nozzle materials
9. Corrosion-resistant materials
10. Magnetic materials
11. Microtechnology materials
12. Nanotechnology materials
13. Information data storage materials
14. Biomedical materials
15. Medical instrument materials
16. Fuel cell separator materials

As it is known, zirconium and Nickel-based alloys demonstrate remarkable thermal stability, outstanding corrosion resistance, and excellent mechanical properties [77-80]. finding about Zr-based alloys, which showed an excellent tensile property with fracture strength ranges between 1.4-2 GPa with a tensile elongation up to 2 pct. On the other hand, the findings verified by [78] were he proved that Ni-based alloy reached a flow stress 3 GPa fracture strength with a plastic failure region of 6.5%. Also, the findings by [79]) that Ni-based alloy $(Ni_{60}Nb_{40-x}Ta_x)_{0.95}P_5$ alloy in a corrosion medium of 12 kmol/m^3 HCL has almost a zero-weight loss.

5.2 BMG Material Composition

Two primary samples of BMG were used in this test, as shown in Figure 5-5 and Figure 5-6; sample 1 had a rectangular shape, While sample 2 was built in a hexagonal shape. These two samples were used as a test material for marine and army applications such as armor-piercing shields.

Figure 5-5: Bulk Metallic Glasses Sample 1 - Bulk sample - Ni-based alloy

Figure 5-6: Bulk Metallic Glasses Sample 2 - Cracked sample - Zr-based alloy

The samples components were verified utilizing the EDS system in the Nanoscale Fabrication and Characterization Facility using Scios 2 DualBeam (an ultra-high-resolution analytical focused ion beam scanning electron microscopy (FIB-SEM) system), which utilizes the energy-dispersive spectroscopy (EDS) for compositional information. Plus, the compositional raw material for samples one and two are shown in Table 5-2 & Table 5-3, respectively.

As can be seen and according to Inoue classification [76], sample 1 composition shows that BMG Is classified under the Metal-metalloid type as Nickle based since the Ni concentration is over 50% at%., while sample 2 was classified under Metal-Metal Type as Zirconium based due to Zr concentration over 60% at%. Noting that sample 1 tests were done four times due to some discrepancies in Ni compositions, while sample 2 tests were done only twice due to high confidence in Zr compositions matching in the two-spectrum analysis.

Table 5-2 : Sample1 Amorphous BMG 364gm raw material components

Spectrum label	Spectrum 1	Spectrum 2	Spectrum 3	Spectrum 4
Al	-	0.34	0.36	0.36
Si	2.52	2.7	2.31	2.2
P	9.98	10.09	10.05	10.28
Cr	8.37	8.24	7.48	7.62
Ni	59.77	58.8	63.09	62.74
Nb	19.36	19.83	16.71	16.79
Total	100	100	100	100

Table 5-3: Sample 2 Amorphous BMG 92gm raw material components

Spectrum Label	Spectrum 1	Spectrum 2
Ti	11.3	11.18
Ni	9.23	9.29
Cu	12.38	12.42
Zr	67.09	67.11
Total	100	100

According to the alloy composition extracted from the EDS system, we calculated the sample's Volume, Mass, and density accordingly. This information will be crucial in future calculations to measure the wave velocity among these new BMG alloys. Sample one was cut in SWANSON CENTER FOR PRODUCT INNOVATION using MV2400, the WIRE EDM machine. The sample Dimensions Length x Width x Height (thickness) mm was 40.28 mm x 31.09 mm x 17.14 mm, respectively, leading to a total volume of 21,464 mm^3, the mass was calculated mathematically and measured in an electronic scale with readability accuracy of 0.1mg /0.01mg, and it was 169.9842 grams, accordingly the density of the sample measured at 7.9193 kg/cm^3. While on the other hand, sample 2 had a particular shape (a hexagonal shape) with an edge length of 32.73mm and a thickness of 7.5mm. The volume was 20874 mm^3 while the mass mathematically and experimentally agreed in results to be 92.4928gm. From that information, the resulting density was 4.4310 kg/cm^3.

5.3 Experimental Procedure

The procedure used in this test will follow the same steps described in Chapter 3. The only change that happened in this test was the alignment of the samples since sample two suffered a defect crack on the back surface extending from the bottom edge to the upper edge going through the middle of the sample; the sample's face was facing the Line focus Transducer upward while the cracked surface on the bottom secondly the PVDF in the LFT was aligned with the sample surface away from the crack as shown in Figure 5-7 to avoid any distorted waves such as the direct wave that have a shorter time of flight through the whole thickness of the sample. That part was verified by testing the sample on different edges to ensure the Direct wave was consistent.

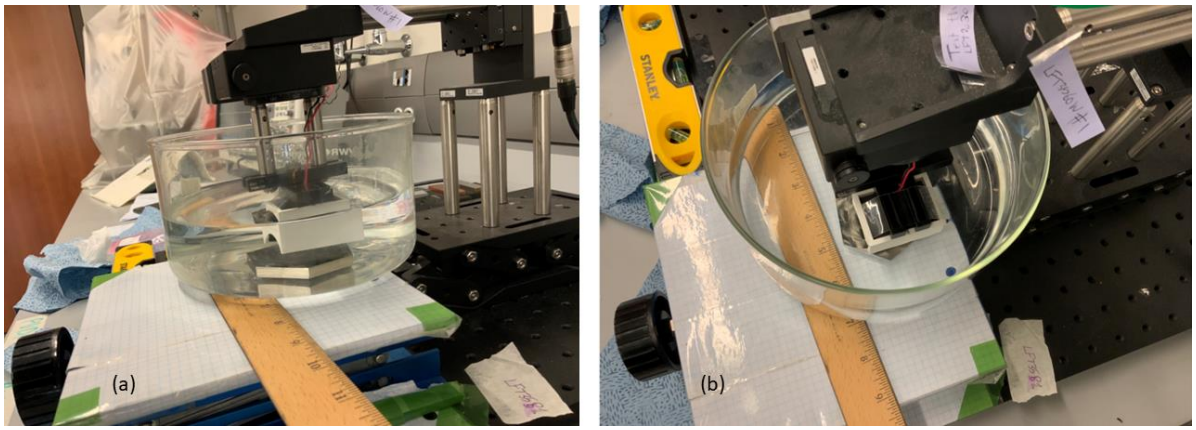

Figure 5-7: BMG Sample 2 - alinement under LFT avoiding crack area (a) Side View and (b) Top View

After this adjustment, the highest direct reflected wave amplitude was found, and their defocusing process will be applied by moving closer to the specimen following a constant increment in the step size. In these experiments, the step size was 0.2mm, and two designs gave the data for each sample. We built LFT3560 and LFT2030 to give enough representable

data and then averaged the results of Elastic constants such as Young's Modulus, Shear Modulus, Bulk Modulus, and Poisson's Ratio.

5.4 Results And Discussion

5.4.1 Wave Diagrams Of Sample 1 (Bulky) BMG

By using the same method described earlier in Chapter 3, a total of eight sets of groups of data were collected from the two samples of Bulk Metallic Glasses (BMG) using the two designed and fabricated Lens-Less Line focus Transducers LFT2030 and LFT3560. First, the V(z,t) wave curves were obtained and measured to identify Rayleigh waves. It shows the perfect separation of Rayleigh surface wave from Direct Wave. Secondly, the Z(t) plot was made according to the step size that showed the linear velocity relationship, which is proved by the slope calculations; based on these data, the Rayleigh surface wave velocities were obtained. Samples of the V(z,t) curves and Z(t) plots are shown below in Fig, while the rest of the graphs and curves will be added to the appendix.

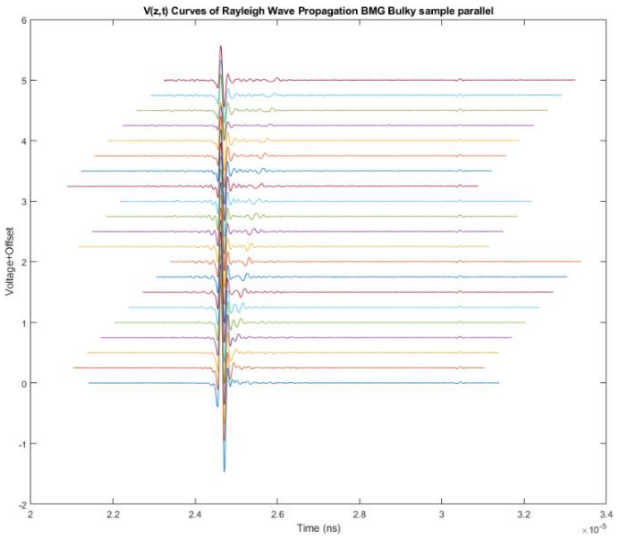

Figure 5-8 V(z,t) curves of BMG sample 1 with a step size of 0.2 - LFT2030

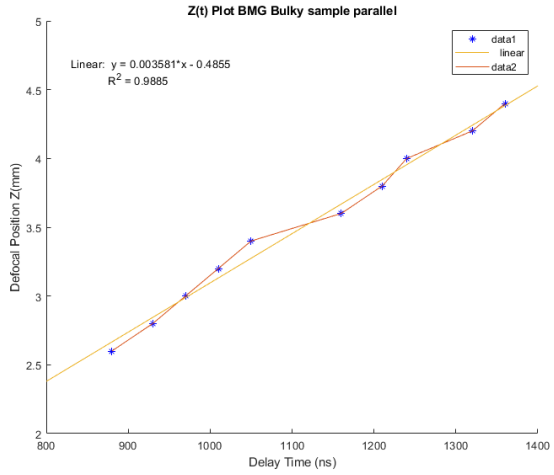

Figure 5-9 Z(t) plot of BMG sample 1 with a step size of 0.2 – LFT2030

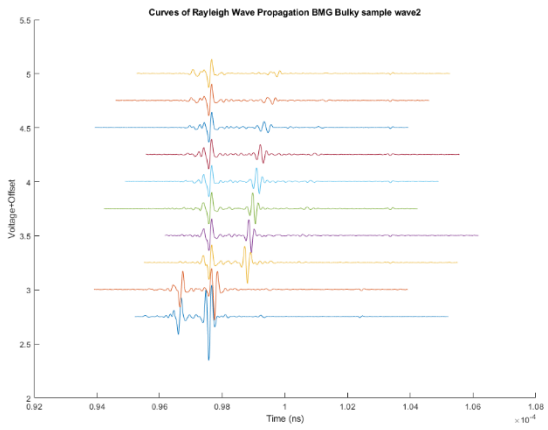

Figure 5-10: V(z,t) curves of BMG sample 1 with a step size of 0.2 - LFT3560

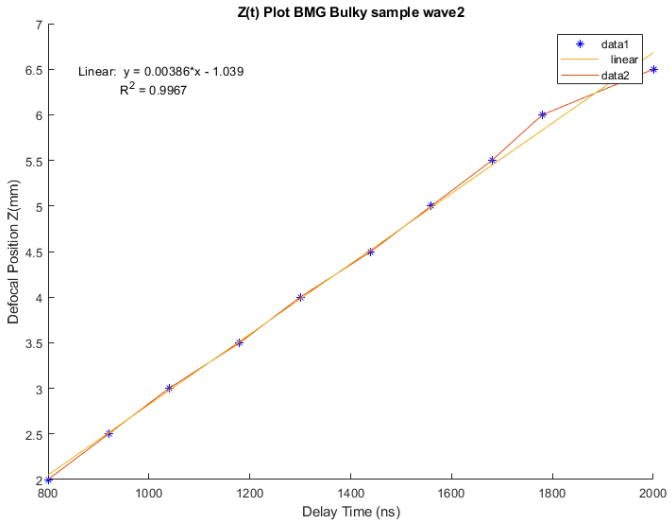

Figure 5-11:Z(t) plot of BMG sample 1 with a step size of 0.2 – LFT3560

5.4.2 Wave Diagrams of Sample 2 (Cracked) BMG

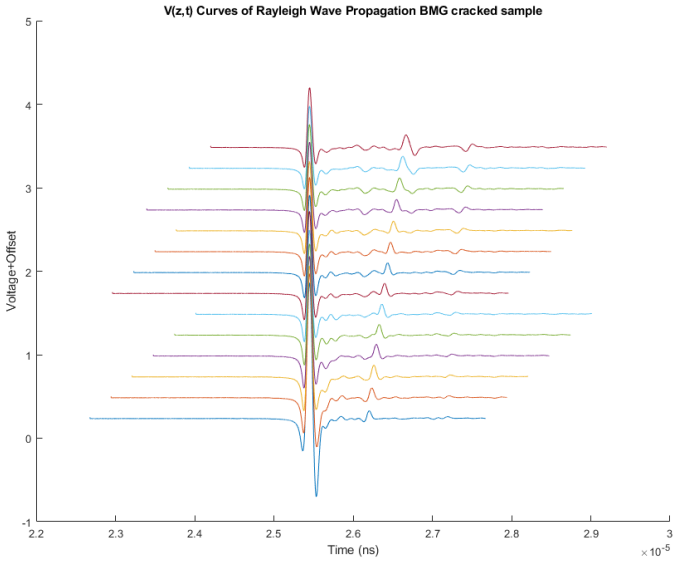

Figure 5-12: V(z,t) curves of BMG sample 1 with a step size of 0.2 - LFT2030

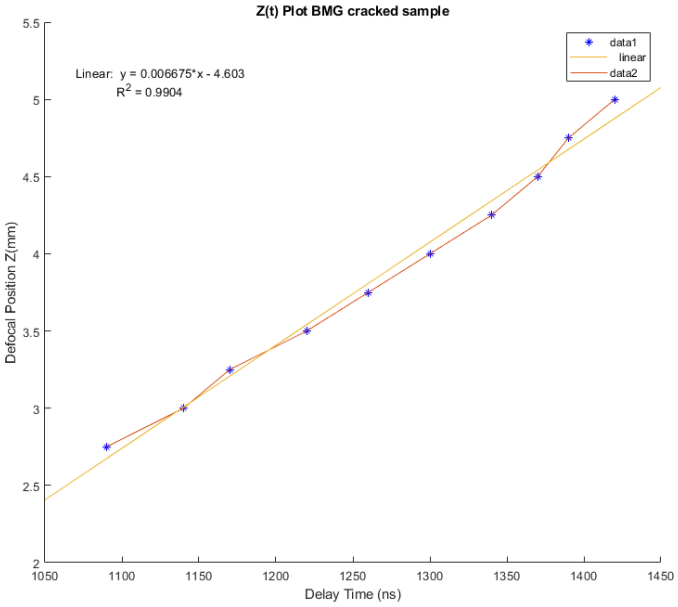

Figure 5-13: Z(t) plot of BMG sample 1 with a step size of 0.2 – LFT2030

5.4.3 Numerical Results & Discussion:

The validated Line Focus Transducer system was used to characterize the Bulk Metallic Glasses materials. Both Line Focus Transducers, LFT2030, and LFT3560, were used to collect data sets resulting in two data groups for each sample by each Transducer. So, in total, eight sets of data were collected. The measurement and calculation results are summarized in Table 5-4 and Table 5-6.

5.4.3.1 The measurement and calculation for Bulk sample number 1 with a Composition $Ni_{63.09}Nb_{16.71}P_{10.05}Cr_{7.48}Si_{2.31}Al_{0.36}$

Starting with sample 1 ($Ni_{63.09}Nb_{16.71}P_{10.05}Cr_{7.48}Si_{2.31}Al_{0.36}$), Hence; this sample is sometimes in this literature called a bulk sample since it has got 21mm thickness. After applying the time domain waveform analysis, the measured wave velocities V_L, V_R, and V_S were calculated, resulting in calculations of Elastic constants such as modulus of elasticity, Shear elasticity, Poisson's ratio, and the Bulk Modulus, and they are summarized in Table 5-4.

Table 5-4: Elastic Constants of BMG (sample 1) Ni-based

Sample#	LFT type	Slope dz/dt	Density $\rho(g/cm^3)$	Measured Velocities (m/s)			Elastic Constants			
				Longitudinal Wave, V_L	Rayleigh Surface Wave, V_R	Shear - Transverse Wave, V_S	Young's Modulus, E (GPa)	Shear Modulus, G (GPa)	Poisson Ratio, ν	Bulk Modulus, K(GPa)
1	LFT2030	4.49	7.919	5895.1	2691.2	2870.2	175.45	65.24	0.3446	188.23
1	LFT2030	4.59	7.919	5879.9	2720.2	2903.8	178.79	66.77	0.3387	184.76
1	LFT3560	4.53	7.919	5920.6	2.7013	2.8809	176.79	65.72	0.3449	189.96
1	LFT3560	4.50	7.919	5905.3	2.6935	2.8726	175.79	65.34	0.3450	189.03

The LFT2030 measurements for the sample1 lead to a slope of approximately 4.5 with average values for Longitudinal velocity of 5887.5 m/s, shear velocity of 2887.0 m/s, and a Rayleigh surface wave velocity which recorded 2705.7 m/s. While on the other hand, the LFT3560 transducer resulted in an average velocity of longitudinal velocity of 5912.9m/s, a shear velocity of 2876.8m/s, and a Rayleigh surface wave velocity of 2697.4 m/s. According to these average velocities and after applying equations in ch3 (3-12 to 3-14) previously mentioned, the elastic constants were calculated as shown in Table 5-4; as it can be seen from the initial results, we had a very close range of data set in each elastic constant, but we further calculated the average values for each constant to give more representable data.

The average values of modulus of Elasticity, shear modulus, poison's ratio, and Bulk modulus, which resulted from LFT2030, were 177.12 GPa, 66.01 GPa, 0.34, and 186.49 GPa, respectively, while for the same sample but with using LFT3560 it was 176.29 GPa, 65.54 GPa, 0.34 and 189.49 GPa respectively as well. The absolute values of each elastic constant beside the averages from both Line Focus Transducers were equal with minor -if not negligible- discrepancy

since the relative standard deviation for sample1 – Bulk BMG as shown in Table 5-5, which shows an excellent consensus of both transducers (LFT2030 and LFT3560) and their accuracies in reading and collecting data for new materials such as Bulk Metallic glasses. Only one notice that LFT3560 had more accurate results and lower relative standard deviation than LFT2030 and that mainly can be referred to the angle of aperture of the LFT3560, which in total has 50 degrees allowing the system to collect better signal compared to only 40 degrees for LFT2030 but still the overall values are beyond satisfactory for both transducers.

Table 5-5: Relative standard deviation for sample1 – Bulk BMG using LFT2030 and LFT3560

Relative standard deviation	Young's Modulus, E (GPa)	Shear Modulus, G (GPa)	Poisson Ratio, ν	Bulk Modulus, K (GPa)
Sample1 – LFT2030	1.33%	1.65%	1.22%	1.32%
Sample1 – LFT3560	0.40%	0.41%	0.02%	0.34%

5.4.3.2 The Calculation For Cracked Sample No.2 With A Composition Of $Zr_{67}Cu_{12}$ $Ti_{11}Ni_9$

For the second test, We studied sample 2 (hence, $Zr_{67}Cu_{12}$ $Ti_{11}Ni_9$), In this sample study, we had slight variations in measuring the wave velocities, especially determining the direct wave reflecting from the face and the back wall of the sample since this sample already had a crack but with some alignments avoiding the crack and focusing on one edge as shown in Figure 5-7 we had a consistent result with both line focus transducers we used. In addition, by applying the time domain waveform analysis, the measured wave velocities VL, VR, and VS were calculated, resulting in calculations of Elastic constants including the modulus of elasticity, Shear elasticity, Poisson's ratio, and Bulk Modulus, and they are summarized in Table 5-6.

Table 5-6 Elastic Constants of BMG (sample 2) Zr-based.

Sample#		Slope dz/dt	Density ρ (g/cm^3)	Measured Velocities (m/s)			Elastic Constants			
				Longitudinal Wave, V_L	Rayleigh Surface Wave, V_R	Shear - Transverse Wave, V_S	Young's Modulus, E (GPa)	Shear Modulus, G (GPa)	Poisson Ratio, ν	Bulk Modulus, K
LFT2030	Cracked edge1	4.0311	4.4310	5.5046	2.5630	2.7372	88.6912	33.1990	0.3358	89.9964
LFT2030	Cracked edge 1	4.0720	4.4310	5.4995	2.5747	2.7508	89.3989	33.5287	0.3332	89.3108
LFT3560	cracked	4.0226	4.4310	5.6285	2.5606	2.7303	88.9303	33.0315	0.3461	96.3333
LFT3560	Cracked	4.0052	4.4310	5.6285	2.5556	2.7247	88.6181	32.8953	0.3470	96.5149

Starting with LFT2030 measurements for the sample2, we got a slope value of 4 with calculated average velocities V_L, V_S & V_R, respectively; the Longitudinal velocity amounted to 5502.1m/s, the shear velocity was 2744 m/s, and a Rayleigh surface wave velocity recorded an average of 2568.9 m/s. However, for the LFT3560 transducer results, we ended up with an average longitudinal velocity of 5628.5m/s higher than the previous result, a shear velocity of 2727.5m/s which is very close to the result from LFT2030, and a Rayleigh surface wave velocity averaged to 2558.1m/s that is almost similar to the result given by LFT2030.

According to these average velocities and after applying the elastic equations in ch3, the elastic constants were calculated as shown in Table 5-6; the average modulus of Elasticity, shear modulus, and poison's ratio resulted from LFT2030 were 89.05 GPa, 33.36 GPa and 0.33 respectively, while for LFT3560 it was 88.77 GPa, 32.96 GPa and 0.35 respectively as well. With a relative standard deviation of 0.56% for Young modulus, 0.70% for shear modulus, 0.55% for Poisson's ratio and 0.54% for bulk modulus while it was 0.25%,0.29%, 0.18% and 0.13% for Young's modulus, shear modulus, Poisson's ratio & bulk modulus respectively for LFT3560,

again confirming and indicating the outstanding consensus of both transducers LFT2030 and LFT3560 and their accuracies in reading and collecting data for new materials.

5.4.3.3 Validation Of Measurement Using Standard Data Library

The main challenge arises in our study and concern that we had to confirm these results' accuracy and authenticity; we had to compare our results to standard Bulk metallic glasses or commercial BMG alloys available in the market. Nevertheless, due to challenges regarding the metallic glasses material, such as how metallic liquid starts and the metallic glass phase begins, why liquid suddenly approaches glass transition temperature Tg? what factors determine the Glass-forming ability (GFA), why the barrier created by the ambiguity raised from a metastable phase of metallic glasses including the avoid of crystallization during processing which limits the commercial and industrial applications. Also, due to the lack of understanding of atomic arrangements in supercooled metallic liquid other challenges arise around the physical and mechanical properties of metallic glasses. All these factors lead to difficulties in having a proper classification system. Not only that, but the wide variety these alloys can be designed in with their randomly disordered structure can lead to challenges in metallic glasses characterization, which can be another issue in understanding the structure-properties relationship of these alloys [80-87].

According to all these uncertainties, our approach to BMG comparison to standard BMG in this research will be more related to the Bulk Metallic Glasses based alloy's groups, not to a specific BMG alloy. So, for our sample no.1 (hence, $Ni_{63.09}Nb_{16.71}P_{10.05}Cr_{7.48}Si_{2.31}Al_{0.36}$), which consists of the majority of Nickle-based alloy around 60%, we will compare this sample's wave velocities and elastic properties to the mechanical properties related to Ni- Based alloy group. In contrast, for sample no.2 (Hence, $Zr_{67}Cu_{12}$ $Ti_{11}Ni_{9}$), which consists of a Zirconium majority of

around 67%, we will compare the sample's elastic properties to the mechanical properties of the Zr-based alloy group.

In this research, we build our comparison to the standard and comprehensive compiled results of Ni- and Zr-based alloy elastic and mechanical properties that were done by Professor W.H. Wang [88] since his research study included review and measurement of almost all the Bulk metallic glasses' available including their elastic properties, elastic models, physical and mechanical properties, by utilizing different methods but mainly experimental acoustic measurements and various ultrasonic methods which resulted in reliable and abundant data such as transverse, longitudinal acoustic velocities, densities and elastic constants that shows a considerable correlation with a weighted average of the elastic constants of the constituent elements [88].

Firstly, the primary base element for samples 1 and 2, Ni-based and Zr-based alloy BMG, respectively, at room temperature, were given as shown in

Table 5-7, which gives an initial indication of the elastic constant values we expect from the BMG.

Table 5-7 the elastic constants (Young's modulus, E, shear modulus, G, Poisson's ratio, ν and Bulk modulus, K) and density, ρ, for the major base element of BMG sample 1 – Ni-based alloy – [89, 90]

Element	E(GPa)	G(GPa)	ν	K(GPa)	ρ (g/cm3)
Ni	200	76	0.31	180	8.902
Zr	68	33	0.34	-	6.508

Also, the experimental measurement and calculations for sample 1, a Ni-based alloy, had been mentioned previously, but since we want to compare the measured results with standard results, we will briefly mention it below, which is summarized in Table 5-8. The measured results were as follows, the young modulus ranged between 175-178 GPa with an average of 176.70 GPa, the Shear Modulus ranged between 65-66 GP with an average of 65.77 GPa, the Poisson's ratio was between 0.33 and 0.35 with an average of 0.34 and lastly, Bulk modulus between 184-189 averaging to 187.99 GPa. On the other hand, the Ni-based alloy group correspondent to these values was as follows, the Modulus of elasticity was between 161 to 183 GPa with an average of 172GPa, for the shear modulus, it was 66.3 GPa while the Poisson's ratio was 0.357 and the Bulk modulus of 129.6 up to 267 with an average of 198.3 GPa.

Table 5-8: range values of Elastic constants for sample 1 compared to Ni-based BMG alloy [89, 90].

Element	E(GPa)	G(GPa)	ν	K(GPa)	ρ (g/cm3)
Sample 1 Measured	175-178	66	0.33-0.35	184-189	7.919
Standard Ni-based BMG alloy	161-183	66.3	0.357-0.385	129.6-267	6.4-9.24

Likewise, for sample 2, the Zr-based BMG alloy, the elastic constants have been summarized in Table 5-9 for sample and standard BMG alloys. The sample measured Young's modulus was ranging between 88.61-89.39 GPa with an average of 88.91 GPa, the Shear Modulus ranging between 32.89 – 33.53 GP with an average of 33.16 GPa, the Poisson's ratio was in between 0.33 – 0.36 with an average of 0.35 and lastly Bulk modulus between 96.33-96.52

averaging to 96.42 GPa. On the other hand, the Zi-based alloy group (standard values) correspondent to these values was as follows, the Modulus of elasticity was between 77.3 to 97.3 GPa with an average of 87.3 GPa, for the shear modulus ranging between 28.2 to 35.9 GPa with an average of 32.05 GPa while the Poisson's ratio is ranging from 0.3550 to 0.377 with an average of 0.366 and the Bulk modulus of 92.9 up to 102.1 GPa with an average of 97.5 GPa, according to data extracted from [88] W.H. Wang's research about elastic properties of based alloys metallic glasses.

Table 5-9: range values of Elastic constants for sample 1 compared to Zr-based BMG alloy[89, 90].

Element	E(GPa)	G(GPa)	ν	K(GPa)	ρ (g/cm3)
Sample 1 Measured	88.61 – 89.39	32.89 – 33.53	0.33 – 0.35	96.33 – 96.52	4.0311
Standard Zr-based BMG alloy	77.3 – 97.3	28.2 – 35.9	0.35– 0.38	92.9 – 102.1	6.27 – 6.82

These sets of data and information guided us to calculate the error margin for each elastic constant and had them as follows, for sample 1 Ni-based BMG, Young's modulus was -2.74%, while Shear modulus was 0.79%, Poisson's ratio was 3.84%, and lastly, the Bulk modulus was 5.2%. The same calculation was carried out for sample 2 Zr-based BMG; Young's modulus error was 1.84%, the shear modulus error was 3.47%, Poisson's ratio was 4.37%, and the Bulk modulus error was 4.58%. Since our highest error does not exceed 5%, we can say that our confidence in this set of data is 95%, and by extracting the error margin between the two sets of data, a prediction interval for each elastic constant can be made based on the measured and calculated results, Using

the t-scores of 95% confidence interval we ended up with a validated range of results for elastic constants, as shown in Table 5-10.

Table 5-10: statistical prediction range for Elastic constants

	Young's Modulus (GPa)	Shear Modulus (GPa)	Poisson's Ratio	Bulk Modulus (GPa)
Sample 1	[174.3 - 179.1]	[64.66 – 66.89]	[0.3384 – 0.3482]	[184.4 – 191.6]
Sample 2	[88.35 – 89.47]	[32.73 – 33.59]	[0.3293 – 0.3517]	[86.80 – 99.28]

5.5 Conclusion

Utilizing the approach outlined in Chapter 3, we collected eight sets of data from two Bulk Metallic Glasses (BMG) samples using the Lens-Less Line focus Transducers LFT2030 and LFT3560. The data collection process involved the identification of Rayleigh waves and the calculation of their velocities. The Line Focus Transducer system was then employed to characterize the BMG materials, with each transducer collecting two data sets per sample, resulting in eight complete data sets.

The first sample, $Ni_{63.09}Nb_{16.71}P_{10.05}Cr_{7.48}Si_{2.31}Al_{0.36}$, was subjected to time domain waveform analysis, yielding calculated wave velocities and elastic constants. The LFT2030 and LFT3560 transducers provided similar results, with minor discrepancies, confirming their accuracy in data collection for new materials like BMGs.

Despite having a crack, the second sample, $Zr_{67}Cu_{12}$ $Ti_{11}Ni_{9}$ yielded consistent results with both transducers. The calculated elastic constants were compared with standard BMG alloys, confirming the accuracy of the measurements.

The results were further corroborated by comparing them with standard data libraries. Despite the inherent challenges in characterizing BMGs due to their complex nature, the measurements were in good agreement with the standard values, with a confidence level of 95%. This research provides a reliable method for characterizing new materials like BMGs, contributing to understanding their structure-properties relationship. The study's findings emphasize the accuracy and reliability of the Line Focus Transducers LFT2030 and LFT3560 in collecting data for new materials, demonstrating their potential for broader applications in material science.

6.0 Novel Methodology Of Coating Line Focus Transducer And Validating The System In A Corrosive Environment

This chapter introduces an innovative method of fabricating Large Lens Less Line Focus Transducers (LFTs), devices utilized in material characterization. These transducers' traditional design and size have been significantly modified, resulting in a more compact and efficient device, thereby making a profound contribution to the current body of research in this area. In the quest to enhance the functionality and versatility of LFTs, we incorporated the use of additive manufacturing technology, specifically 3D printers. The transducer casing was reconstructed using Polylactic Acid (PLA), a biodegradable thermoplastic derived from renewable resources. This change in material selection resulted in a significant reduction in the weight of the transducer.

Furthermore, the PLA proved to be more durable, even during prolonged submersion, extending the usable life of the device. Our fabrication method also aimed to enhance the utility of the transducer under harsh environmental conditions. To this end, we improved the resistance of the Polyvinylidene Fluoride (PVDF) film, a vital component of the transducer, to withstand such conditions. We achieved this by coating the film with Parylene-C, a procedure that, to our knowledge, has not been previously reported in the literature for Line Focus Transducers. Implementing these modifications in the fabrication process resulted in the successfully creating two unique Line Focus Transducers, designated LFT3560 and LFT2030. This chapter will

primarily focus on the LFT2030 due to its compact design and alignment with the purpose of our research. As a result of these advancements in fabrication, the newly designed system demonstrated enhanced material characterization capabilities. We observed a reduction in the step size required for the defocusing process, which translated into an increased accuracy in output results. Furthermore, the tested samples measured elastic constants aligned excellently with reference values in the existing literature.

6.1 Improved Line Focus Transducer For Submersion In Corrosive And High Acidity Environments

6.1.1 Transducers Improvements

In this part, the approach was changing the material components of the transducer designed and suggested by D. Xiang in 1996; since then, no improvements have been made to the transducer's casing. The transducer case is constructed using a rectangular aluminum tube that has been machined to possess the necessary curvature, as shown in Figure 6-1.

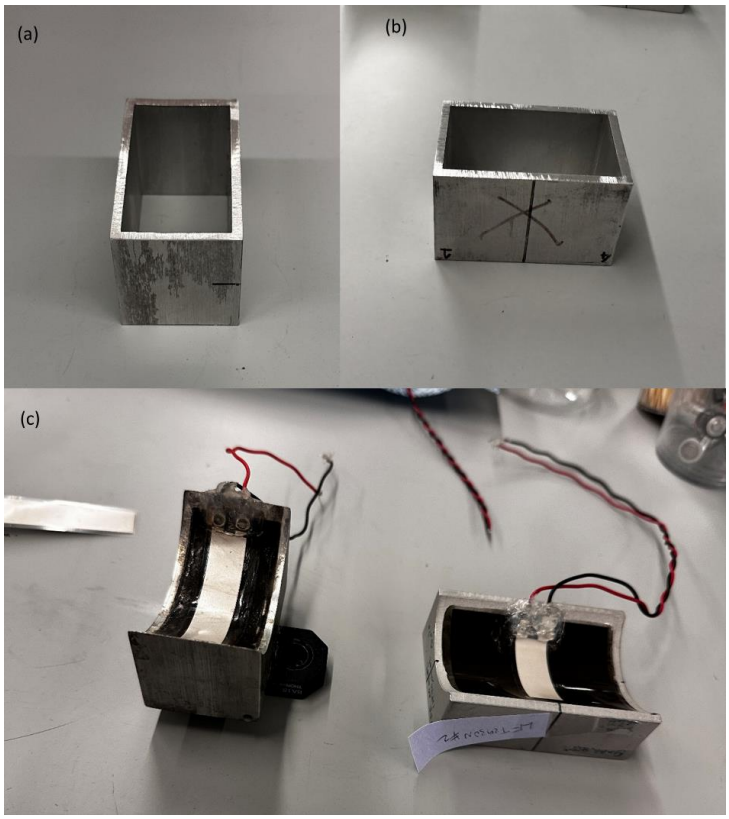

Figure 6-1:transducer case using a rectangular aluminum (a) side view, (b) Front View before machining and (c) Aluminum case after cut and backing material casted.

This part uses conventional machining to cut the aluminum tube to the desired shape. Also, the PVDF film used to generate and collect waves had never been improved to withstand harsh environments.

Our approach to improving the system consisted of two main factors the Line focus transducer should comprise. First, the Transducer should withstand harsh environments to be used in environments other than lab, such as seawater, or even in acidic environments like acid tanks. Secondly, the size of the transducer should be compact to test on smaller areas and can fit with no problem of size limitations access to that transducer in more complicated systems.

According to these two factors, a novel suggestion for building and fabricating the Line focus transducer for the first time using additive manufacturing technology where the casing was designed in solid works and then printed from a 3D printer using the PLA filament made of polylactic acid that can withstand high melting point reach up to 145-160°C and have impressive chemical resistance.

A sample made of the same material was submersed in diluted Nitric acid solution with a PH lower than one that had been left submerged for over one month with no changes happened to the structure, and no creeping or material softness was recorded during the test period as it can be seen in Figure 6-2.

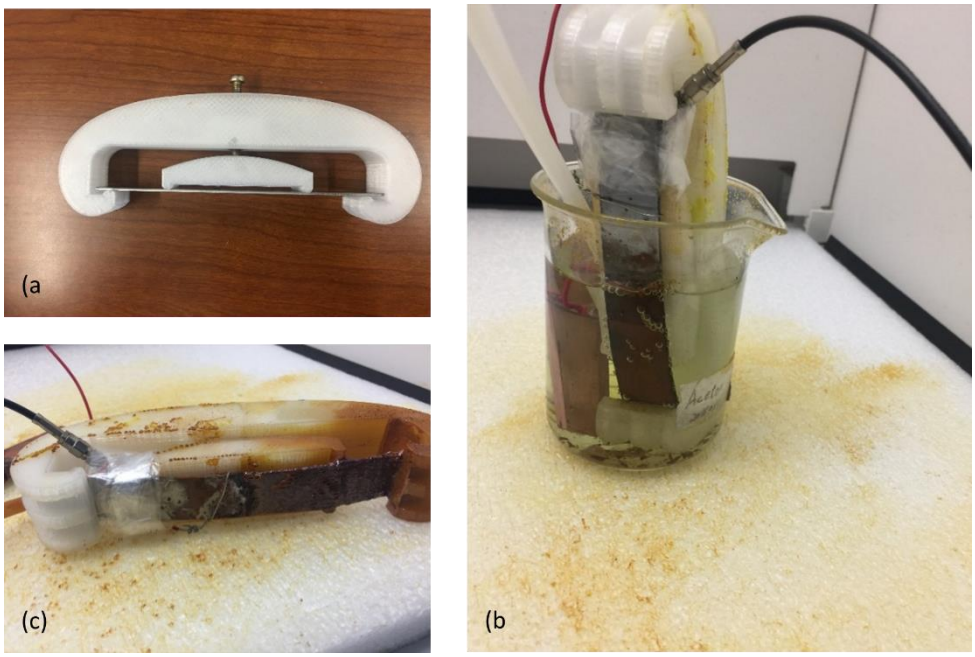

Figure 6-2 3D print sample made of PLA tested in diluted Nitric acid,(a) sample before submerse, (b) sample in diluted acidic solution left for 15 days, (c) 3D Print sample after test with no failure except some discoloration

Similarly, the flexibility that PLA material provides with 3d printing allows for building more fine meshing and sturdy samples every time a print order is given. Machining the aluminum casing requires a more professional and skillful operator to give exact results consistently. The samples made from 3D printers at the University of Pittsburgh in lab Additive Manufacturing Research Laboratory (AMRL), an institution established in 2016, and Open Lab @ Hillman Center for Teaching and Learning are shown in Figure 6-3.

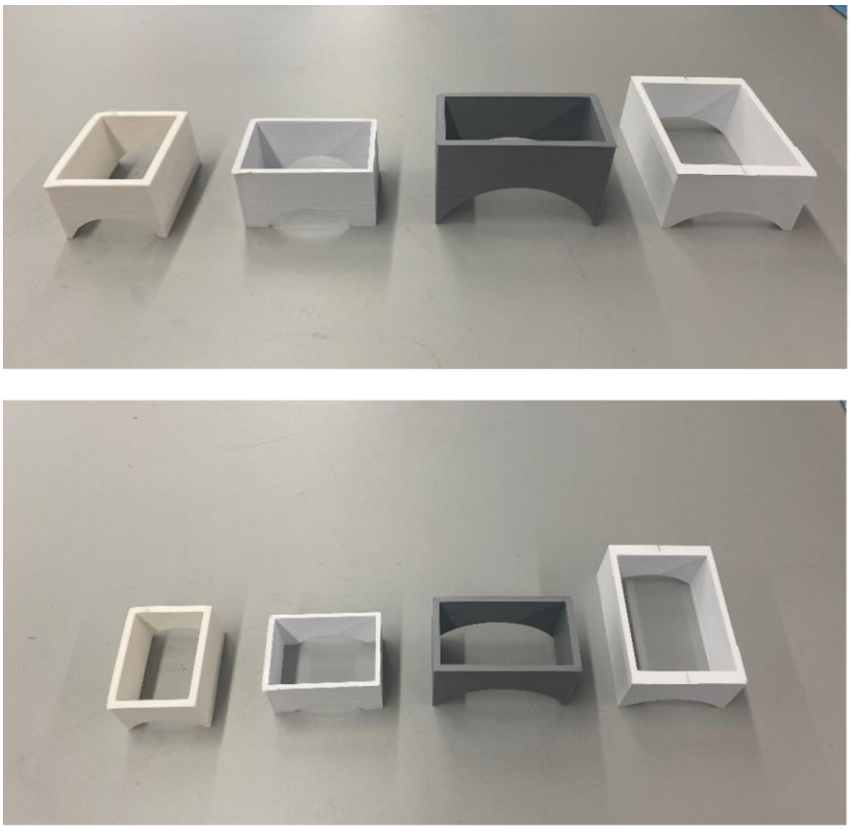

Figure 6-3 Line Focus Transducer Casing Using PLA material with different sizes, meshing, and filling levels (a) Front View, (b) Top View.

The second suggestion and improvement we had is by proofing the main component in the transducer, which is the PVDF film that will increase the abrasion & corrosion resistance by the implementation of polymeric coating using the Poly(-para-xylylene) Parylene-C (PARYLENE, By Specialty coating systems “SCS”). Parylene, a specific polymer, is characterized by a linear arrangement of benzene rings. Each ring has two methylene groups replacing two hydrogen atoms positioned on diametrically opposite sides of the benzene ring, thus serving as bonding links in the polymer's construction.

The primary source for this deposited film is a dimeric version of the perylene molecule, consisting of two parallel-coupled monomers linked via the methylene ends. In the production process, the dimer undergoes sublimation in a vaporization chamber, subsequent separation into

monomer units in a pyrolytic furnace, and deposition as extensive chain polymers onto substrates within the deposition compartment. Three keys primary of Parylene—C, N, and D—, each demonstrating unique properties, and according to our application, we used Parylene-C. The main benefit of using Parylene-C comes in many aspects, such as a low adhesion coefficient at room temperature, a high degree of protection without affecting flexibility and conformability, and low weight without compromising fragility. After curing, it is a non-porous material that provides adequate insulation against moisture for many microscale electronic devices or submerged marine devices [91-93]. Likewise, Parylene C manifests a valuable addition to its remarkably low permeability to moisture and corrosive gases, and it is a highly effective barrier layer that provides excellent moisture and chemical protection for a wide range of applications. It can encapsulate medical devices, electronics, and oxidative materials with a thin and conformal layer, ensuring waterproofing. With its superior chemical resistance, perylene can safeguard parts in harsh chemical environments. For example, the Parylene C response to 37% Hydrochloric (Non-Oxidizing Acid) HCL inorganic reagents was impressive since Parylene C showed 0.0% swelling at 25°C and 4.1% swelling at 75°C which is considered a high chemical resistant material.

Its versatility is generally demonstrated in applications such as implants, printed circuit boards, protection for various materials, 3D printed parts, power supplies, and corrosion protection for metals.

6.2 Coating Process Methodology

According to the Gorham route, the Parylene-C deposition process will be performed using a PDS coater system where the system will deposit the Parylene-C. The machine used in our case was Parylene Deposition Coater PDS 2010 in Room 620 Benedum Hall Figure 6-4.

Figure 6-4 PDS 2010 Lab Coater Parylene Deposition System

First, the dimer will be vaporized at a temperature range of 100-150°C and pressure of 1 torr to make the powder dimer go through a pyrolysis process and reduced to monomers. Secondly, the temperature will be increased to 650-700°C at a pressure of 0.5 torr, allowing for the monomers to polymerize and become gaseous monomers. After that, the gas will enter the deposition chamber at room temperature 20-25°C at 0.1torr, allowing for a conformal deposition on the substrate.

The required amount of Parylene-C to deposit a 1μm thick layer would be 1g of dimer powder and one hr. process [94]. Using this valuable feature in Parylene, a coating layer was done to the PVDF film ranging from 1-1.5 μm, as shown below in Figure 6-5.

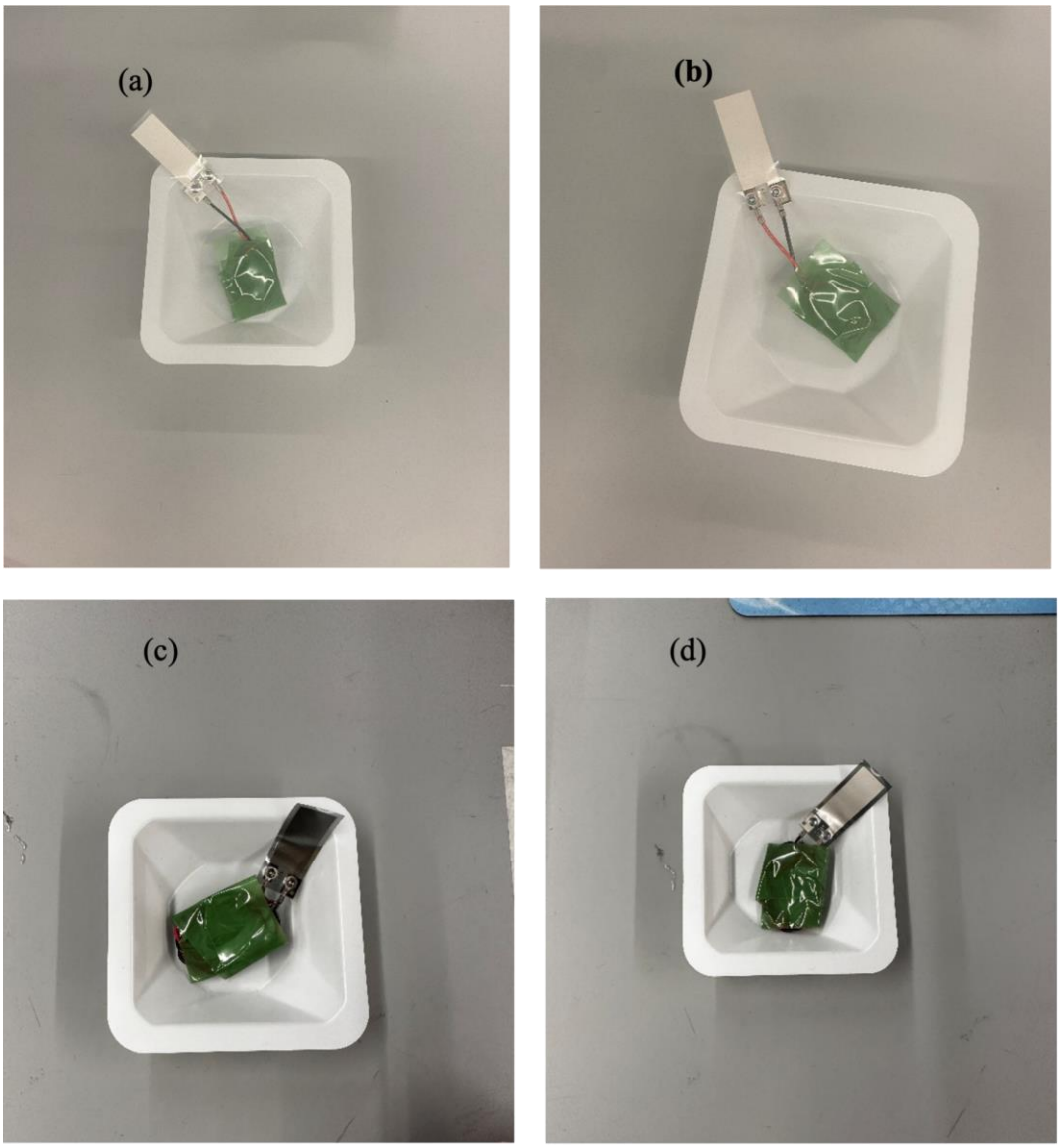

Figure 6-5 PVDF sample before Coating (a) back , (b) Front and after Coating with Paryelene-C (c) back and (d) front

A validation test was done by measuring and confirming the thickness of the coated perylene-C was done using The Filmetrics F40 Thin-Film Analyzer located at NFCF Lab at SB 60-63 Benedum Hall, as shown in Figure 6-6; the thickness sample was a Si sample placed next to the PVDF film inside the chamber of the PDS 2010 coater which coats the Si- sample with the same thickness, and it will be easier to read under the Filmetrics F40 system since the built-in library already calibrated for Si samples.

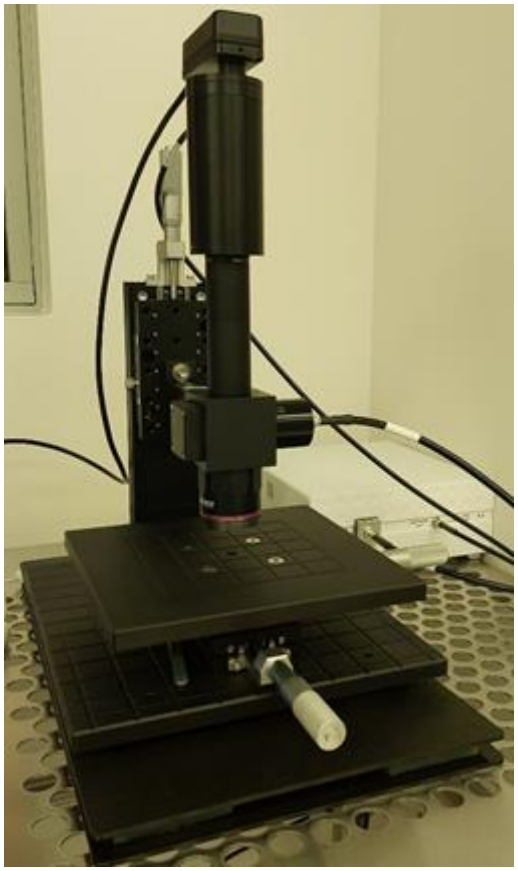

Figure 6-6 The Filmetrics F40 Thin-Film Analyzer

the result for the thin PVDF film was 11879 Å correspondents to 1.18 µm with a Goodness of fit 0.98963. in the end, the goal of this procedure is to test and prove that the new original modification we did will provide reliable data using the Ultrasonic Line focus transducer system in a corrosive environment which never have been done before due to the lack of research in this part.

6.3 Corrosive Medium (Saline Water And HCL) Preparation

The medium used to submerge the Ultrasonic LFT, and samples were made and classified under two main groups. The first one was the Saline water (salt at sea level) which we will require to bring the salinity of the freshwater to 35 ppt (parts per thousand), so a sodium chloride NaCl was used, adding 35gm of it to 965gm of distilled water. The mix was done using Fisher Scientific Hot Plate Stirrer; the stirring speed was set at 700rpm for 10min at Room Temperature to ensure the complete dissolution of NaCl with water and reach the salinity level required. After making the solution, it was used immediately in the tests, and each time we tested a new material, the solution would be replaced with a new one to avoid contamination from the previous samples.

The second was the Acidic Solution; the goal was to drop the acidity of the 1L distilled water to a pH of ≈ 1. Accordingly, the 32% by weight solution of Hydrochloric acid (HCl) with 12M was used to reach that level. and since the hydrogen ion concentration should reach 0.1M (moles per liter) for 1L total volume solution, we used 8.33ml of HCl. Again, the same procedure for the salinity water solution was done to the Acidic solution, which is changing the solution after each sample group of material to avoid contamination and acidity level change.

The acidity level was measured using Wireless Field pH Meter Electrode probe HI12302/Halo by Hann's instruments that got a reading pH range from 0 to 12 with pH accuracy (@25°C/77°F) of ±0.1 pH; ±0.01 pH; ±0.002 pH (±1 last significant digit). The Probe confirmed the reading to pH 1 for the solution made.

6.4 Materials

The test specimens employed in this study comprised three distinct categories of materials. The first group consisted of commercially available standard materials, namely Stainless Steel 420, Nickel, and Aluminum 6360, as outlined in Chapter 3. The second group encompassed the samples derived from 3D printing, specifically Sample 1 and Sample 3 (referred to as Sample 2 in this chapter for simplicity) made of stainless steel316, which were subjected to testing in Chapter 4. Lastly, the third group involved the utilization of Bulk Metallic Glass (BMG) alloys, encompassing Sample 1 (a bulk sample) comprising a Nickel-based alloy and Sample 2 (a cracked sample) composed of a Zirconium-based alloy. The testing and analysis of these BMG alloys were conducted in Chapter 5.

6.5 Measurement Methodology

The process began with carefully aligning the Line Focus Transducer (LFT) to the vertical orientation of the targeted samples. This step was crucial to ensure the accuracy of subsequent measurements, as precise alignment is pivotal for maintaining consistency in wave propagation characteristics.

Following alignment, the focus position was finely adjusted. The optimal focal position was determined by identifying the setting that yielded the highest amplitude of the directly reflected wave. This facilitated the most effective interaction between the ultrasound waves and the sample, yielding more precise measurements.

A systematic defocusing process was implemented once the optimal focus position was identified. This process involved incrementally moving the LFT closer to the specimen. The increments were carefully maintained at a constant step size of 0.2mm. This controlled approach was critical in ensuring uniformity in data collection and minimizing experimental error.

6.6 Results And Discussion

In this Part, the results shown in this chapter were generated using transducers LFT2030 & LFT3560 designed and fabricated as previously mentioned in Chapter 3. The transducer specification was 20mm and 25mm as a focal length, while the aperture half-angle was ~21 and ~25, respectively. Both Transducers were submerged under saline water and an acidic medium during the testing of each sample—the results are shown in two tables, Table 6-1 & Table 6-3.

Table 6-1 represents the data of mechanical properties of three standard commercial materials, Stainless Steel 420, Nickle, and Aluminum 6063. Also, two of the samples from 3D print additive manufacturing material used in Chapter 4 have been used in this test which is sample 1 and sample 3. and lastly, the Bulk Metallic glasses alloys used in Chapter 5 sample 1 & 2 (hence, Bulk and cracked sample, respectively) all of these samples have been submerged in saline water medium and tested using both transducers fabricated, LFT2030 and LFT3560.

In the second Table 6-3, the results of mechanical properties of the same material in Table 6-1 were tested under the harsh medium environment with an acidity level reaching PH 1 by adding and diluting HCl (32% w). In this last test, the only used Transducer was the LFT2030, Since Both transducers have been fabricated from the same casing material, backing material, PVDF film, and curing time. Also, they both had a 1-3µm thickness coat of Paralyene C, and lastly, they both proved reliable data shown already in chapters 3,5, and 6. Another factor that influenced our choice is the more compact size LFT2030 had than LFT3560, with a smaller step size. The only concern was if the Aperture angle was enough to cover the wave reflection & detection from the sample. We will prove in this literature that it was not a problem, and the system efficiently generated both Direct and Rayleigh waves enabling the rest of the measurement for the material characterization.

The significant remarks in the measured velocities in both Table 6-1 and Table 6-2 that is, on average, it is slightly faster than what has been measured in distilled water in previous chapters; the main reasoning is that the speed of sound tends to be faster in saline (sea water levels) water varies between (1450 to 1570/s) than distilled water (freshwater) (1482m/s) at 20°C. Since the speed of sound in liquids depends on two significant factors, the bulk modulus of medium and density, as it can be concluded from (6-1, where c is the speed of sound (m/s), K is the coefficient of stiffness (Pa), and ρ is density (kg/m^3). Furthermore, as it is known, K is higher in seawater

(2.34 GPa) than fresh water (2.18GPa), while density in seawater is 1022kg/m^3 while normal water is 997 kg/m^3. Also, the increase of temperature of the seawater by 1 degree will increase the speed of sound in that medium by 4.5m/s.

$$c = \sqrt{\frac{K}{\rho}} \tag{6-1}$$

So, in the measured values of Longitudinal velocity for Standard commercial materials such as SS420, Nickle, and Aluminum, its noticeable that the average Longitudinal Wave velocity was higher for Nickle and Aluminum 6306 in Saline than in distilled, which recorded 5818m/s compared to 5778m/s respectively. While for Stainless Steel, it was lower by a small margin of less than 0.54%. For the 3D print sample one, the Longitudinal average velocity jumped from 5300 to 5400 m/s and increased in average from 5333m/s to 5399.5 for 3D print sample two, and lastly, the BMG was noticeable in the increment happened in average velocity from 5900 to 5990 m/s for sample 1 (Hence, Bulk sample) as it is shown in Table 6-1.

Table 6-1 Saline water medium – sea water salinity level

Material		Slope dz/dt	Density ρ (kg/m^3)	Measured Velocities (m/s)			Elastic Constants			
				Longitudinal Wave, V_L	Rayleigh Surface Wave, V_R	Shear - Transverse Wave, V_S	Young's Modulus, E (GPa)	Shear Modulus, G (GPa)	Poisson Ratio, ν	Bulk Modulus, K (GPa)
Stainless Steel 420	LFT2030	5.3374	7820.1	5707	2913.4	3138	197.6	76.99	0.28	52
	LFT3560	5.2204		5670	2883.7	3104	193.81	75.36	0.29	51
	Standard	-	7600-7800	5720	3011	3272	197.5	78	0.27	52
Nickle	LFT2030	5.4860	7840.6	5804	2950.7	3176	203	79.10	0.29	59
	LFT3560	5.4430		5831	2939.9	3162	202.5	78.38	0.29	62
	Standard	-	8830-8950	5630	-	2815	205	77	0.31	62
Aluminum 6063	LFT2030	5.6832	2689.0	6213	2999.5	3213	73	27.75	0.32	67
	LFT3560	5.3559		7027	2918.0	3096	71	25.77	0.37	98
	Standard	-	2700	6320		3160	68.9	25.8	0.33	70
3D Print Sample 1	LFT2030	4.1145	8003.4	5369	2586.7	2770	161.95	61.41	0.32	149
	LFT3560	3.9175		5431	2530.3	2703	156.12	58.45	0.34	158
	Standard	-			-		172	70	0.29	143
3D Print Sample 2	LFT2030	4.6955	8112.2	5424	746.6	2955	182.64	70.85	0.29	144
	LFT3560	4.4658		5375	2684.5	2884	175.17	67.48	0.30	144
	Standard	-			-		172	70	0.29	143
BMG Sample 1 Bulk	LFT2030	4.4134	7919.3	5875	2670.1	2847	172.86	64.19	0.35	188
	LFT3560	4.4560		6105	2681.8	2854	175.44	64.49	0.36	209
	Standard	-			-		172	66.3	0.371	196.8
BMG Sample 2 Cracked	LFT2030	3.9969	4431.0	5714	2553.2	2719	88.71	32.77	0.35	101
	LFT3560	3.9284		5300	2533.5	2711	86.17	32.57	0.32	81
	Standard	-			-		87.3	32.05	0.365	97.5

On the other hand, the elastic properties for the standard commercial materials, 3D print samples 1 & 2 and Bulk metallic Glasses Ni- Zr- based alloy are fulfilling the standard values in saline water as shown in Table 6-1. Also, as shown from the figures of Young's modulus, Shear Modulus, and Poisson's Ratio for 3D prints samples 1&2 and BMG alloys, the distribution is closely related with minimal discrepancy. The error margin was calculated and will be shown in the next section.

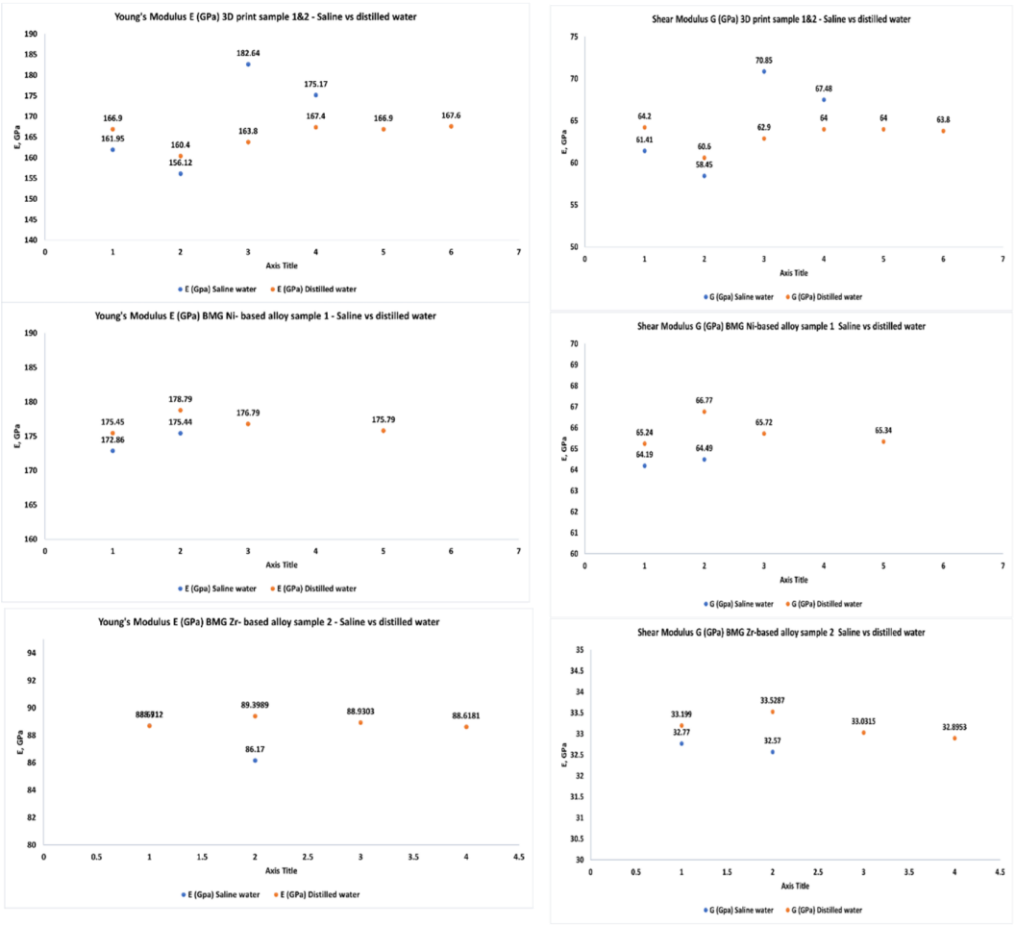

Figure 6-7 Young's modulus E(GPa) Left side and Shear Modulus Right side for 3Dprint then BMG Ni-Based then BMG Zr-based

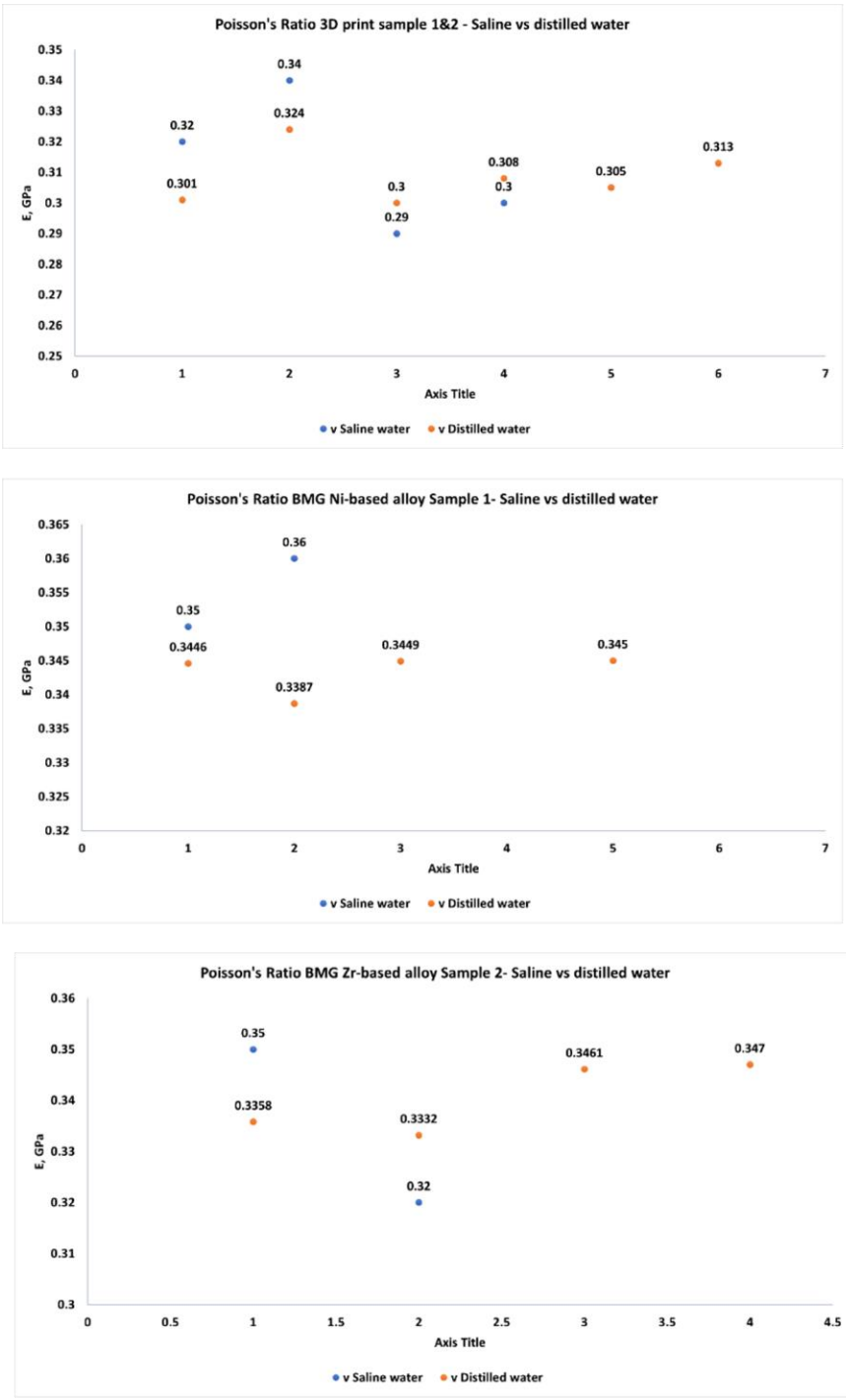

Figure 6-8 Poisson's Ratio for 3Dprint then BMG Ni-Based then BMG Zr-based.

Next, by Measuring the deviation from standard elastic constants for each sample considering the error factor, we ended up with an overall acceptable value that would not exceed the 10-15% error range limit for each sample, as shown in Table 6-2.

Table 6-2: Elastic constants' Error percentage in saline water (sea water level 35ppt) for SS420, Nickle, Al6306 commercial material, 3D print samples (1 & 2) and Bulk metallic Glasses alloys samples (1 and 2)

		Young's Modulus, E (GPa)	Shear Modulus, G (GPa)	Poisson Ratio, ν	Bulk Modulus, K (GPa)
Stainless Steel 316	LFT2030	0.05%	-1.29%	3.70%	0.00%
	LFT3560	-1.87%	-3.38%	7.41%	-0.66%
Nickle	LFT2030	-0.98%	2.73%	-6.45%	-1.85%
	LFT3560	-1.22%	1.79%	-6.45%	0.00%
Aluminum	LFT2030	5.80%	8.82%	-3.03%	-4.29%
	LFT3560	2.90%	1.06%	12.12%	40.00%
3D Print	LFT2030	-5.84%	-12.27%	10.34%	4.20%
Sample 1	LFT3560	-9.23%	-16.50%	17.24%	10.49%
3D Print	LFT2030	6.19%	1.21%	0.00%	0.70%
Sample 2	LFT3560	1.84%	-3.60%	3.45%	0.70%
BMG	LFT20 30	0.50%	-3.18%	-5.66%	-4.47%
Sample 1	LFT3560	2.00%	-2.73%	-2.96%	6.20%
BMG	LFT2030	1.62%	2.25%	-4.11%	3.59%
Sample 2	LFT3560	-1.29%	1.62%	-12.33%	-16.92%

According to the results from Table 6-2, The highest error was for the 3D print SS316 sample no.1, which had 9.23%, the highest we recorded. Even with the errors measured for Shear modulus and Poisson ratios, the results were mainly acceptable except for the 3D print sample 1, which again recorded higher errors around 16.5% and 17.24%, respectively, although 3D print sample 2 had consistent and lower error margins. However, we suspect that 3D print sample 1 had misalignment, which might cause changes in results due to the diagonal

cut in 3D print samples, which affected Transducer's ability to detect perfect signals. Moreover, lastly, the Bulk metallic glasses had meager error margins below 12% for both samples except the Bulk modulus error for sample 2 since it recorded almost 17%.

One more note that we had an outlier error represented in the Aluminum Bulk modulus value, which recorded an error of 40% using the Line focus Transducer LFT3560, although all the other values like Young's modulus shear modulus and Poisson ratio were within the acceptable range. The only reasoning could lead to that result is the longitudinal velocity recorded by the LFT3560, which was 7027m/s higher than standard values for Aliminum6030 (6320m/s), which in turn increased the Bulk modulus value after substituting that value in bulk modulus (6-2.

$$K = \rho\left(V_L^2 - \frac{4}{3}V_S^2\right) \tag{6-2}$$

After these tests and results, we can conclude that testing the metal alloys in saline water utilizing the Line focus transducer system can produce reliable and acceptable repeatability data set to calculate the elastic constants and define the material properties.

The more difficult experiment would be the submersion of the Line focus Transducer in an acidic medium such as the one we made, as we mentioned previously. Initially, the system could not detect the signal, but after an alignment to the base of the container holding the sample, we had the signal, and we recorded the following data, as shown in Table 6-3.

In this test, we used only LFT2030, as we previously mentioned the reasoning behind that choice. In addition, we chose three standard commercial materials, and they are (SS420, Ni, and Al6306). Also, we tested the 3D print sample from additive manufacturing since we had a reliable result in Chapter 4. Lastly, we tested the BMG alloys in samples 1 (Ni-based alloy) and 2 (Zr-based alloy).

Table 6-3 Acidic medium – HCL PH=1 using Line Focus Transducer LFT2030

Material		Slope dz/dt	Density ρ (kg/m^3)	Measured Velocities (m/s)			Elastic Constants			
				Longitudinal Wave, V_L	Rayleigh Surface Wave, V_R	Shear Transverse Wave, V_S	Young's Modulus, E (GPa)	Shear Modulus, G (GPa)	Poisson Ratio, ν	Bulk Modulus, K (GPa)
Stainless Steel 316	measured	5.68	7820	5757	3000	3240	208	82.07	0.2683	150
	Standard	-	8000	5720	3011	3272	197.5	78	0.27	152
Nickle	Measured	5.23	7841	5885	2885	3096	197	75.17	0.3086	171
	Standard		8830	5630	-	2815	205	77	0.31	162
Aluminum	Measured	5.35	2689	6183	2917	3118	69.51	26.14	0.3295	67.93
	Standard		2700	6320	-	3160	68.9	25.8	0.33	70
3D Print Sample 1	Measured	4.23	8003	5418	2619	2806	166	63.01	0.3168	151
	Standard	-	-	-	-	-	172	70	0.29	143
3D Print Sample 2	Measured	4.23	8112	5412	2622	2809	168	64.01	0.3156	152
	Standard	-	-	-	-	-	172	70	0.29	143
BMG Sample 1	LFT2030	4.40	7919	5880	2669	2846	173	64.12	0.3471	188
	Standard	-	-	-	-	-	172	66.3	0.371	196.8
BMG Sample 2	LFT2030	4.01	4431	5871	2559	2722	89	32.82	0.3631	109
	Standard	-	-	-	-	-	87.3	32.05	0.365	97.5

The results for each sample are given in Table 6-3; measured Elastic constants for standard commercial samples (SS420, Ni, and AL6306) have a close-range value with an error margin that will not exceed 10%, as shown in Table 6-4.

Table 6-4 Elastic Constants' error margin calculated for Standard Commercial Materials (SS420, Ni, and Al6306)

Material	Young's Modulus, E (GPa)	Shear Modulus, G (GPa)	Poisson Ratio, ν	Bulk Modulus, K (GPa)
SS 316	5.32%	5.22%	-0.63%	-1.32%
Nickle	-3.90%	-2.38%	-0.45%	5.56%
AL3606	0.89%	1.32%	-0.15%	-2.96%

As for the 3D print samples 1 and 2, we noticed that the measured Young's modulus was 166 and 168 GPa, respectively, with an error margin not exceeding 3.5% from standard material. More consistent results than the one measured in saline water since it was in the later 162 and 183 GPa, although both measurements were based on the wave data collection by LFT2030 in both tests. That might be related to the base leveling adjustment we mentioned earlier. The same can be seen in shear modulus, Poisson ratio, and Bulk modulus, where it noticed that results confirm each other with a slight margin of difference for samples 1 and 2 in acidic solution; the shear modulus was 63 and 64 GPa, the Poisson ratio values of 0.32 for both samples and the Bulk modulus measured at 151 and 152 GPa for sample 1 & 2 respectively with an acceptable error margin 6% to standard commercial material that is 143 GPa.

Table 6-5 Elastic Constants' error margin calculated for 3D print samples 1 & 2

Material	Young's Modulus, E (GPa)	Shear Modulus, G (GPa)	Poisson Ratio, ν	Bulk Modulus, K (GPa)
3D Print #1	-3.49%	-9.99%	9.24%	5.59%
3DPrint #2	-2.33%	-8.56%	8.83%	6.29%

Lastly, the test included the Bulk metallic glasses samples in Chapter 5. The BMG alloys, especially the Zr- and Ni-based alloys, are well known for their outstanding corrosion resistance, which helps in having more stable material in a corrosive environment helping us to determine if the new method of coating the Line focus transducers is effective. Accordingly, the test is done for samples 1 and 2 with no change in any of the experiment factors already done in the Saline water test, with encouraging results as seen in Table 6-3.

Table 6-6 Elastic Constants' error margin was calculated for BMG sample 1(Ni-) and 2(Zr-) based alloys.

Material	Young's Modulus, E (GPa)	Shear Modulus, G (GPa)	Poisson Ratio, ν	Bulk Modulus, K (GPa)
BMG Sample1 Ni-based	0.58%	-3.29%	-6.44%	-4.47%
BMG Sample2 Zr- based	1.95%	2.40%	-0.52%	11.79%

The Young's modulus for sample 1 was measured at 173 GPa, while the standard BMG Ni-based alloy had an average Young's modulus of 172 GPa, with an error of 0.58%. The shear modulus measured at 64 GPa while the standard was 66 GPa, still with a very acceptable error margin of 3.3%, while the Poisson ratio was 0.29 and the standard value is 0.34 with an error margin of 6%, which would be the highest error we recorded for this sample, and lastly the Bulk modulus for the sample measured at 188 GPa while the standard is 196GPa still with an acceptable error margin of 4.47%. These results show that LFT2030 can detect accurate wave velocities, primarily when the material under the test is known for corrosive resistance, such as Ni-based BMG alloy.

As for sample 2 (Zr- based alloy), this sample, as mentioned before, had a crack on the back wall surface that sometimes gave us different results due to the direct wave propagation through the sample thickness, but using the smaller and more compact size LFT2030, we overcome that problem since the later transducer needs only smaller area to focus and defocus which enabled us to avoid the crack area and measured the wave velocity more accurately.

The measurements for sample 2 (Zr- based alloy) resulted in having Young's modulus measured at 89 GPa with a 1.95% error margin from standard material. The shear modulus and Poisson ratio results were 32.8 GPa and 0.3631, respectively. These results were almost identical to the standard values of 32.05 GPa and 0.365 for the Shear modulus and Poisson ratio. While the bulk modulus K measured at 109 GPa higher than standard value that is 97.5 GPa by 11.79%, the reasoning for this higher error margin could be related to the difficulty in defining the back wall reflected wave D_L adding that to the increase of wave velocity in acidic environment since the temperature of liquid medium holding the sample were higher than distilled by few degrees between 3-4 C degrees. which might alter the result in having larger

Longitudinal velocity affecting the Bulk modulus calculations. Nevertheless, since this error margin did not exceed 10% for the other elastic constants, we can conclude that overall results can be acceptable.

At last, the following samples of Figure 6-9, Figure 6-10 and Figure 6-11 showing all the results of main Elastic Constants such as Young's Modulus, Shear Modulus, and Poisson's ratio for the three mediums (Distilled water, Saline water, and Acidic medium) for group 2 and 3 (3D prints and BMG) proving the high adjacency results we got for this experiment since the results tend to converge near to each other which validate the use of LFT2030 Line focus Transducer as reliable, compact Ultrasonic system for material characterization.

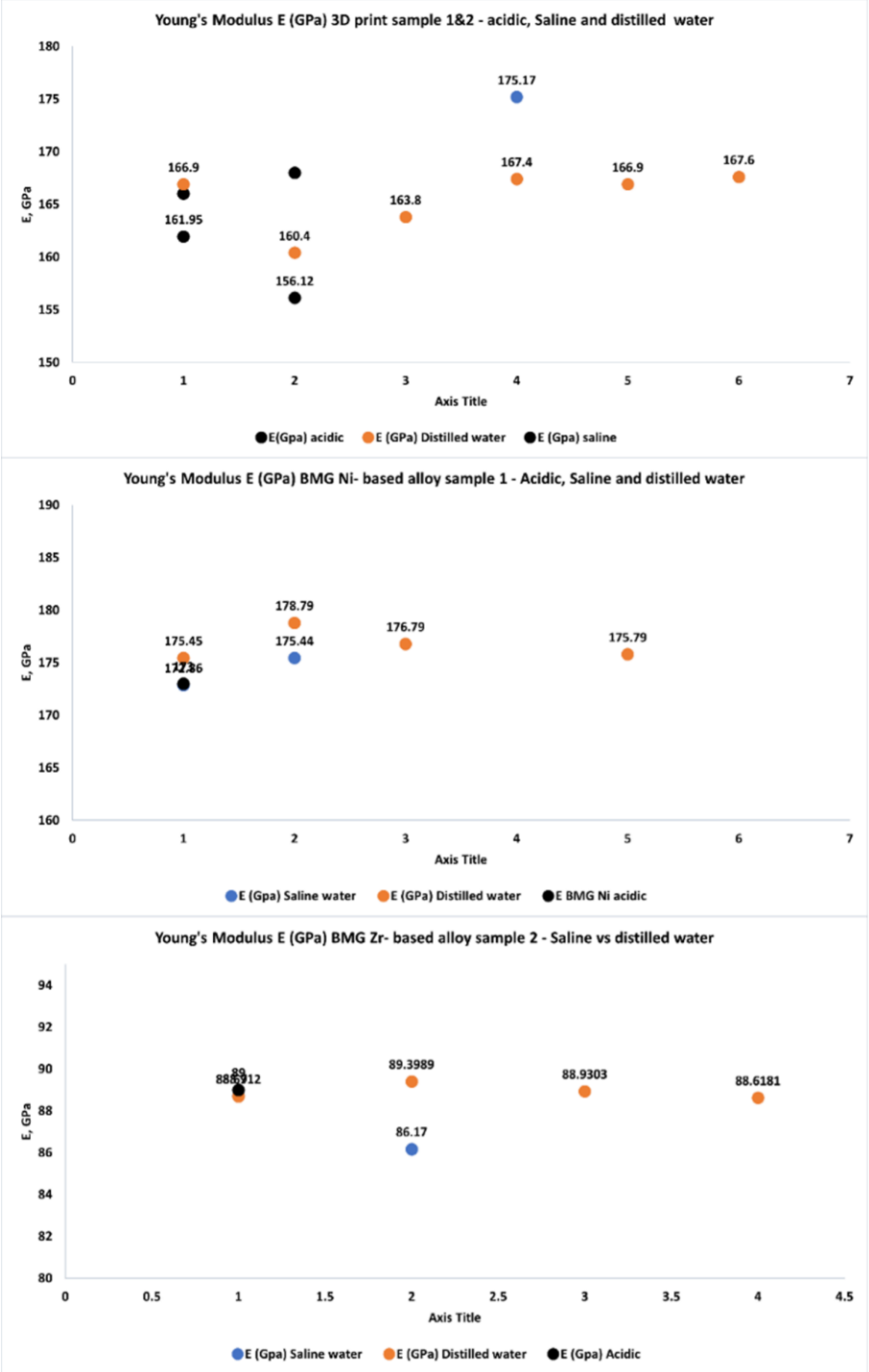

Figure 6-9 E(GPa) Young's Modulus for (a) 3D Print sample 1 and 2, (b) BMG Ni- based sample 1, (c) BMG Zr-based sample 2 in- acid, saline and distilled water

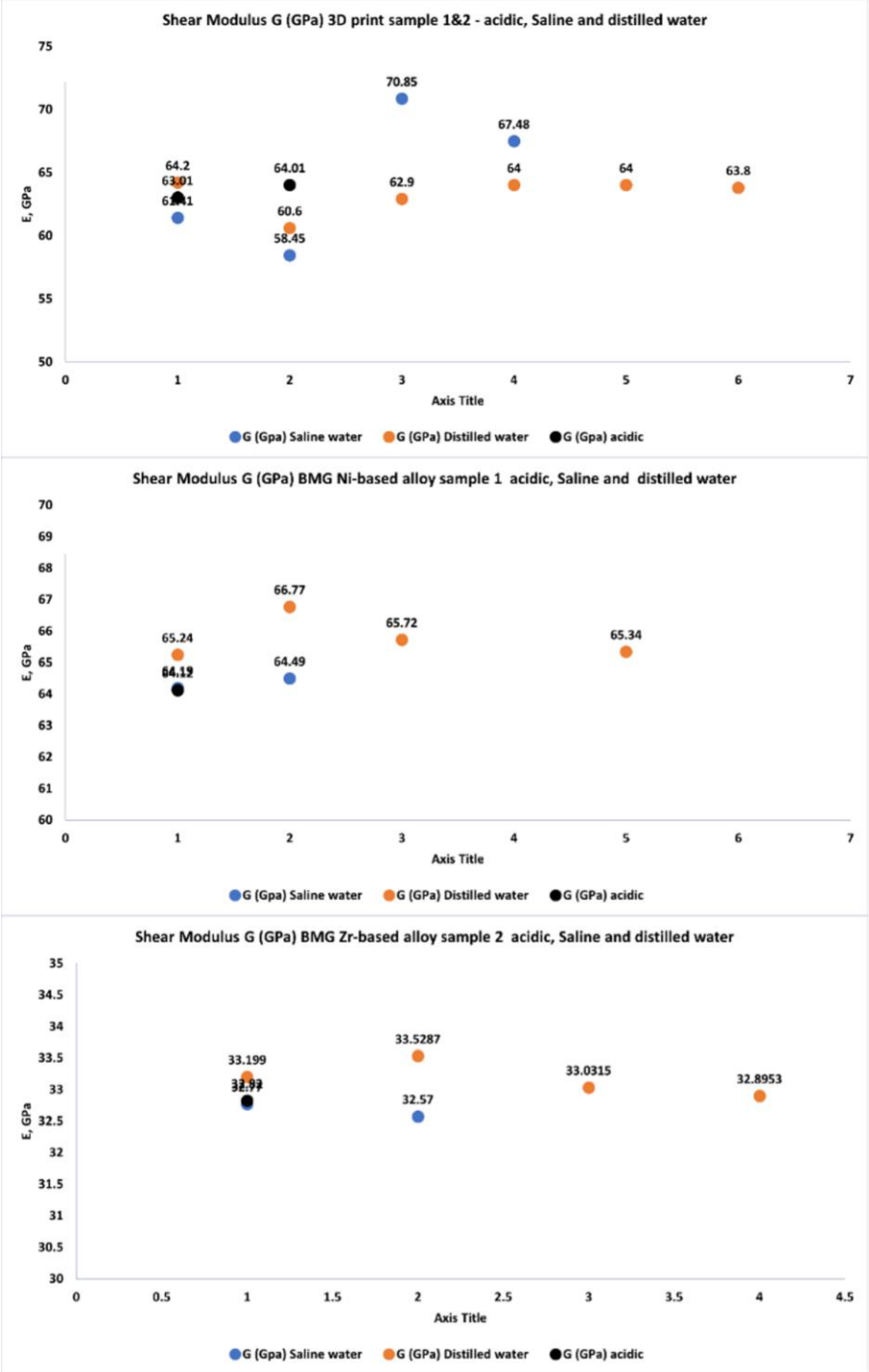

Figure 6-10 G(GPa) Shear Modulus for (a) 3D Print sample 1 and 2, (b) BMG Ni- based sample 1, (c) BMG Zr-based sample 2 in- acid, saline and distilled water

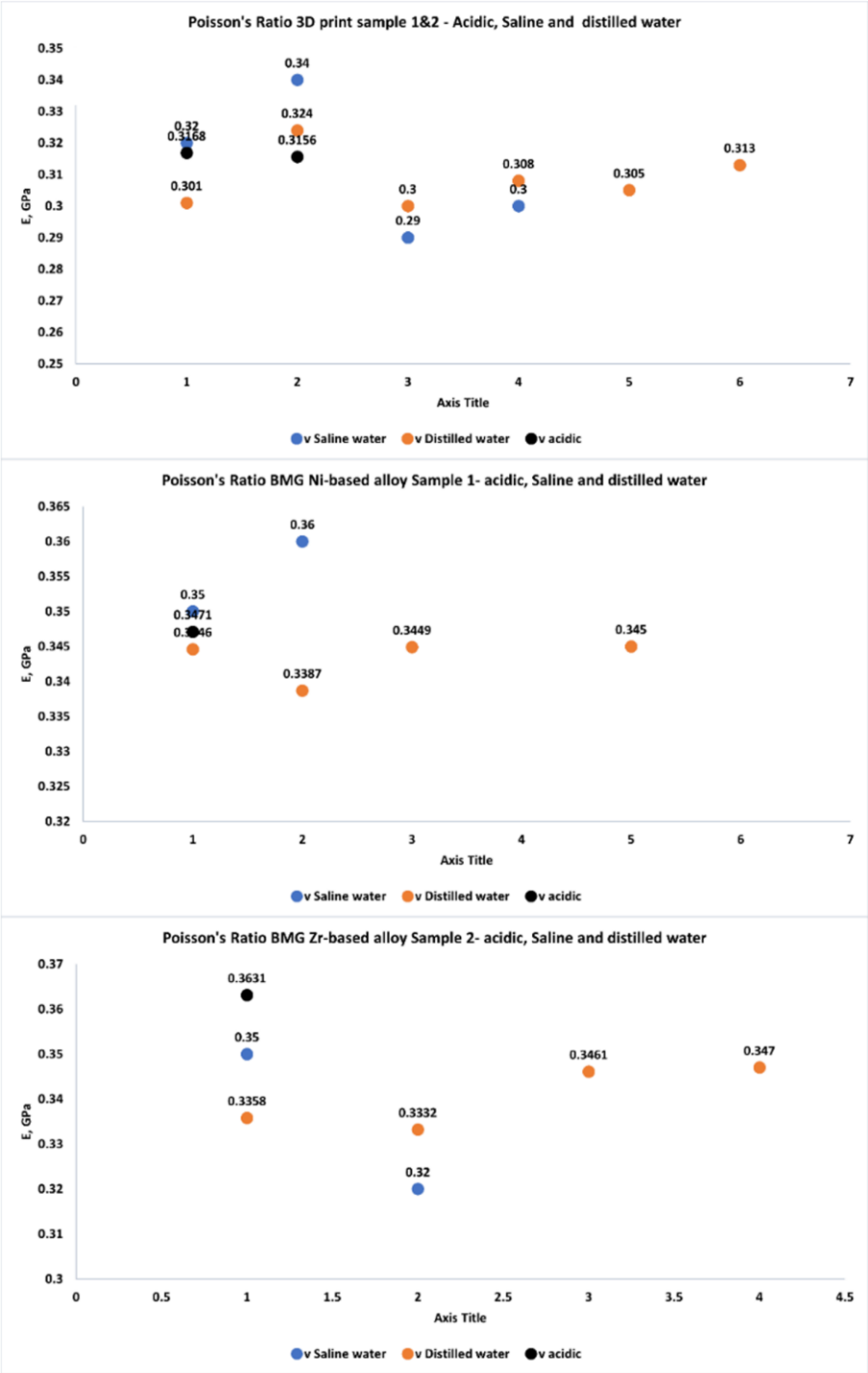

Figure 6-11 v Poisson's Ratio for (a) 3D Print sample 1 and 2, (b) BMG Ni- based sample 1, (c) BMG Zr-based sample 2 in- acid, saline and distilled water

7.0 Conclusion Remarks and Future Work

This Thesis has made significant strides in non-destructive testing (NDT) and non-destructive evaluation (NDE) techniques, specifically focusing on ultrasound testing. It presents the work and improvement of a novel method to develop a Lens less line-focus PVDF piezoelectric transducer capable of collecting and reading longitudinal and Rayleigh surface waves under a corrosive environment. The protection of the transducer from acidity or any harsh chemicals, including the changes to the main casing of the transducer and the PVDF film coating process, was studied and validated through experimental studies.

First, the lens-less line focus transducer, a product of the innovative work of D. Xiang and Yamanaka, has been a central focus of this research. Its versatility, efficiency, and affordability have been highlighted, and its potential in the characterization of isotropic materials has been thoroughly explored by designing different sizes and testing them on standard materials. This exploration has contributed significantly to the broader field of understanding the best focal length and aperture angle of Line Focus Transducer -experimentally- suited to material characterization.

Second, A crucial part of the study came after, which was the application of the lens-less line focus transducer in testing 3D printed materials. Three primary samples were tested extensively by taking three readings for each sample, analyzing them, and then comparing them to each other to find any discrepancies or deviations in order to demonstrate the effectiveness of the transducer in characterizing these samples, providing valuable data on their elastic constants such as Young's modulus and Rayleigh surface waves velocity and validating the accuracy of the Transducers to regenerate consistent results.

Furthermore, the study examined the application of Line Focus Transducers on novel Bulk Metallic Glasses (BMGs). The aim was to categorize the material and verify the design's consistency and reliability in producing repeatable results. The results confirmed the effectiveness of the transducer in identifying and characterizing the BMGs, which led to building a statistical predict range for Elastic modulus, shear modulus, Poisson's ratio & bulk modulus with t-scores of 95% confidence interval, thereby validating its use in this context.

In the final chapter of the thesis, a proposed novel methodology for coating Line focus Transducers, enabling their use in corrosive environments. It has been validated through experimental testing comparing three groups of previously tested materials submerged in distilled water, but this time tested in two new mediums, such as seawater and diluted acid solution, including HCl. The first group was the standard materials; the second group was the 3D printed samples from Chapter 4; the last third group was the BMG samples tested and verified from Chapter 6. The findings showed that the results were very close to the standard, with minimal deviations. This confirms the accuracy of the testing methods used and demonstrates the reliability of the new coated lens-less line focus transducer in producing consistent and accurate results, further expanding the potential applications of these transducers. The proposed coating methodology has the potential to revolutionize the use of these transducers in harsh environments, opening new avenues for their application.

In conclusion, this research has substantially contributed to non-destructive testing and evaluation. It has advanced our understanding of the techniques and methodologies involved and opened new avenues for future research and practical applications. The potential of these techniques to revolutionize various industries is significant, and future work should continue to explore and refine these techniques for broader application.

Appendix A MATLAB Program

1. Program Code to calculate Longitudinal Wave propagation in the target sample.

```
clear;clc
%%The first part is to determine the intrinsic property of the material
M=33.7468;%mass in g
V=12.55;%volume in ml
density=M/V*1000 %density in kg/m3
%The thinckness is used for calculate longitudinal bulk wave
d=6.43; %thickness in mm
Defocus_Time=xlsread('Linear_Interpolation_AL');
figure(1);
scatter(Defocus_Time(:,3),Defocus_Time(:,2),'b','*');
hold on
plot(Defocus_Time(:,3),Defocus_Time(:,2));
title('Z(t) Plot AL');
xlabel('Delay Time (ns)');
ylabel('Defocal Position Z(mm)');
P = polyfit(Defocus_Time(:,3),Defocus_Time(:,2),1);
slope=P(1)*10^6

%%import the data of focus point
Focus=csvread('focus01.csv',2,0);
%%Plot the diagram of the focus point
figure(2);
plot(Focus(:,1),Focus(:,2));
title('Curves of Rayleigh Wave Propagation AL');
xlabel('Time (ns)');
ylabel('Voltage+Offset');
hold on
%Find the highst reflection (Longitudinal Wave)
[value,position]=max(Focus(:,2))
x_value=Focus(:,1);
Highest_time=x_value(position,1)
%Find the longitudinal bulk wave reflection
%The Time Delay was calculated from the values of the focus point
%The time delay is the time between the highest point of the first
%reflection wave and the longitudinal bulk wave
    Back_Reflect_x=Focus(:,1);
    Back_Reflect_y=Focus(:,2);
    Find_Back=[0,0];
    for j=1:length(Back_Reflect_x(:,1))
        if Back_Reflect_x(j)>4.96242e-5 && Back_Reflect_x(j)<4.97142e-5
            Find_Back=[Find_Back;Back_Reflect_x(j),Back_Reflect_y(j)];
        end
    end
    [Bulk_Value,Bulk_Position]=max(Find_Back(:,2))
    Bulk_Time=Find_Back(Bulk_Position,1)
    TimeDelay_BulkWave=Bulk_Time-Highest_time
```

```
        V_L=2*d/1000/TimeDelay_BulkWave

    %Find the highst reflection (Longitudinal Wave) in the focus to allignt
the
    %data
    % [value,position]=max(Focus(:,2))
    % x_value=Focus(:,1);
    % Highest_time=x_value(position,1)

        for i=1:10
        j=num2str(i);
        alal=['adjust0',j];
        alalal=[alal,'.csv'];
        Data=csvread(alalal,2,0);%Import each data set from 1-10
        clear alal alalal;
        %set the offset of y (with increment of 0.1)
        a=Data(:,2);
        b=length(a);
        offset=0.25*i*ones(b,1);
        Data(:,2)=Data(:,2)+offset;
        %Align the highest point (find the offset of x-axes)
        [value1,position1]=max(Data(:,2));
        x_value1=Data(:,1);
        offset_x=Highest_time-x_value1(position1,1);
        offset_x=offset_x*ones(b,1);
        Data(:,1)=Data(:,1)+offset_x;
        plot(Data(:,1),Data(:,2));
        end

    for i=1:9
        k=num2str(i);
        filename=['step0',k];
        filename1=[filename,'.csv'];
        Data=csvread(filename1,2,0);%Import each data set from 1-10
        %set the offset of y (with increment of 0.1)
        a=Data(:,2);
        b=length(a);
        offset=0.25*(i+10)*ones(b,1);
        Data(:,2)=Data(:,2)+offset;
        %Align the highest point (find the offset of x-axes)
        [value1,position1]=max(Data(:,2));
        x_value1=Data(:,1);
        offset_x=Highest_time-x_value1(position1,1);
        offset_x=offset_x*ones(b,1);
        Data(:,1)=Data(:,1)+offset_x;
        plot(Data(:,1),Data(:,2));
    end
```

2. Calculation of Rayleigh Surface wave Velocity, Shear Wave velocity and Elastic Constants including Young's modulus, Shear modulus, Poisson's ratio and Bulk modulus for target sample

```
%slope=z/dt;
%This is what we can get from the experiment
%Surface Wave
V_W=1480;
%Rayleigh surface wave velocity
V_R=(1/(V_W*slope)-1/4/(slope^2))^(-0.5);
%longitudinal bulk wave velocity,get from the experiment as well
V_L;
syms V_T;
tho=density;
[V_T]=solve((V_T/V_L)^3-(V_R/V_L)*((V_T/V_L)^2)-
0.718*(V_T/V_L)+0.75*(V_R/V_L)==0);
V_T=double(V_T);
V_T=abs(V_T);
L=length(V_T);
for i=1:L
    if V_T(i)< (V_L/(2^0.5))
        answer=V_T(i);
    end
end
V_T=answer;
C_L=V_L
C_R=V_R
C_S=V_T
%density unit is kg/m^3
%Elastic Constants calcualtions
E=(tho*(V_T)^2*(3*(V_L^2)-4*(V_T^2))/(V_L^2-V_T^2))/(10^9)%The   Young's
Modulus
G=(tho*V_T^2)/(10^9)%The Shear modulus
v=(2*V_T^2-V_L^2)/(2*(V_T^2-V_L^2))%Poisson's ratio
K=  ((tho*(V_L^2-2*V_T^2))+((2/3)*(tho*V_T^2)))/(10^9)%Bulk  Modulus  of
the solid
```

Appendix B Density Calculation For Bulk Metallic Glasses Samples (1 & 2)

The Density Calculation Of A Zr-Cu-Ni-Ti Alloy

This report outlines the procedure and calculations carried out to determine the density of a bulk metallic alloy composed of Zr, Cu, Ni, and Ti. The composition of the alloy, by atomic percentage, is $Zr_{67.09}Cu_{12.38}Ni_{9.23}Ti_{11.3}$. The alloy has a total mass of 92.4928 grams and occupies a volume of 20,874 mm^3.

Methodology

1. Calculation of the Mass of Each Component:

The mass of each component in the alloy is calculated by multiplying the atomic percentage by the total mass of the alloy.

2. Calculation of the Number of Moles for Each Component:

The atomic weights of Zr, Cu, Ni, and Ti are approximately 91.22 g/mol, 63.55 g/mol, 58.69 g/mol, and 47.87 g/mol, respectively. The number of moles of each component is calculated by dividing the mass by the atomic weight.

3. Calculation of Density:

The density of the alloy is calculated using the formula: Density (ρ) = Total Mass (m) / Volume (V).

Results

Mass of Each Component

- Mass of Zr = 67.09% of 92.4928 grams = 0.6709 * 92.4928 grams ≈ 62.06 grams

- Mass of Cu = 12.38% of 92.4928 grams = 0.1238 * 92.4928 grams ≈ 11.44 grams

- Mass of Ni = 9.23% of 92.4928 grams = 0.0923 * 92.4928 grams ≈ 8.53 grams

- Mass of Ti = 11.3% of 92.4928 grams = 0.1130 * 92.4928 grams ≈ 10.45 grams

Number of Moles of Each Component

- Moles of Zr = Mass of Zr / Atomic weight of Zr = 62.06 grams / 91.22 g/mol ≈ 0.680 moles

- Moles of Cu = Mass of Cu / Atomic weight of Cu = 11.44 grams / 63.55 g/mol ≈ 0.180 moles

- Moles of Ni = Mass of Ni / Atomic weight of Ni = 8.53 grams / 58.69 g/mol ≈ 0.145 moles

- Moles of Ti = Mass of Ti / Atomic weight of Ti = 10.45 grams / 47.87 g/mol ≈ 0.218 moles

Density of the Alloy

The volume of the alloy is 20,874 mm^3, which is equivalent to 20.874 cm^3 (1 cm^3 = 1,000 mm^3).

Using the formula for density:

ρ = Total Mass / Volume

= 92.4928 grams / 20.874 cm^3

≈ 4.43 grams/cm^3

Conclusion

The density of the Zr67.09Cu12.38Ni9.23Ti11.3 alloy, with a total mass of 92.4928 grams and a volume of 20,874 mm^3, is approximately 4.43 grams per cubic centimeter.

The Density Calculation Report Of Hexagonal Zr-Cu-Ni-Ti Alloy Sample

This report outlines the procedure and results for calculating the density of a bulk metallic alloy with composition Zr67.09Cu12.38Ni9.23Ti11.3. The sample is shaped as a hexagonal prism with a specific edge length and thickness. The total mass of the alloy sample is provided, and the density is computed accordingly.

Data given:

- Alloy Composition: Zr67.09Cu12.38Ni9.23Ti11.3
- Shape: Hexagonal Prism
- Edge Length: 32.73 mm
- Thickness (Height) of the Prism: 7.5 mm
- Total Mass of the alloy sample: 92.4928 grams

Methodology

The density (ρ) is calculated using the formula:

ρ = Total Mass (m) / Volume (V).

The volume (V) of the hexagonal prism is computed using the formula:

$V = (3\sqrt{3}/2) * \text{Edge Length}^2 * \text{Height}$.

Calculations

1. Calculating the volume of the hexagonal prism:
   - $V = (3\sqrt{3}/2) * (32.73\ mm)^2 * 7.5\ mm$
   - $\approx 20{,}873.975068749\ mm^3$.

   Convert the volume to cubic centimeters:
   - Volume (V) = $20{,}873.975068749\ mm^3$ / 1,000
   - $\approx 20.874\ cm^3$.

2. Calculating the density of the hexagonal prism:
   - ρ = Total Mass / Volume

- = 92.4928 grams / 20.874 cm^3

- ≈ 4.43 grams/cm^3.

Conclusion

The density of the bulk metallic alloy sample with the composition $Zr_{67.09}Cu_{12.38}Ni_{9.23}Ti_{11.3}$, shaped as a hexagonal prism with an edge length of 32.73 mm and a thickness of 7.5 mm, is calculated to be approximately 4.43 grams per cubic centimeter (g/cm^3).

Appendix C Saline And Acid Solution Calculation And Preparation Methodology

Laboratory Preparation Of A Saline Solution Emulating Sea-Level Salinity

I. Introduction:

Salinity is a fundamental characteristic of seawater, affecting its physical and chemical properties. On average, seawater at sea level possesses a salinity of about 3.5% or 35 parts per thousand (ppt). This implies that in every kilogram of seawater, there are approximately 35 grams of dissolved salts, predominantly sodium chloride. This report presents a method to simulate seawater's salinity using sodium chloride and fresh water, acknowledging that actual seawater contains a variety of additional salts and minerals.

II. Materials and Methods:

Materials:

1. Sodium chloride (table salt)
2. Distilled or deionized water
3. Gram-accurate scale
4. 1-liter beaker or equivalent container
5. Stirring apparatus

Procedure:

1. Using the scale, measure out exactly 35 grams of sodium chloride.
2. Dispense 965 grams (or approximately 965 milliliters, considering the density of water is about 1 gram per milliliter) of distilled or deionized water into the beaker.
3. Gradually add the 35 grams of sodium chloride into the beaker containing the water.

4. Stir the mixture thoroughly until all the salt is dissolved, thereby creating approximately 1 liter of saline water.

III. Results and Discussion:

The outcome of this experiment was the creation of approximately 1 liter of saline solution that approximates the salinity of average seawater at sea level. The procedure proved to be straightforward, emphasizing its ease of implementation in a laboratory setting for various purposes.

Laboratory Preparation of A 0.1 M Hydrochloric Acid Solution Simulating A Ph Of 1

Abstract:

This report describes a method to prepare a 1-liter solution with a pH of 1, equivalent to a 0.1 M Hydrochloric acid (HCl) solution, using a 32% w/w HCl stock solution and distilled water. The results were measured using a pH meter, and the dilution was performed considering the molarity equation M1V1 = M2V2.

I. Introduction:

The pH scale is logarithmic, meaning small numerical changes can correspond to large changes in acidity or basicity. A solution with a pH of 1 has a hydrogen ion (H+) concentration of 0.1 M. Preparing such a solution necessitates careful dilution of a strong acid, in this case, Hydrochloric acid (HCl). The experiment was carried out using distilled water, 32% w/w HCl solution, a pH meter, and standard laboratory glassware.

II. Materials and Methods:

Materials:

1. Distilled water
2. Hydrochloric acid (HCl, 32% w/w, approximately 12 M)
3. pH meter or pH indicator strips
4. Protective equipment: gloves, safety glasses, lab coat
5. Beaker (2 L capacity)
6. Graduated cylinder (100 mL capacity)
7. Volumetric flask (1 L capacity)
8. Dropper or burette

Method:

The method involved carefully adding approximately 8.33 mL of concentrated HCl to approximately 900 mL of distilled water in a beaker while under a fume hood. The solution was then stirred, and its pH was measured. If the pH was

greater than 1, small amounts of HCl were added drop by drop until the desired pH was reached. The solution was then transferred to a 1 L volumetric flask and diluted to the mark with distilled water.

III. Results and Discussion:

The preparation of a solution with a pH of 1 was successfully carried out using the described method.

Bibliography

1. Center, N.R. *Wave Propagation.* [cited 2021 November 21st]; Available from: http://www.ndt-ed.org/EducationResources/CommunityCollege/Ultrasonics/Physics/wavepropagation.html.
2. Gantner, A., et al., *Numerical simulation of piezoelectrically agitated surface acoustic waves on microfluidic biochips.* Computing and Visualization in Science, 2007. **10**(3): p. 145-161.
3. Briggs, G.A.D. and O.V. Kolosov, *6.2 Tensor Derivation of Acoustic Waves in Solids*, in *Acoustic Microscopy (2nd Edition)*. Oxford University Press.
4. Ballantine, D.S., Jr., et al., *2.1.3 Reduced Notation (Engineering Notation)*, in *Acoustic Wave Sensors - Theory, Design, and Physico-Chemical Applications*. Elsevier.
5. Auld, B.A., *Acoustic fields and waves in solids*. 1973: Рипол Классик.
6. Scruby, C.B., K.R. Jones, and L. Antoniazzi, *Diffraction of elastic waves by defects in plates: Calculated arrival strengths for point force and thermoelastic sources of ultrasound.* Journal of Nondestructive Evaluation, 1986. **5**(3): p. 145-156.
7. Prakash, R., *Non-Destructive Testing Techniques*. 2009, Kent, UNITED KINGDOM: New Academic Science.
8. Royer, D. and E. Dieulesaint, *Elastic waves in solids*. 2000, New York;Berlin;: Springer.
9. Ahmad, A. and L.J. Bond, *13.4 General Characteristics of Ultrasonic Waves*, in *ASM Handbook, Volume 17 - Nondestructive Evaluation of Materials (2018 Revision)*. ASM International.
10. Ji, C., et al. *Corrosion evaluation of additive manufacture metal alloy by nondestructive line-focused transducer*. in *2017 IEEE International Ultrasonics Symposium (IUS)*. 2017. IEEE.
11. Li, Q., *Elastic Stiffness Characterization of Anisotropic Materials by Line-focus Ultrasound Transducer*. 2019, University of Pittsburgh.
12. Vijaya, M.S., *Piezoelectric Materials and Devices : Applications in Engineering and Medical Sciences*. 2012, Baton Rouge, UNITED STATES: Taylor & Francis Group.
13. Fraden, J., *Handbook of modern sensors: physics, designs, and applications*. 2004: Springer Science & Business Media.
14. Nakamura, K., *Ultrasonic Transducers : Materials and Design for Sensors, Actuators and Medical Applications*. 2012, Cambridge, UNITED KINGDOM: Elsevier Science & Technology.
15. Quate, C.F., A. Atalar, and H.K. Wickramasinghe, *Acoustic microscopy with mechanical scanning—A review.* Proceedings of the IEEE, 1979. **67**(8): p. 1092-1114.
16. Lemons, R.A. and C.F. Quate, *Acoustic microscope—scanning version.* Applied Physics Letters, 1974. **24**(4): p. 163-165.
17. Weglein, R.D. and R.G. Wilson, *Characteristic material signatures by acoustic microscopy.* Electronics Letters, 1978. **14**(12): p. 352-354.
18. Atalar, A., C.F. Quate, and H.K. Wickramasinghe, *Phase imaging in reflection with the acoustic microscope.* Applied Physics Letters, 1977. **31**(12): p. 791-793.

19. Briggs, A., G. Briggs, and O. Kolosov, *Acoustic microscopy*. Vol. 67. 2010: Oxford University Press.
20. Parmon, W. and H.L. Bertoni, *Ray interpretation of the material signature in the acoustic microscope.* Electronics Letters, 1979. **15**(21): p. 684-686.
21. Kushibiki, J. and N. Chubachi, *Material Characterization by Line-Focus-Beam Acoustic Microscope.* IEEE Transactions on Sonics and Ultrasonics, 1985. **32**(2): p. 189-212.
22. Kushibiki, J., et al., *Characterization of LiNbO3 crystals by line-focus-beam acoustic microscopy.* Applied Physics Letters, 1991. **58**(23): p. 2622-2624.
23. Kobayashi, T., J. Kushibiki, and N. Chubachi. *Improvement of measurement accuracy of line-focus beam acoustic microscope system*. in *IEEE 1992 Ultrasonics Symposium Proceedings*. 1992.
24. Kushibiki, J., Y. Ohashi, and M. Mochizuki, *Evaluation of mass-produced commercial LiTaO/sub 3/ single crystals using the LFB ultrasonic material characterization system.* IEEE Transactions on Ultrasonics, Ferroelectrics, and Frequency Control, 2004. **51**(6): p. 748-755.
25. Tsukahara, Y., K. Ohira, and N. Nakaso. *An ultrasonic micro-spectrometer for the evaluation of elastic properties with microscopic resolution*. in *IEEE Symposium on Ultrasonics*. 1990. IEEE.
26. Khuri-Yakub, B. and C.-H. Chou. *Acoustic microscope lenses with shear wave transducers*. in *IEEE 1986 Ultrasonics Symposium*. 1986. IEEE.
27. Kanai, H., N. Chubachi, and T. Sannomiya, *Microdefocusing method for measuring acoustic properties using acoustic microscope*. IEEE transactions on ultrasonics, ferroelectrics, and frequency control, 1992. **39**(5): p. 643-652.
28. Atalar, A., et al. *Anisotropy sensitivity of an acoustic lens with slit aperture*. in *1993 Proceedings IEEE Ultrasonics Symposium*. 1993. IEEE.
29. Bozkurt, A., et al. *Characterization and imaging with Lamb wave lens at gigahertz frequencies*. in *1994 Proceedings of IEEE Ultrasonics Symposium*. 1994.
30. Yamanaka, K., *Surface acoustic wave measurements using an impulsive converging beam.* Journal of applied physics, 1983. **54**(8): p. 4323-4329.
31. Hsu, N.N., D. Xiang, and G.V. Blessing. *Time-resolved ultrasonic body wave measurements of material anisotropy using a lensless line-focus transducer*. in *1998 IEEE Ultrasonics Symposium. Proceedings (Cat. No. 98CH36102)*. 1998.
32. Xiang, D., N. Hsu, and G. Blessing, *The design, construction and application of a large aperture lens-less line-focus PVDF transducer.* Ultrasonics, 1996. **34**(6): p. 641-647.
33. Xiang, D., N. Hsu, and G. Blessing, *Materials characterization by a time-resolved and polarization-sensitive ultrasonic technique,* in *Review of Progress in Quantitative Nondestructive Evaluation*. 1996, Springer. p. 1431-1438.
34. Hsu, N.N., et al. *Time and polarization resolved ultrasonic measurements using a lensless line-focus transducer*. in *1995 IEEE Ultrasonics Symposium. Proceedings. An International Symposium*. 1995.
35. Yung-Chun, L., J.O. Kim, and J.D. Achenbach, *Acoustic microscopy measurement of elastic constants and mass density.* IEEE Transactions on Ultrasonics, Ferroelectrics, and Frequency Control, 1995. **42**(2): p. 253-264.
36. Lee, Y.-C. and C.-C. Chu, *A double-layered line-focusing PVDF transducer and V (z) measurement of surface acoustic wave.* Japanese journal of applied physics, 2005. **44**(3R): p. 1462.

37. Lee, Y.-C. and S.H. Kuo, *Double-layer PVDF transducer and V (z) measurement system for measuring leaky Lamb waves in a piezoelectric plate.* Ultrasonics, 2007. **46**(1): p. 25-33.
38. Freund, L.B., *Dynamic fracture mechanics*. 1998: Cambridge university press.
39. AZoM. *Stainless Steel - Grade 316 (UNS S31600)*. 2001 [cited 2020 12/03]; Available from: https://www.azom.com/properties.aspx?ArticleID=863.
40. Workman, G.L., P.O. Moore, and D. Kishoni, *Nondestructive Testing Handbook: Ultrasonic Testing*. 2007: Amer Society for Nondestructive.
41. ASTM, *Standard Terminology for Additive Manufacturing Technologies.* 2014(F2792 – 12a): p. 3.
42. Industry, P., *The free beginner's guide to 3D printing.* New York, NY, 2014.
43. Tan, E.T., J.M. Ling, and S.K. Dinesh, *The feasibility of producing patient-specific acrylic cranioplasty implants with a low-cost 3D printer.* Journal of neurosurgery, 2016. **124**(5): p. 1531-1537.
44. Spencer, O.O., O.T. Yusuf, and T.C. Tofade, *Additive manufacturing technology development: A trajectory towards Industrial Revolution.* Am. J. Mech. Ind. Eng, 2018. **3**(5): p. 80-90.
45. Mercado Rivera, F.J. and A.J. Rojas Arciniegas, *Additive manufacturing methods: techniques, materials, and closed-loop control applications.* The International Journal of Advanced Manufacturing Technology, 2020. **109**: p. 17-31.
46. Kedziora, S., et al., *Strength Properties of 316L and 17-4 PH Stainless Steel Produced with Additive Manufacturing.* Materials (Basel), 2022. **15**(18).
47. Poprawe, R., et al., *SLM production systems: recent developments in process development, machine concepts and component design.* Advances in production technology, 2015: p. 49-65.
48. Yadroitsev, I. and I. Smurov, *Selective laser melting technology: From the single laser melted track stability to 3D parts of complex shape.* Physics Procedia, 2010. **5**: p. 551-560.
49. Kokkonen, P., et al., *Design guide for additive manufacturing of metal components by SLM process.* 2016.
50. Messimer, S.L., et al., *Full-density fused deposition modeling dimensional error as a function of raster angle and build orientation: Large dataset for eleven materials.* Journal of Manufacturing and Materials Processing, 2019. **3**(1): p. 6.
51. Abe, Y., et al., *Effect of layer directions on internal structures and tensile properties of 17-4PH stainless steel parts fabricated by fused deposition of metals.* Materials, 2021. **14**(2): p. 243.
52. Garlea, E., et al., *Variation of elastic mechanical properties with texture, porosity, and defect characteristics in laser powder bed fusion 316L stainless steel.* Materials Science and Engineering: A, 2019. **763**: p. 138032.
53. Qin, Y., *12.4.1 Amorphous Metals*, in *Micromanufacturing Engineering and Technology (2nd Edition)*. Elsevier.
54. Klement, W., R. Willens, and P. Duwez, *Non-crystalline structure in solidified gold–silicon alloys.* Nature, 1960. **187**(4740): p. 869-870.
55. Chen, H., *Thermodynamic considerations on the formation and stability of metallic glasses.* Acta Metallurgica, 1974. **22**(12): p. 1505-1511.
56. Schroers, J., *Bulk metallic glasses.* Physics today, 2013. **66**(2): p. 32.

57. Nishiyama, N., et al., *The world's biggest glassy alloy ever made.* Intermetallics, 2012. **30**: p. 19-24.
58. Li, S., et al., *A bulk metallic glass based on heavy rare earth gadolinium.* Journal of non-crystalline solids, 2005. **351**(30-32): p. 2568-2571.
59. Basu, J. and S. Ranganathan, *Bulk metallic glasses: A new class of engineering materials.* Sadhana, 2003. **28**: p. 783-798.
60. Greer, A.L. and E. Ma, *Bulk metallic glasses: at the cutting edge of metals research.* MRS bulletin, 2007. **32**(8): p. 611-619.
61. Ashby, M. and A.L. Greer, *Metallic glasses as structural materials.* Scripta Materialia, 2006. **54**(3): p. 321-326.
62. Inoue, A., et al., *Production methods and properties of engineering glassy alloys and composites.* Intermetallics, 2015. **58**: p. 20-30.
63. Herlach, D., et al., *Containerless processing in the study of metallic melts and their solidification.* International Materials Reviews, 1993. **38**(6): p. 273-347.
64. Inoue, A., *Stabilization of metallic supercooled liquid and bulk amorphous alloys.* Acta materialia, 2000. **48**(1): p. 279-306.
65. Zhou, H., S. Qu, and W. Yang, *An atomistic investigation of structural evolution in metallic glass matrix composites.* International Journal of Plasticity, 2013. **44**: p. 147-160.
66. Huang, Y., et al., *Ductile Ti-based metallic glass spheres.* Scripta Materialia, 2012. **67**(7-8): p. 661-664.
67. Trexler, M.M. and N.N. Thadhani, *Mechanical properties of bulk metallic glasses.* Progress in Materials Science, 2010. **55**(8): p. 759-839.
68. Huang, Y., et al., *The onset of plasticity of a Zr-based bulk metallic glass.* International Journal of Plasticity, 2014. **60**: p. 87-100.
69. Rafique, M., *Bulk Metallic Glasses and Their Composites : Additive Manufacturing and Modeling and Simulation*. 2018, New York, UNITED STATES: Momentum Press.
70. Lai, J., et al., *Promising Ta-Ti-Zr-Si metallic glass coating without cytotoxic elements for bio-implant applications.* Applied Surface Science, 2018. **427**: p. 485-495.
71. Hao, G., et al., *Ti–Zr–Be ternary bulk metallic glasses correlated with binary eutectic clusters.* Materials Science and Engineering: A, 2010. **527**(23): p. 6248-6250.
72. Brechtl, J., et al., *Evolution of the microstructural and mechanical properties of BAM-11 bulk metallic glass during ion irradiation and annealing.* Journal of Nuclear Materials, 2019. **523**: p. 299-309.
73. Ashby, M., et al., *Selection strategies for materials and processes.* Materials & Design, 2004. **25**(1): p. 51-67.
74. Tregilgas, J.H., *Amorphous titanium aluminide hinge: an amorphous titanium aluminide hinge developed for the Texas Instruments digital light processor is the winner of the 2004 ASM Engineering Materials Achievement Award.* Advanced materials & processes, 2004. **162**(10): p. 40-42.
75. Fukushige, T., S. Hata, and A. Shimokohbe, *A MEMS conical spring actuator array.* Journal of Microelectromechanical Systems, 2005. **14**(2): p. 243-253.
76. Inoue, A. and A. Takeuchi, *Recent Development and Applications of Bulk Glassy Alloys.* International Journal of Applied Glass Science, 2010. **1**(3): p. 273-295.
77. Choi-Yim, H. and W.L. Johnson, *Bulk metallic glass matrix composites.* Applied Physics Letters, 1997. **71**(26): p. 3808-3810.

78. Lee, M., et al., *A development of Ni-based alloys with enhanced plasticity.* Intermetallics, 2004. **12**(10-11): p. 1133-1137.
79. Kawashima, A., et al., *Characterization of surface of amorphous Ni-Nb-Ta-P alloys passivated in a 12 kmol/m3 HCl solution.* Materials Transactions, 2004. **45**(1): p. 131-136.
80. Launey, M.E., et al., *Solution to the problem of the poor cyclic fatigue resistance of bulk metallic glasses.* Proceedings of the National Academy of Sciences, 2009. **106**(13): p. 4986-4991.
81. Löffler, J.F., *Bulk metallic glasses.* Intermetallics, 2003. **11**(6): p. 529-540.
82. Schroers, J. and N. Paton, *Amorphous metalalloys.* Advanced Materials & Processes, 2006. **164**(8): p. 61-63.
83. Lu, X., et al., *How a liquid becomes a glass both on cooling and on heating.* Physical review letters, 2008. **100**(4): p. 045701.
84. Angell, C.A., *Insights into phases of liquid water from study of its unusual glass-forming properties.* Science, 2008. **319**(5863): p. 582-587.
85. Hoffmann, H.-J., *Mysteries of the glass transition.* Physics Today, 2008. **61**(1): p. 72-72.
86. Hodge, I., *Mysteries of the glass transition.* Physics Today, 2008. **61**(1): p. 15-, 72.
87. Byrne, C.J. and M. Eldrup, *Bulk metallic glasses.* Science, 2008. **321**(5888): p. 502-503.
88. Wang, W.H., *The elastic properties, elastic models and elastic perspectives of metallic glasses.* Progress in Materials Science, 2012. **57**(3): p. 487-656.
89. Baysinger, G., et al., *CRC handbook of chemistry and physics.* National Institute of Standards and Technology, 2015.
90. Alok, N., *The metals databook*. 1997, McGraw-Hill, New York.
91. Chen, T.N., et al., *Improvements of permeation barrier coatings using encapsulated parylene interlayers for flexible electronic applications.* Plasma Processes and Polymers, 2007. **4**(2): p. 180-185.
92. Cieślik, M., et al., *Silane–parylene coating for improving corrosion resistance of stainless steel 316L implant material.* Corrosion Science, 2011. **53**(1): p. 296-301.
93. Golda-Cepa, M., et al., *Microbiological investigations of oxygen plasma treated parylene C surfaces for metal implant coating.* Materials Science and Engineering: C, 2015. **52**: p. 273-281.
94. Mariello, M., et al., *Captive-air-bubble aerophobicity measurements of antibiofouling coatings for underwater MEMS devices.* Nanomaterials and Nanotechnology, 2019. **9**: p. 1847980419862075.